

Controlling piezoelectric properties through grain orientation in tapecast PZT multilayers

by

Edoardo Francesco Mantheakis

Supervisor

Prof. Ian M. Reaney

Submitted in partial fulfilment of the requirements for the degree of

Doctor of Philosophy

Department of Material Science and Engineering

The University of Sheffield

September 2016 - February 2021

i. Abstract

The synthesis of perovskite $x\text{Na}_{0.5}\text{Bi}_{0.5}\text{TiO}_3-(1-x)\text{PbTiO}_3$ (NBT-PT) templates via topochemical conversion of Aurivillius phase $\text{PbBi}_4\text{Ti}_4\text{O}_{15}$ (PBT) precursor is explored. Significant template particle defects, difficulty in reproducing desired grain morphologies, and the complexity of the synthesis procedure necessitates the use of commercially available BaTiO_3 (BT) templates as a suitable alternative. Successful templated grain growth (TGG) of [001]-textured $\text{Pb}(\text{Zr}_x\text{Ti}_{1-x})\text{O}_3$ (PZT) multilayers using 5 vol. % anisometric (001) BT templates + 5 wt. % PbO (PZT_x-5BT), along with TGG of [001]-textured commercial PZT-5A1 composition using 10 vol. % anisometric (001) BT templates is presented. The critical processing parameters necessary to achieve texturisation in PZT multilayers are investigated, along with further compositional tailoring of the PZT_x-5BT system considering both compositional and piezoelectric effects of the added BT templates within the PZT system. Nanoscale PZT powder is mixed with 5 wt. % PbO, to act as a transient liquid phase during sintering and promote textured grain heteroepitaxy. Anisometric (001) BT platelet shaped seed crystals are added into the PZT slurry and aligned during tapecasting. The tape is sectioned, stacked, and pressed into green bodies prior to binder burnout. During sintering, [001]-textured PZT grains nucleate on the (00 l) crystal faces of the oriented template grains and grow at the expense of the finer matrix material via Ostwald ripening, followed by exaggerated grain growth. The resulting multilayer exhibits texture in the [001] direction. PZT multilayers synthesised with 5 vol. % BT templates + 5 wt. % PbO achieve a Lotgering factor, $f_{(001)} \sim 0.94$, indicating near complete [001]-texturisation. Commercially available PZT-5A1 is also successfully textured using 10 vol. % BT templates, with a reported $f_{(001)} \sim 0.86$. Both starting micron-sized matrix grains and the lack of PbO addition, result in no texturisation being attained. BT template grains are thermally unstable within the PZT matrix. Large grain growth is observed in samples sintered for up to 8 hours. Modification of the starting Zr:Ti ratio of the PZT matrix to ~ 56 Zr mol. % is carried out due to a shift in the morphotropic phase boundary (MPB) for the PZT_x-5BT system. This results in an optimum tetragonal composition ($\text{Pb}_{0.947}(\text{Ba}_{0.053}\text{Zr}_{0.531})\text{Ti}_{1.469}\text{O}_3$) adjacent to the MPB, which exhibits piezoelectric properties ($d_{33} \sim 450$ pC/N, with $T_c \sim 340$ °C) to rival commercial PZT-5A1 ($d_{33} \sim 410$ pC/N, with $T_c \sim 370$ °C). In addition, there is evidence that the MPB curves towards the PbZrO_3 (PZ) end member more sharply with respect to temperature than in the undoped PZT system, resulting in the appearance of T_{r-t} transitions in ϵ_r vs. temperature curves below T_c .

ii. Acknowledgements

I would like to acknowledge my supervisor, Prof. Ian M. Reaney, for giving me the opportunity to work on this project. Your supervision and discussions throughout the course of this project have proven to be invaluable. I am also grateful to Thales for acting as my industrial sponsors, in particular Dr. Laura Stoica for providing continued support over the period of this project, and the Engineering and Physical Sciences Research Council (EPSRC) for funding this project.

I would like to thank Prof. Gary L. Messing at Pennsylvania State University (PSU) for allowing me to join his group on secondment. Their lent knowledge and expertise enabled me without doubt to achieve certain progress within this project. I wish to thank individual group members: Beecher Watson, Michael Brova, and Rebecca Walton for their technical support, comprehensive discussions, and general enthusiasm which aided me tremendously.

I want to mention Tom Hooper at the University of Leeds, for assisting me in providing processed materials, and being ever present for discussing results that materialised throughout both our projects.

I am grateful to Dawei, Leo, Ge, and Kerry, in the Functional Materials and Devices (FMD) group at the University of Sheffield, for their help in the laboratory and training me in the processes necessary to attempt this project. I want to thank the members of the jaja club who have made the last 4 years in Sheffield so memorable: Theo, Imad, Marco, Szymon, Ben, Neassa, Matt, Georgie, Michele, and last but not least Panos.

I am extremely lucky to have had the babou by my side throughout the end of this project. Your encouragement, support, and love have helped me immeasurably and made writing this thesis so much easier. The next chapter in our lives awaits! Finally, I would like to thank my parents who have been there to support and encourage me from the get-go. Without them, this would not have been possible.

iii. Contents

i.	Abstract	1
ii.	Acknowledgements	2
iii.	Contents	3
iv.	Abbreviations and acronyms	6
1.	Introduction	9
2.	Literature review	11
2.1	Perovskite structure	11
2.2	PZT phase diagram	12
2.3	PZT phase formation	13
2.4	Compositional control	14
2.5	Piezoelectricity	15
2.6	Electrostrictive effect	18
2.7	Ferroelectricity	18
2.7.1	Domains	19
2.7.2	Polarisation/strain hysteresis	20
2.7.3	Dopants	22
2.8	Separation of intrinsic/extrinsic piezoelectric contributions	24
2.9	Piezoelectric enhancement	26
2.9.1	Polarisation rotation and polarisation extension	28
2.10	Monoclinic phase	31
2.11	Adaptive phase	34
2.12	Templated grain growth	35
2.13	Template synthesis	39
2.14	Textured PZT ceramics	43
3.	Aims and objectives	45
4.	Characterisation methods	46

4.1	Density measurements	46
4.2	X-ray diffraction	46
4.2.1	D2 PHASER	46
4.2.2	D2 PHASER data analysis	47
4.2.3	Lotgering factor.....	47
4.2.4	STOE STADI P (CuPSD)	48
4.2.5	STOE STADI P (CuPSD) data analysis.....	48
4.3	Scanning electron microscopy	48
4.3.1	Ceramic sample preparation.....	49
4.3.2	Powder sample preparation.....	50
4.4	Dielectric measurements	50
4.5	Poling and quasi-static d_{33} measurements.....	50
4.5.1	Polarisation/strain hysteresis measurements	51
5.	Suitable NBT-PT templates to texture PZT via TGG.....	52
5.1	Synthesis methodology for PBT precursor	52
5.2	X-ray diffraction analysis of PBT precursor	53
5.3	Microstructural characterisation of PBT precursor.....	53
5.4	Synthesis methodology for NBT-PT templates	54
5.5	X-ray diffraction analysis of NBT-PT templates	55
5.6	Microstructural characterisation of NBT-PT templates	57
5.7	NBT-PT templates results summary	63
6.	Platelet shaped BT templates	64
6.1	X-ray diffraction analysis of BT templates	64
6.2	Size separation methodology for BT templates	65
6.3	Microstructural characterisation of BT templates.....	66
6.4	BT templates results summary	68
7.	Textured PZT multilayers via TGG.....	69
7.1	Synthesis methodology for [001]-textured PZT multilayers	69
7.2	Synthesis methodology for PZT/PZT-5A1 ceramics.....	71

7.3	X-ray diffraction analysis of [001]-textured PZT multilayers	72
7.4	Microstructural characterisation of [001]-textured PZT multilayers	76
7.4.1	Parameters affecting texture evolution in PZT multilayers	79
7.5	[001]-textured PZT multilayers results summary	81
8.	Compositional modification of starting PZT matrix powder	83
8.1	Synthesis methodology for PZT _x -5BT ceramics	84
8.2	X-ray diffraction analysis of PZT _x -5BT ceramics	85
8.2.1	Secondary phase in synthesised PZT _x -5BT ceramics	88
8.3	Microstructural characterisation of PZT _x -5BT ceramics	89
8.4	Dielectric properties of PZT _x -5BT ceramics	93
8.4.1	Dielectric properties of inhomogeneous PZT _x -5BT ceramics	96
8.5	Quasi-static d_{33} measurements of PZT _x -5BT ceramics	99
8.6	Polarisation/strain hysteresis measurements	101
8.7	PZT _x -5BT ceramics results summary	101
9.	Conclusions	103
10.	Future work	105
11.	References	107
A.	Appendix	124
B.	Appendix	125
C.	Appendix	126

iv. Abbreviations and acronyms

ASTM	American Society for Testing Materials
BiNN5	Bismuth layered structure; $\text{Bi}_{2.5}\text{Na}_{3.5}\text{Nb}_5\text{O}_{18}$
BSE	Backscattered electron
BT	Perovskite phase; BaTiO_3
B6T17	Perovskite layered structure; $\text{Ba}_6\text{Ti}_{17}\text{O}_{40}$
DTA	Differential thermal analysis
EDS	Energy dispersive X-ray spectroscopy
EPSRC	Engineering and Physical Sciences Research Council
FMD	Functional Materials and Devices group
HRTEM	High resolution transmission electron microscopy
ICDD	International Centre for Diffraction Data
KNN	Perovskite phase; $\text{K}_{0.5}\text{Na}_{0.5}\text{NbO}_3$
MPB	Morphotropic phase boundary
MSS	Molten salt synthesis
NBT	Perovskite phase; $\text{Na}_{0.5}\text{Bi}_{0.5}\text{TiO}_3$
NBT-PT	Perovskite phase, binary solid solution; $x\text{Na}_{0.5}\text{Bi}_{0.5}\text{TiO}_3 - (1-x)\text{PbTiO}_3$
NIST	National Institute of Standards & Technology
NN	Perovskite phase; NaNbO_3
PBT	Aurivillius phase, pseudo-perovskite blocks with interlayering $[\text{Bi}_2\text{O}_2]^{2+}$; $\text{PbBi}_4\text{Ti}_4\text{O}_{15}$
PIN-PMN-PT	Ternary solid solution; $y\text{Pb}(\text{In}_{1/2}\text{Nb}_{1/2})\text{O}_3 - x\text{Pb}(\text{Mg}_{1/3}\text{Nb}_{2/3})\text{O}_3 - (1-(y+x))\text{PbTiO}_3$
PMN-PT	Binary solid solution; $x\text{Pb}(\text{Mg}_{1/3}\text{Nb}_{2/3})\text{O}_3 - (1-x)\text{PbTiO}_3$
PMN-PZT	Binary solid solution; $y\text{Pb}(\text{Mg}_{1/3}\text{Nb}_{2/3})\text{O}_3 - (1-y)\text{Pb}(\text{Zr}_x\text{Ti}_{1-x})\text{O}_3$
PNN	Perovskite phase; $\text{Pb}(\text{Ni}_{1/3}\text{Nb}_{2/3})\text{O}_3$
PSU	Pennsylvania State University
PT	Perovskite phase; PbTiO_3
PVA	Polyvinyl alcohol; $[\text{CH}_2\text{CH}(\text{OH})]_n$
PYN-PMN-PT	Ternary solid solution; $y\text{Pb}(\text{Yb}_{1/2}\text{Nb}_{1/2})\text{O}_3 - x\text{Pb}(\text{Mg}_{1/3}\text{Nb}_{2/3})\text{O}_3 - (1-(y+x))\text{PbTiO}_3$
PZ	Perovskite phase; PbZrO_3
PZ+Z	Atmosphere control powder; $\text{PbZrO}_3 + \text{ZrO}_2$
PZN-PT	Binary solid solution; $x\text{Pb}(\text{Zn}_{1/3}\text{Nb}_{2/3})\text{O}_3 - (1-x)\text{PbTiO}_3$
PZT	Perovskite phase; $\text{Pb}(\text{Zr}_x\text{Ti}_{1-x})\text{O}_3$
R-M	Rhombohedral-monoclinic phase transition
RTGG	Reactive templated grain growth
SBIT	Aurivillius phase, pseudo-perovskite blocks with interlayering $[\text{Bi}_2\text{O}_2]^{2+}$; $\text{SrBi}_4\text{Ti}_4\text{O}_{15}$
SE	Secondary electron
SEM	Scanning electron microscopy
ST	Perovskite phase; SrTiO_3
TGG	Templated grain growth

T-M	Tetragonal-monoclinic phase transition
TMC	Topochemical microcrystal conversion
XRD	X-ray diffraction
T	Temperature
T_c	Curie temperature
T_0	Curie-Weiss temperature
C	Curie constant
T_{r-t}	Rhombohedral to tetragonal ferroelectric-ferroelectric transition temperature
Q_m	Quality mechanical factor
d_{ijk}	Piezoelectric tensor, third rank
σ_{jk}	Stress tensor, second rank
x_{ij}	Strain tensor, second rank
ϵ_{ij}^σ	Dielectric permittivity tensor under constant applied stress, second rank
s_{ijkl}^E	Elastic compliance tensor under constant applied electric field, fourth rank
E_k	Applied electric field
D_i	Dielectric displacement
k_{ij}	Electromechanical coupling coefficient
Q_{ijkl}	Electrostriction tensor, fourth rank
P_i	Polarisation
P_r	Remanent polarisation
P_s	Spontaneous polarisation
d_{33}	Longitudinal piezoelectric coefficient
d_{31}	Transversal piezoelectric coefficient
d_{15}	Shear piezoelectric coefficient
d_h	Hydrostatic piezoelectric coefficient
$d_{33}^*(\vartheta)$	Longitudinal piezoelectric coefficient measured at arbitrary angle ϑ from polar axis
d_{init}	Initial piezoelectric contribution from reversible domain wall motion
X_{max}	Amplitude of driving ac stress
Q_{max}	Piezoelectric charge density
α	Raleigh coefficient
$f_{(001)}$	Lotgering factor measured for [001]-texture
ϵ	Dielectric permittivity
ϵ_r	Relative permittivity
ϵ_{rRT}	Relative permittivity at ambient temperature
ϵ_0	Permittivity of free space
$\tan \delta$	Dielectric loss, or loss tangent
$\tan \delta_{RT}$	Dielectric loss, or loss tangent, at ambient temperature
χ_{ij}	Dielectric susceptibility tensor, second rank
χ_{33}	Longitudinal dielectric susceptibility

χ_{11}	Transversal dielectric susceptibility
E_c	Coercive field
t	Goldschmidt tolerance factor
$V_{\text{O}}^{\bullet\bullet}$	Oxygen vacancies, double positively charged
$V_{\text{Pb}}^{\prime\prime}$	Lead vacancies, double negatively charged
c/a	Tetragonal distortion
q	Separated charge
r	Particle separation distance
μ	Dipole moment vector

1. Introduction

The perovskite solid solution PZT has been studied extensively as a piezoelectric material since its discovery in the 1950s¹⁻³. The drive to find new piezoelectric materials based on the perovskite PZT system has led to both compositional and microstructural enhancements in the field of piezoelectrics. First generation binary relaxor-PbTiO₃ (PT) perovskite counterparts, e.g. Pb(Zn_{1/3}Nb_{2/3})O₃-PT (PZN-PT) and Pb(Mg_{1/3}Nb_{2/3})O₃-PT (PMN-PT), whereby the relaxor component includes mixed B-site cations consisting of Zn²⁺, Mg²⁺, and Nb⁵⁺, exhibit enhanced piezoelectric coefficients (d_{33} , d_{31} , etc.) and quality mechanical factors (Q_m) with the major drawbacks being a significant drop in Curie temperature (T_c), appearance of low temperature rhombohedral to tetragonal phase transitions (T_{r-t}) due to strongly curved morphotropic phase boundaries (MPB) which limit their usable temperature range, and lower coercive fields (E_c) hindering their use in high drive applications⁴⁻⁸. Second generation relaxor-PT based perovskite piezoelectric materials, e.g. Pb(In_{1/2}Nb_{1/2})O₃-PMN-PT (PIN-PMN-PT) and PMN-PZT, with ternary systems with mixed B-site cations including In³⁺ and the incorporation of PZT in binary systems, show improved E_c and T_{r-t} values compared with first generation compositions, albeit with T_c values still significantly lower than that of ‘hard’ PZT variants⁹⁻¹³. The drive to utilise first/second generation piezoelectric materials for high power applications, requiring low dielectric loss ($\tan \delta$) to avoid significant heat generation, has led to the discovery of third generation materials by compositional acceptor doping, e.g. Mn-doped PZN-PT, Mn-doped PIN-PMN-PT, and Mn-doped PMN-PZT, to specifically tailor electromechanical properties¹⁴⁻¹⁶.

As well as focusing on the composition of new Pb-based perovskite piezoelectric materials, significant research has been devoted to different synthesis methods, such as single crystal growth and TGG which can dramatically affect piezoelectric properties via microstructural effects, e.g. domain engineering and reduced domain clamping¹⁷. The ability to grow large single crystals of first/second generation piezoelectric materials has seen a shift away from researching PZT, focussing on more complex systems from which single crystals can be grown¹⁸⁻²⁰. There is currently no reported method in the literature to produce large (cm dimensions) PZT single crystals. The reason for the inherent difficulty in producing larger PZT single crystals is due to incongruent melting across the PZ-PT solid solution range. As PZT melts, zirconia precipitates out in any given composition across the phase diagram²¹. The growth of single crystal piezoelectric materials by a variety of process, e.g. high temperature solution (flux), Bridgman, and modified Bridgman methods, are in general much more costly and time consuming when compared to the conventional solid state synthesis of polycrystalline piezoelectrics²². The use of piezoelectric materials in different modes, increasingly required for new design applications, has created demand for more complex material geometries which cannot be easily accommodated by single crystal growth. It is within this niche that textured polycrystalline piezoelectrics show great promise in achieving enhanced piezoelectric properties to rival those of single crystals, whilst extending the

possibility to significantly improve piezoelectric properties for compositions where single crystal growth is currently not possible or economically unfeasible. PZT therefore, is a prime candidate for texturisation. Successful TGG and reactive templated grain growth (RTGG) of second generation piezoelectrics has been reported in literature, however there is still very limited work published on TGG of PZT²³. The scope of this project is to investigate possible texturisation of PZT multilayers via TGG and assess their piezoelectric properties against conventionally fabricated PZT ceramics.

2. Literature review

2.1 Perovskite structure

PZT has a perovskite structure with the general formula ABO_3 , as illustrated in Figure 1²⁴. The ideal cubic perovskite unit cell has the space group $Pm\bar{3}m$ (no. 221)²⁵. The larger A-site cations (Pb^{2+}) with 12-fold coordination are located on the corners (0,0,0), the smaller B-site cations (Zr^{4+} , Ti^{4+}) with 6-fold coordination are located at the body centres ($\frac{1}{2}$, $\frac{1}{2}$, $\frac{1}{2}$), and the oxygen anions are located on the face centres ($\frac{1}{2}$, 0, 0), (0, $\frac{1}{2}$, 0), (0, 0, $\frac{1}{2}$). This gives rise to a network of corner sharing oxygen octahedra with the formula BO_6 ²⁶. Both A- and B-site interstices accommodate cations with varying ionic radii, which has a dramatic effect on electrical and microstructural properties²⁷. The Goldschmidt tolerance factor, t , describes the geometric considerations for the formation of the prototype perovskite structure from any group of cations²⁴:

$$t = (R_A + R_O) / \sqrt{2}(R_B + R_O) \quad (1)$$

where R_A , R_B , and R_O are the ionic radii of the large A-cation, B-cation, and anion, respectively. The ideal cubic perovskite structure is obtained when $t = 1$. If t deviates far from unity, then a different structure will form, e.g. for $FeTiO_3$ where $t < 0.85$, has the ilmenite structure²⁶. In practice, perovskite structures have t values near to unity, with slight distortions manifesting as lower (than cubic) symmetries. Most industrial applications make use of ferroelectric distortions in compounds such as PZT and BT, however the most prevalent type of phase transitions in perovskites are related to octahedral tilting, which are responsible for a wide range of symmetries. Octahedral tilt transitions have been covered extensively by Megaw²⁸ and Glazer^{29,30} and are non-ferroelectric in nature but can couple to ferroelectric instabilities. In brief, the oxygen octahedra distort according to a cogwheel motion by rotating around their central axes in plane. The layer above has the option to rotate in-phase with the original layer, designated as superscript '+' by Glazer^{29,30}, or out of (anti-) phase, represented by superscript '-'. Each orthogonal axis of the unit cell/octahedral can tilt and thus a sequence of tilt systems can be created, e.g. $a^-a^-a^-$ means that all three orthogonal axes are tilted antiphase, with the resulting lattice distortion defining the symmetry as rhombohedral (space group, $R-3c$), in the absence of other instabilities.

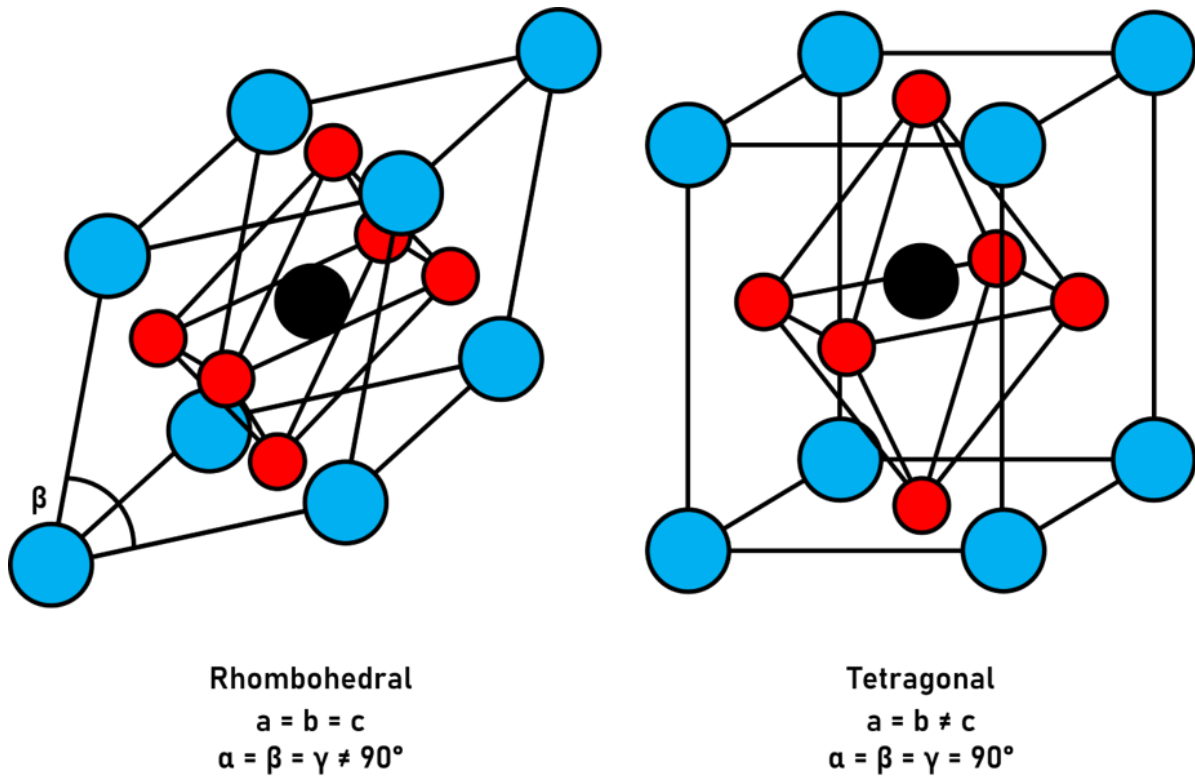


Figure 1 - a) Unit cell illustration of rhombohedral perovskite structure with A-site (blue), B-site (black) cations, and oxygen anions (red); b) tetragonal perovskite structure.

2.2 PZT phase diagram

The PZT system can be considered as a pseudo-binary solid solution of PbZrO_3 (PZ) and PT (Figure 2). The PT end member has a ferroelectric tetragonal (F_T) perovskite structure (space group $P4mm$, no. 99) below a paraelectric-ferroelectric transition temperature, $T_c \sim 490^\circ\text{C}$, Figure 1b. With increasing substitution of Ti^{4+} by Zr^{4+} on the B-site, the tetragonal distortion, c/a , reduces, eventually transforming to a ferroelectric rhombohedral ($F_{R(HT)}$) perovskite structure (space group $R3m$, no. 160) at ~ 48 mol. % PT³, Figure 1a. The phase boundary between the two ferroelectric phases is almost vertical, i.e. temperature independent, and is referred to as an MPB. The T_c of compositions near to the MPB are around $\sim 380^\circ\text{C}$. Increasing PZ concentration results in an octahedral tilt transition into a second ferroelectric rhombohedral ($F_{R(LT)}$) perovskite structure (space group $R3c$, no. 161), where the oxygen octahedra become tilted about the $[111]$ direction with $a^-a^-a^-$ tilt system²⁹. At higher PZ concentrations (~ 6 mol. % PT) an antiferroelectric orthorhombic structure appears¹, with some authors reporting an antiferroelectric tetragonal phase found just below the T_c ($\sim 230^\circ\text{C}$) for PZ-rich compositions, with up to 1 mol. % PT³¹.

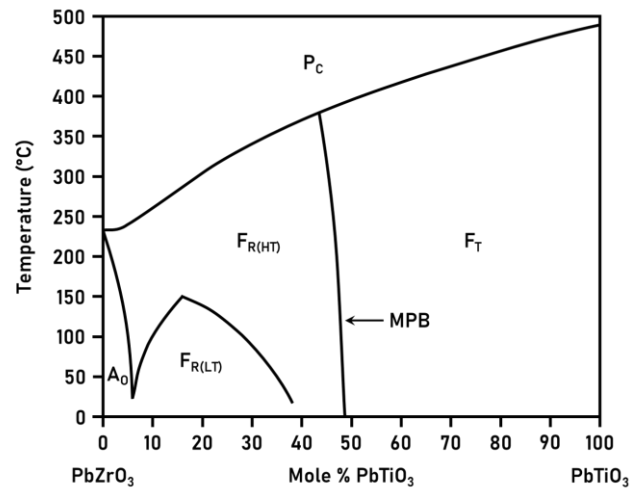


Figure 2 - PZT phase diagram, where P_c = paraelectric cubic, A_0 = antiferroelectric orthorhombic, $F_{R(LT)}$ = low temperature ferroelectric rhombohedral, $F_{R(HT)}$ = high temperature ferroelectric rhombohedral, F_T = ferroelectric tetragonal. Adapted from Jaffe *et al.* ³².

2.3 PZT phase formation

The phase formation of PZT from mixed oxide powders has been discussed and examined extensively in references ³³⁻³⁷. Several intermediate phases have been identified using X-ray diffraction and differential thermal analysis (DTA) techniques prior to PZT formation. All sources report PZT formation below 800 °C. There is a consensus that PT is the initial intermediary phase to form at 600 °C, after which various differing reaction sequences have been proposed. The formation of PZ as an intermediary product has not been reported in literature. Differing reaction sequences are shown in Table 1.

Table 1 - Comparative list of different reaction sequences for PZT formation

ref. Matsuo & Sasaki ³³	ref. Hankey <i>et al.</i> ³⁶	ref. Hiremath <i>et al.</i> ³⁷
$P + T \rightarrow PT$	$P + T \rightarrow PT$	$P + T \rightarrow PT$
$PT + P + Z \rightarrow PT + PZT (Z)$	$PT + P + Z \rightarrow PT + P_{(ss)}$	* $PT + P + Z \rightarrow PZT (Z)$
		or
		* $P_{(ss)} + Z \rightarrow PZT (Z)$
$PT + PZT (Z) \rightarrow PZT$	$PT + P_{(ss)} \rightarrow PZT$	* $PT + P + Z \rightarrow PZT (T)$
		$PZT (Z) + PZT (T) \rightarrow PZT$

where $P = PbO$, $T = TiO_2$, $Z = ZrO_2$, $PT = PbTiO_3$, $P_{(ss)}$ = solid solution of PbO , $PbTiO_3$, ZrO_2 , $PZT (Z)$ = Zr-rich PZT, $PZT (T)$ = Ti-rich PZT. Stages donated with * are reported to be concurrent and competing.

One of the first proposed reaction sequences by Matsuo & Sasaki³³, found the formation of PZT to originate from the final homogenisation of both PT and Zr-rich PZT phases. Chandratreya *et al.*³⁴ hypothesised two junctions for perovskite PZT nucleation after initial PT formation: PT/ZrO₂ and PbO/ZrO₂. It is inferred that the rapid diffusion of Ti⁴⁺ across PbO towards the PbO/ZrO₂ junction quickly eliminates any intermediate PZ, rendering it undetectable. An intermediate tetragonal PbO solid solution phase, P_(ss), including PT and ZrO₂ has also been reported by Speri³⁵ and Hankey *et al.*³⁶, identified by the presence of *d*-spacings in X-ray diffraction data slightly smaller than those expected for tetragonal PbO. Incorporating both identified Zr-rich PZT and P_(ss) phases, Hiremath *et al.*³⁷ proposed a reaction sequence whereby the formation of Ti-rich and Zr-rich PZT intermediaries are competing processes, highly sensitive to powder properties. Variations in starting ZrO₂ particle size directly affect whether the reaction for Ti-rich or Zr-rich PZT intermediate phases are favoured. The reported effects of starting particle size, and more general differences in experimental parameters, can explain the discrepancies between the reported reaction sequences. It is important however, to allow for sufficient time for interdiffusion and homogenisation of the B-site Ti⁴⁺/Zr⁴⁺ cations in the final stage of the PZT reaction sequence. Tight processing controls, specifically on starting oxide particles size, will aid and ensure complete homogenisation whilst minimising phase coexistence.

2.4 Compositional control

One major difficulty in synthesising single-phase PZT ceramics is the volatility of PbO, which has a melting point ~ 888 °C. Sintering temperatures for conventional ceramics exceed > 1000 °C. In the case of PZT, this renders the high vapour pressure of PbO during sintering a major problem in maintaining satisfactory compositional control. Several studies have been conducted, examining the effects of different sintering atmospheres^{38–41} and excess PbO additions^{42–44} on both the resulting final composition and densification kinetics. Small variations in PbO concentration can result in liquid phase sintering (excess PbO), single-phase solid-state sintering (stoichiometric PbO), and two-phase solid-state sintering (PbO deficient). Northrop^{45,46} first reported a distinct Pb-depleted layer, i.e. secondary phase, in sintered PZT pellets, with a solid solution of TiO₂-ZrO₂ present within the depleted layer. The composition of the secondary phase was predicted to move along the line towards the TiO₂-ZrO₂ binary in the PZT ternary diagram with increasing PbO loss. Webster *et al.*⁴⁷ proposed ZrO₂ as the main component of the secondary phase to explain the decrease in piezoelectric properties of starting tetragonal MPB PZT compositions. The rate of PbO loss in PZT under an atmosphere of air is reported to be substantially slower than in vacuum³⁸. Holman & Fulrath³⁹ found non-linear and limiting PbO loss behaviour within the single-phase PZT region compared to constant PbO activity within both excess PbO and deficient two-phase regions.

Two common methods to compensate for PbO loss during sintering include adding excess PbO to the starting green body and/or sintering with sacrificial powder. Härdtl & Rau⁴⁰ first reported firing PZT

pellets in covered crucibles with the addition of PZ pellets to avoid substantial PbO loss. PZ maintains a PbO partial pressure higher than the dissociation pressure of PZT, resulting in loss of PbO from the PZ source. Kingon & Clark⁴¹ reported a final 0.8 % PbO-deficiency in PZT compacts using PZ+Z atmosphere powders, with slight initial PbO loss from the sample occurring prior to equilibration with the atmosphere powders. There is a consensus that sintering in a closed crucible configuration with PZ+Z packing powder is satisfactory to maintain near stoichiometric PZT, i.e. single-phase, and avoid significant degradation in electric properties. Atkins & Fulrath⁴⁸ indicated a dependency of the densification rate in solid-state sintering of PZT on oxygen vacancy ($V_{\text{O}}^{\bullet\bullet}$) concentration, with accelerated densification in sintering atmospheres with reduced O_2 partial pressure. Further studies on densification by Kingon & Clark^{42,43} found liquid phase sintering with starting excess PbO to enhance early stage densification due to particle rearrangement, however final densities were reported to be sensitive to the initial distribution of the liquid phase. The addition of PbO to form a liquid phase is also known to give rise to compositional inhomogeneity due to the different solubilities of TiO_2 and ZrO_2 in PbO⁴⁴. Higher densities (~ 99 % theoretical density) are reported for sintered, slightly PbO deficient single-phase samples^{42,48}. Therefore, the desire to add excess PbO to starting PZT powder to compensate for PbO loss during sintering should be avoided by using suitable crucible configurations with PZ+Z packing powder. This should achieve sufficiently dense single-phase PZT compacts with minimal loss of PbO and Zr:Ti non-stoichiometry, negating and detrimental effects of PbO loss on piezoelectric properties.

2.5 Piezoelectricity

Piezoelectricity is the accumulation of electric charge in certain solid materials in response to an applied stress⁴⁹. Materials with centrosymmetric crystal structures, i.e. crystals structures that have a centre of symmetry, have no polar properties (not piezoelectric) due to inversion symmetry cancelling out any dipole moments within the lattice⁵⁰. The piezoelectric effect is only seen in crystalline materials with no inversion symmetry, i.e. noncentrosymmetric. 21 out of 32 crystal classes are noncentrosymmetric, with 20 exhibiting piezoelectricity⁵¹. Both tetragonal and rhombohedral PZT structures have point groups, $4mm$ and $3m$, that exhibit piezoelectricity. The direct piezoelectric effect is the internal generation of electrical charge within a piezoelectric crystal under an applied external stress. The direct piezoelectric effect is expressed as^{51,52}:

$$D_i = d_{ijk}\sigma_{jk} \quad (2)$$

where D_i is the generated dielectric displacement (or polarisation), d_{ijk} is a third rank tensor of piezoelectric coefficients, and σ_{jk} is the stress tensor. The converse piezoelectric effect is the change in expansion of the piezoelectric crystal under an applied external electric field. The converse piezoelectric effect is expressed as:

$$x_{ij} = d_{kij}E_k \quad (3)$$

where x_{ij} is the resulting strain tensor, and E_k is the applied electric field. In practice, linear piezoelectricity is the coupling between elastic variables (stress, σ , and strain, x) and dielectric variables (dielectric permittivity, ϵ , and electric field, E). (2 & 3 can therefore be both written as piezoelectric constitutive equations, with the strain-charge form:

$$D_i = d_{ijk}\sigma_{jk} + \epsilon_{ij}^\sigma E_j \quad (4)$$

$$x_{ij} = s_{ijkl}^E \sigma_{kl} + d_{kij}E_k \quad (5)$$

where the second term in equation (4) denotes the linear polarisation of a material under an applied field, with ϵ_{ij}^σ the dielectric permittivity tensor under constant applied stress, and the first term in equation (5) denotes Hooke's law, with s_{ijkl}^E a fourth rank tensor of elastic compliances under constant applied electric field. The units of the direct piezoelectric coefficients are ($C N^{-1}$) and for the converse piezoelectric coefficients ($m V^{-1}$). The piezoelectric coefficients for the direct and converse effects are thermodynamically identical, i.e. $d_{direct} = d_{converse}$ ⁵². The piezoelectric coefficient, d_{ijk} , from equation $D_i = d_{ijk}\sigma_{jk}$ (2, can be written in Voigt notation, d_{ij} , with the polarisation indices i having 3 possible values (1, 2, 3) relating to the measured polarisation along one of the three principle axes, and the stress component, σ_{jk} , a symmetrical tensor with only 6 distinct elements having values ($\sigma_{xx}, \sigma_{yy}, \sigma_{zz}, \sigma_{yz}, \sigma_{xz}, \sigma_{xy} \equiv 1, 2, 3, 4, 5, 6$) dependent on the direction of the applied stress (Figure 3). Piezoelectric coefficients measured in the direction of the applied electric field, e.g. d_{11}, d_{22}, d_{33} , are termed longitudinal, those measured perpendicular to the applied electric field, e.g. d_{31}, d_{23} , are termed transversal, with the remaining, e.g. d_{15}, d_{26} , known as piezoelectric shear coefficients.

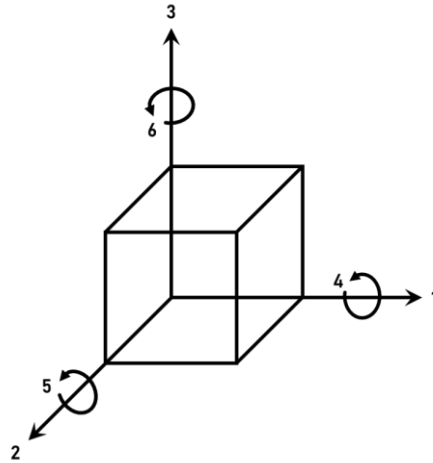


Figure 3 - Notation of axes for poled ceramic where 1, 2, 3 are principal axes with 4, 5, 6 denoting shear planes.

The piezoelectric coefficient relating to hydrostatic pressure, d_h , is given by the relation:

$$d_h = d_{33} + 2d_{31} \quad (6)$$

In general, high d_{ij} coefficients are an important indicator of material suitability for strain-dependent, e.g. actuator, applications. The ability of the piezoelectric material to convert electrical energy to mechanical, and vice versa, is described by the electromechanical coupling factor k_{ij} , expressed as:

$$k^2 = \frac{\text{converted electrical energy}}{\text{input mechanical energy}} \quad (7)$$

for the direct effect, and:

$$k^2 = \frac{\text{converted mechanical energy}}{\text{input electrical energy}} \quad (8)$$

for the converse effect. The conversion of electrical energy to mechanical, and vice versa, is almost never equal, i.e. k_{ij} is less than unity. k values are used as a figure of merit for characterising piezoelectric materials, with materials with high k values considered desirable³².

2.6 Electrostrictive effect

The electrostrictive effect is a non-linear coupling of elastic and electric variables occurring in all dielectric materials ⁵³. The electrostrictive strain of a material, x_{ij} , under an applied field, E_i , is proportional to the square of the induced polarisation, P_i , expressed by the following equation:

$$x_{ij} = Q_{ijkl} P_k P_l \quad (9)$$

where Q_{ijkl} are electrostrictive coefficients of the fourth rank tensor. Electrostriction results from the displacement of ions within the crystal lattice under an applied electric field. Electrostriction occurs in all crystal classes, regardless of their symmetry ⁵⁴. The distinction between piezoelectricity and electrostriction is that the former is limited to 20 noncentrosymmetric crystal classes and exhibits linear rather than quadratic proportionality to the induced polarisation.

2.7 Ferroelectricity

A subset of piezoelectric materials exhibit ferroelectricity. Ferroelectric materials have a spontaneous dipole moment (polarisation) that can be reversed (switched) by an applied external electric field ⁵⁵. The dipole moment, μ , is given by the vector:

$$\mu = q \cdot r \quad (10)$$

where q is the separated charge, and r is the distance between the two particles. The spontaneous polarisation, P , is defined as the total dipole moment per unit volume, expressed as:

$$P = \frac{\sum \mu}{V} \quad (11)$$

where $\sum \mu$ is the vector sum of dipole moments in each unit cell, and V is the volume. The requirement of ferroelectric materials to exhibit a spontaneous dipole moment dictates that the crystal structure cannot be centrosymmetric. It therefore follows that all ferroelectric materials also exhibit piezoelectricity, however not all piezoelectric materials are ferroelectric. In ferroelectric materials, the spontaneous polarisation is constrained along certain crystallographic axes (orientations) dependent on

the apparent ferroelectric crystal structure. On cooling a ferroelectric material from its high temperature paraelectric phase (non-ferroelectric), the material transforms into a lower symmetry ferroelectric phase. The change of crystal structure from high to low symmetry, e.g. cubic to tetragonal, is accompanied by a spontaneous strain due to the differences in dimensions between the paraelectric and ferroelectric unit cells, e.g. $a \neq c$ in tetragonal crystal systems. The temperature at which this phase transformation occurs is denoted by the T_c . Above T_c , the dielectric permittivity decreases with temperature according to the Curie-Weiss law, expressed as:

$$\varepsilon = \varepsilon_0 + \frac{C}{T-T_0} \quad (12)$$

where ε is the dielectric permittivity, ε_0 is the permittivity of free space, C is the Curie constant, T is the temperature, and T_0 is the Curie-Weiss temperature ($T_0 < T_c$).

2.7.1 Domains

The onset of spontaneous polarisation below the T_c results in the formation of surface charge which produces an electric field within the material, called the depolarising field, oriented opposite to the spontaneous polarisation⁵⁶. The associated electrostatic energy is minimised by the creation of ferroelectric domains, regions where all the dipole moments in adjacent unit cells have the same orientation, with oppositely oriented polarisation within individual grains (Figure 4). The formation of certain domains can also arise to minimise elastic energy from mechanical constraints, e.g. transformational stresses (spontaneous strain)⁵⁷. Individual domains are separated by domain walls. Domain walls which separate regions with antiparallel oriented polarisation (inversion domains) are termed 180° domain walls, whereas those that separate regions of polarisation with non-180° angles (twin domains) are termed non-180° domain walls (90° domain walls in tetragonal ferroelectrics, 71° and 109° domain walls in rhombohedral ferroelectrics). Both 180° and non-180° domain walls are ferroelectric, i.e. affect the dielectric response, and reduce the electrostatic energy associated with the depolarising field, however only non-180° domain walls are ferroelastic, i.e. affect the piezoelectric response, minimising the elastic energy and contributing to the direct piezoelectric effect⁵⁸.

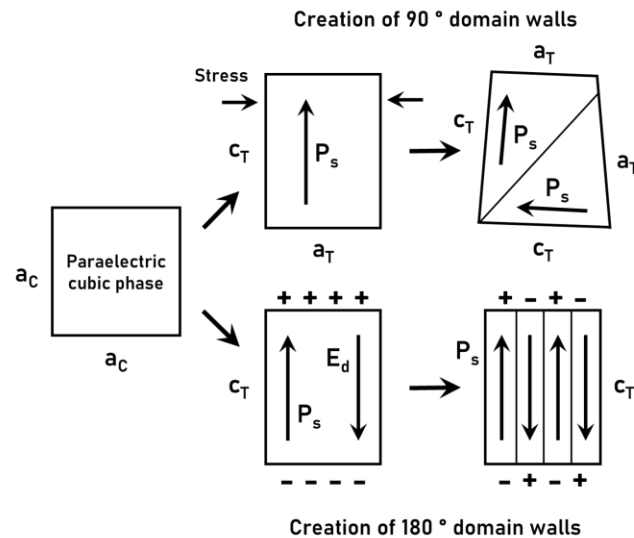


Figure 4 - Formation of 90° (non- 180°) and 180° domain walls in tetragonal perovskite ferroelectric material. Reproduced from Damjanovic⁵⁸.

The type of non- 180° domain walls that can occur are dependent on the symmetry of the ferroelectric phase, e.g. rhombohedral PZT develops spontaneous polarisation along the eight body diagonal directions of the paraelectric cubic unit cell forming 71° , 109° , and 180° domain walls. The random orientation of grains in polycrystalline ceramics, and therefore random orientation of spontaneous polarisation, results in the ferroelectric material having a net zero polarisation, i.e. exhibiting no piezoelectric effect, on cooling from the paraelectric phase. Ambient ferroelectric ceramics may be 'poled' by applying a strong electric field which reorients the domains within individual grains in the direction of the applied electric field. In the case of ferroelectric single crystals, poling can eventually induce a single (mono-) domain state.

2.7.2 Polarisation/strain hysteresis

Ferroelectric hysteresis arises from domain wall switching on reversal of the applied electric field (Figure 5). Under small electric fields, the polarisation increases linearly, as the electric field is not strong enough to switch domains not aligned in the direction of the applied electric field (points A-B). On increasing the electric field strength, the measured polarisation increases non-linearly as the polarisation of domains start to switch in the direction of the applied electric field (points B-C), until all the domains are aligned, and the response becomes linear again (points C-D). Greater electric field strength can eventually exceed the materials dielectric strength causing electrical breakdown. On decreasing the electric field strength, some domains will switch back away from the direction of the applied electric field, however a non-zero remanent polarisation, P_r , at zero field persists. Reversal of the electric field is necessary to attain a net zero polarisation state (point E), with the electric field strength required to completely switch the material termed the coercive field, E_c . Further increasing the

strength of the electric field in the negative direction causes a new alignment of dipoles along with domain switching (point F). The saturation polarisation, P_s , is taken as the linear intercept of the polarisation axis extrapolated from the linear response (points C-D) at high electric field strength.

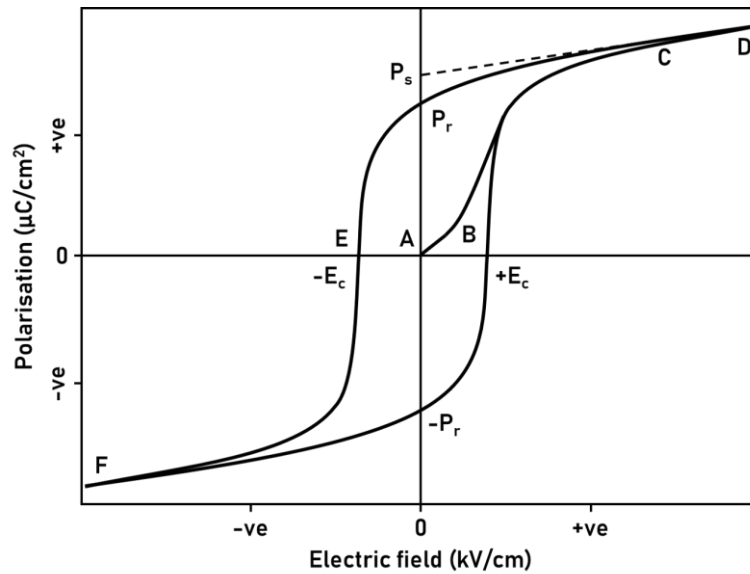


Figure 5 - Ferroelectric polarisation-electric field (P-E) hysteresis.

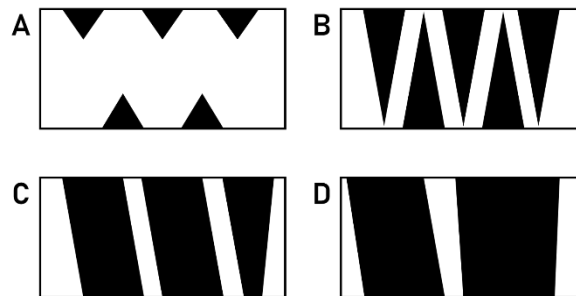


Figure 6 - a) Nucleation of oppositely oriented domains (black); b) forward growth of domains through sample thickness; c) sideways expansion of domains; d) coalescence of residual domains. Reproduced from Shur⁵⁹.

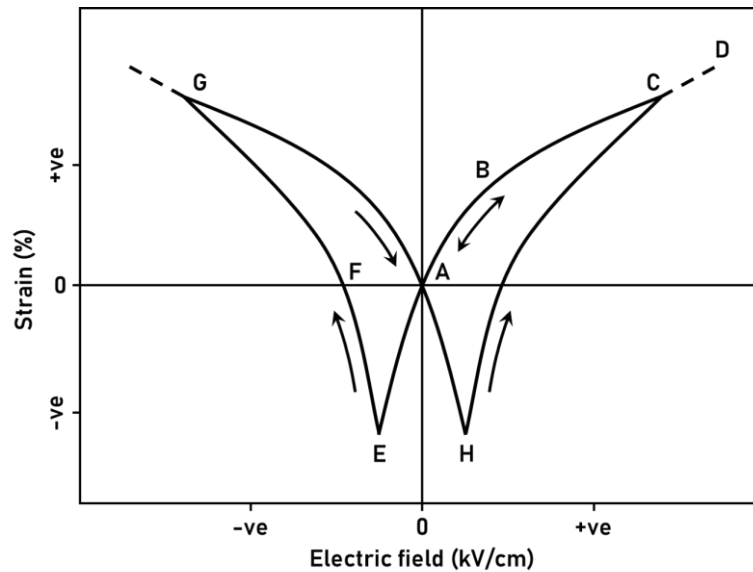


Figure 7 - Ferroelectric strain-electric field (S-E) hysteresis.

The process of domain switching occurs with the nucleation and growth of antiparallel domains via domain wall motion (Figure 6)⁵⁹. Ferroelectric materials also exhibit strain-electric field hysteresis due to the converse piezoelectric effect and switching/movement of domain walls (Figure 7). On increasing the electric field strength in the positive direction, the crystal expands non-linearly, resulting in a crystal strain (points A-B). The non-linear effect is due to the partial switching and movement of non-180° domain walls which cause changes in crystal dimensions⁶⁰⁻⁶². Greater electric field strength results in increasing material strain (point C), achieving a maximum strain, S_{max} , until a saturated linear portion, not usually seen experimentally, is achieved by the formation of a singular domain state at very high electric field strength (points C-D). On decreasing the electric field aligned with the spontaneous polarisation, the strain reduces to zero (points C-A). At this point the electric field is reversed, antiparallel to the poling direction, resulting in a contraction of the crystal, i.e. negative strain (points A-E). Further increasing the electric field strength in the negative direction causes the polarisation to switch parallel to the field (switching and movement of non-180° domain walls), resulting in a positive strain (points E-F). Increasing electric field strength again results in another strain maxima (point G), falling back down to zero on removal of the electric field (points G-A).

2.7.3 Dopants

Factors that influence the nucleation and movement of domain walls directly affect both polarisation and strain hysteresis. The movement of non-180° domain walls can occur at electric fields well below the switching field strength and form part of the extrinsic contributions to piezoelectricity along with defect movement, with the other main contribution being an intrinsic lattice response^{62,63}. Elastic and electrical defects can interfere with both the polarisation within domains and domain wall motion. Charged vacancies and trapped electrons within domain walls can pin/clamp domain walls rendering

them immobile, whilst coupled oxygen vacancies ($V_{\text{O}}^{\cdot\cdot}$)-acceptor dipole pairs can make domain switching more difficult. Whilst these defects are inevitably introduced during ceramic synthesis, they can be promoted by the addition of chemical dopants. PZT is rarely fabricated without dopant additions, with commercial PZT compositions falling into two categories, ‘hard’ and ‘soft’, depending on the valence of the dopant addition.

‘Hard’ compositions involve acceptor doping by replacing A-site Pb^{2+} with monovalent cations (K^+ , Na^+ , Rb^+ , etc.) and B-site $\text{Ti}^{4+}/\text{Zr}^{4+}$ with lower valence cations (Fe^{3+} , Mn^{3+} , Sc^{3+} , Co^{3+} , etc.)⁶⁴. Acceptor doping results in compensating $V_{\text{O}}^{\cdot\cdot}$ to maintain electroneutrality, which when coupled with negatively charged defects, form electric dipoles and elastic defects (elastic dipoles) due to the difference in substituted atomic sizes. These defects affect the extrinsic piezoelectric properties via proposed volume and domain effects⁶⁵. The volume effect arises from the easy motion of $V_{\text{O}}^{\cdot\cdot}$ through the octahedral network, which results in mobile (weak) $V_{\text{O}}^{\cdot\cdot}$ -acceptor dipole pairs that favour specific spontaneous polarisation directions⁶⁶. The resulting internal bias stabilises the domain structure, making any further movement of domain walls unfavourable^{67,68}. The domain effect arises from the diffusion of defects, driven by the neutralisation of internal stress (elastic) or charge compensation (electric), towards domain walls, subsequently fixing their position. The stable domain wall structure that results from acceptor doping increases the coercive field and the poling/depoling field strength of ceramic samples. ‘Hard’ compositions exhibit lower $\tan \delta$ values due to a reduction in the contribution from domain wall motion, and lower piezoelectric response due to a suppression of the extrinsic contribution.

‘Soft’ compositions involve donor doping by replacing both A-site Pb^{2+} with trivalent cations (La^{3+} , Bi^{3+} , Nd^{3+} , etc.) and B-site $\text{Ti}^{4+}/\text{Zr}^{4+}$ with higher valence cations (Nb^{5+} , Ta^{5+} , Sb^{5+} , etc.)⁶⁴. Donor doping results in compensating lead vacancies ($V_{\text{Pb}}^{\cdot\cdot}$) to maintain electroneutrality³². The $V_{\text{Pb}}^{\cdot\cdot}$ -donor dipole pairs are not as mobile as the $V_{\text{O}}^{\cdot\cdot}$ -acceptor dipole pairs introduced in ‘hard’ compositions due to the large difference in distance between cation-cation and oxygen-oxygen occupation sites in the unit cell (~ 0.4 nm between A- or B-site cations, 0.28 nm between oxygen octahedral sites). The effectively immobile $V_{\text{Pb}}^{\cdot\cdot}$ -donor dipole pairs do not produce a ‘hardening’ effect. This results in ‘soft’ compositions having lower coercive field and poling/depoling field strength, along with increased $\tan \delta$ values from facile domain wall motion and higher piezoelectric coefficients.

Another effect of dopant substitution on material properties is a reduction in the T_c when doping with a less polarisable species. Substitution of less polarisable cations on the A- and B-sites, e.g. Ba^{2+} for Pb^{2+} , causes a decrease in T_c accompanied by an increase in room temperature ϵ_r , resulting in a lowering of the strain energy associated with non-180° domain walls. This reduction in strain energy lowers the required activation energy for domain wall motion as the phase transition is depressed towards ambient temperatures, i.e. flattening of free energy profile, enabling easier domain wall motion and resulting in greater piezoelectric response⁶⁹.

2.8 Separation of intrinsic/extrinsic piezoelectric contributions

Separating the intrinsic/extrinsic contributions of the piezoelectric response in polycrystalline ceramics can be challenging due to the complex interactions between domain wall configurations and present defects, of which detailed knowledge is often not known. The intrinsic contribution relates to the lattice, consisting of an average response of individual ferroelectric domains within the ceramic, which can be determined in principle using thermodynamic phenomenological theory not discussed here⁷⁰⁻⁷². The extrinsic contribution arises from the existence of domain walls, phase boundaries, and defect dipoles^{62,63,73}.

One assumption utilised to separate out intrinsic/extrinsic contributions is the apparent ‘freezing out’ of domain walls and defect movement at very low temperatures (approaching 0 K). The ferroelectric properties exhibited at such low temperatures are due to only the intrinsic lattice response, as domain wall fluctuation and nucleation is a thermally activated process^{73,74}. The freezing out of the extrinsic contribution has been reported experimentally, with ‘hard’ and ‘soft’ PZT compositions shown to have converging dielectric permittivity and piezoelectric coefficients with decreasing temperature⁷⁴. Once the intrinsic contribution is determined at near 0 K, the extrinsic response can be derived at any temperature.

Another method to separate the intrinsic/extrinsic contributions is the analysis of the piezoelectric response at weak to moderate electric fields with regard to the Rayleigh Law, derived to describe the analogous movement of magnetic domains in ferromagnetic materials at low magnetic fields (weak field permeability and magnetisation)⁷⁵⁻⁷⁷. The presence of defects randomly distributed throughout the material, which act to pin/clamp domain walls, give rise to local potential energy wells with respect to individual domain wall positions. At low electric fields, reversible domain wall motion occurs when domain walls become excited (move around) within their respective potential well (Figure 8).

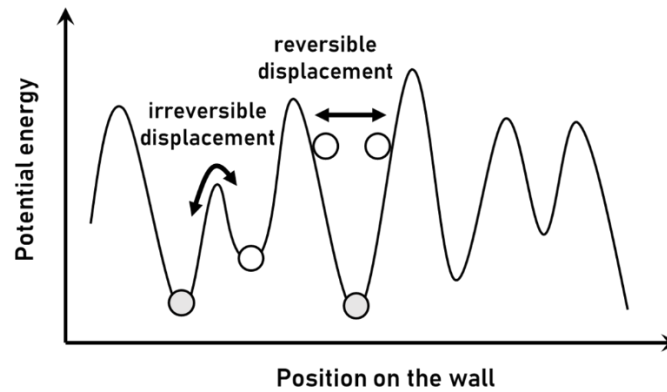


Figure 8 - Domain wall potential in medium with randomly distributed pinning centres. Reproduced from Damjanovic ⁵⁸.

With increasing electric field strength, the domains can overcome the surrounding energy barrier and move into new positions associated with another potential energy minima, resulting in irreversible domain wall displacements ^{62,77}. The linear relationship of the direct piezoelectric coefficient, d_{33} , at low electric fields seen in the d_{33} vs. amplitude of ac stress plot can be expressed as:

$$d_{33} = d_{init} + \alpha X_{max} \quad (13)$$

where d_{init} is the initial piezoelectric contribution from reversible domain wall motion (electric field independent term), α is the Rayleigh coefficient, X_{max} is the amplitude of the driving ac stress. The linear intercept of the d_{33} axis, i.e. when $X_{max} = 0$, indicates the intrinsic piezoelectric contribution of averaged individual ferroelectric domains within the material. The piezoelectric charge density (Q_{max}) may be expressed as:

$$Q_{max} = d_{init} X_{max} + \alpha X_{max}^2 \quad (14)$$

The Rayleigh parameter, α , indicates the change in d_{33} per unit of ac stress due to irreversible domain wall motion (part of the extrinsic response). Ferroelectric materials that do not exhibit irreversible non-180 ° domain wall motion have a Rayleigh parameter, $\alpha = 0$, with the piezoelectric coefficient independent of the ac field amplitude ⁷⁸. It is important to note that the d_{init} parameter is strongly dependent on previous poling conditions. The dependence of the piezoelectric charge density, Q , with respect to stress, X , is given by:

$$Q(X) = (d_{\text{init}} + \alpha X_{\text{max}})X \pm \frac{\alpha}{2}(X_{\text{max}}^2 + X^2) \quad (15)$$

The ratio of the extrinsic contribution of irreversible domain wall motion to the total piezoelectric response at low electric fields can be determined from the expression:

$$\frac{d_{\text{ext}}}{d_{\text{tot}}} = \frac{\alpha X_{\text{max}}}{(d_{\text{init}} + \alpha X_{\text{max}})} \quad (16)$$

The Rayleigh law is suitable to estimate domain wall contributions to the stress and frequency dependency of the piezoelectric response at low electric fields⁷⁹. As the electric field amplitude approaches the coercive field, the energy landscape changes, and the Rayleigh law is no longer applicable. Departure from the linear stress dependence of the d_{33} at low fields may also become significant in samples with small grain sizes (small domain widths) due to domains walls interacting with each other.

2.9 Piezoelectric enhancement

Previous understanding of enhanced piezoelectric response in near MPB compositions found a coexistence of two degenerate ferroelectric phases to have a combined number of spontaneous polarisation directions, e.g. 14 spontaneous polarisation directions in PZT, 6 tetragonal $\langle 001 \rangle$ directions and 8 rhombohedral $\langle 111 \rangle$ directions. This increase in the number of possible spontaneous polarisation directions allows for easy polarisation switching, i.e. greater alignment of domains to the applied electric field, and facilitated domain wall motion, both resulting in a larger volume fraction of the material contributing to the overall piezoelectric response. This assumption involves both intrinsic and extrinsic effects contributing to piezoelectric enhancement around the MPB, whilst indicating that the largest piezoelectric response is to be expected along the spontaneous polarisation directions of the ferroelectric crystal in question. The observation of a maximum electromechanical response in PZT compositions just on the tetragonal side of the MPB, disproved this theory⁸⁰.

Anomalously large piezoelectric coefficients and electromechanical coupling constants ($d_{33} \sim 1500$ pC/N and $k_{33} \sim 0.92$) in rhombohedral PZN-9PT single crystals cut along non polar directions, e.g [001] direction for rhombohedral crystals, were first reported by Kuwata *et al*^{4,5}. Further work by Park & Shrout⁸¹⁻⁸³ found similarly large properties ($d_{33} \sim 2500$ pC/N and $k_{33} \sim 0.94$) in [001]-oriented rhombohedral PZN-8PT single crystals, a direct consequence of piezoelectric anisotropy, with an ultrahigh strain up to 1.7 %, and remarkable anhysteretic behaviour. This anhysteretic behaviour was explained by the formation of engineered domain states (Figure 9).

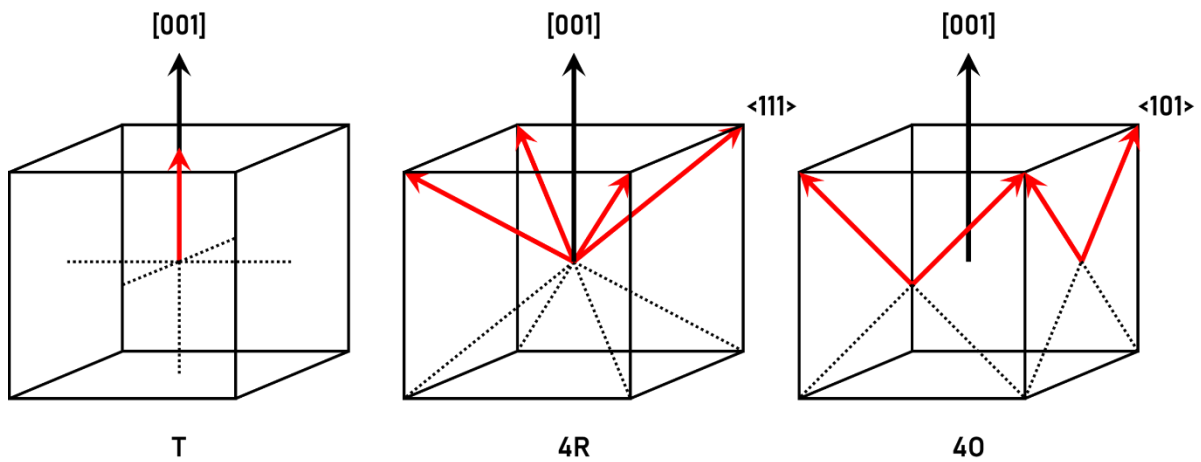


Figure 9 - Pseudocubic representations of equivalent polarisation vectors (red arrows) in single crystals poled in the $[001]$ direction (black arrow); a) 1T tetragonal monodomain state; b) 4R rhombohedral engineered domain state; c) 4O orthorhombic engineered domain state.

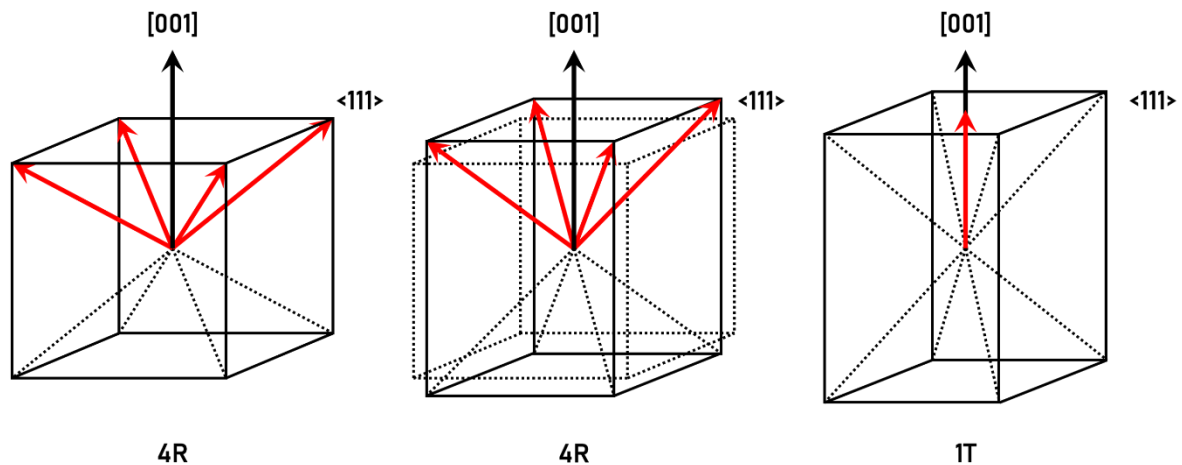


Figure 10 - a) Pseudocubic cell with four equivalent rhombohedral domain states (4R) after poling in $[001]$ direction; b) inclination of the 4R domain states towards the $[001]$ direction of the applied electric field with accompanying lattice strain; c) electric field induced transformation resulting in collapse of equivalent domain states into the 1T tetragonal monodomain state. Adapted from Park & Shrout⁸¹.

Rhombohedral single crystals poled in the $[001]$ direction have dipoles aligned along four $\langle 111 \rangle$ spontaneous polarisation directions, forming four energy equivalent domain states with low driving force for domain wall motion (Figure 10a). Under an applied electric field along the nonpolar $[001]$ direction, the polarisation vector of each domain variant inclines close to the $[001]$ direction, resulting in an equal rhombohedral lattice distortion (strain) within each domain (Figure 10b). The energy equivalency of the domain variants does not permit for domain wall motion to occur in response to the applied electric field, resulting in anhysteretic behaviour. Continued polar vector inclination results in

a collapse of the four equivalent domain states into a single mono-domain state, i.e. an electrically induced rhombohedral-tetragonal phase transition (Figure 10c) ⁸⁴.

Another feature of domain engineering is the resulting change in macroscopic symmetry from local symmetry. The formation of four equivalent engineered domain states with local rhombohedral $3m$ symmetry gives rise to an averaged macroscopic tetragonal $4mm$ symmetry ⁸⁵. Coinciding with the reports of enhanced piezoelectric response in [001]-oriented rhombohedral PZN-PT single crystals, a maximum $d_{33}^*(\vartheta)$ for rhombohedral PZT thin films oriented at angle ($\vartheta = 57^\circ$) away from the [111] spontaneous polarisation direction was predicted by Du *et al.* ^{86,87} using phenomenological theory ⁸⁸, based on intrinsic piezoelectric anisotropy (Figure 11). Later, Fu & Cohen ^{89,90} proposed a polarisation rotation model, derived from applied electric field simulations of single crystal BT, to explain the large piezoelectric enhancements reported along nonpolar directions in relaxor-PT based single crystals.

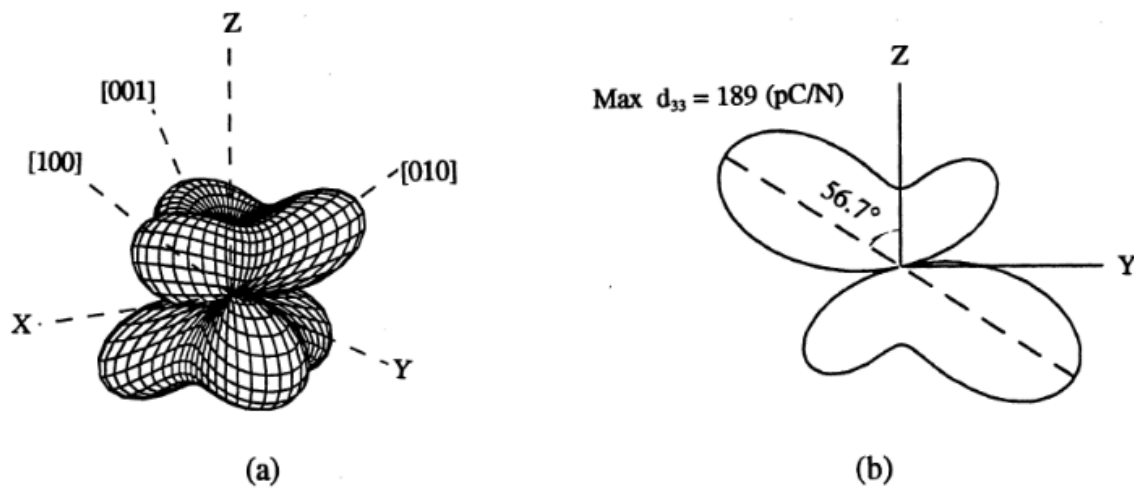


Figure 11 - a) Predicted d_{33} map of rhombohedral 60/40 PZT; b) cross section curve obtained by cutting a) in the Y-Z plane. The distance between origin and any point on the map represents the absolute value of the piezoelectric constant in the corresponding direction. Reproduced from Du *et al.* ⁸⁶.

2.9.1 Polarisation rotation and polarisation extension

To understand the polarisation rotation that occurs in domain engineered single crystals, the change in polarisation vector is considered, ΔP_i , under an applied field in an arbitrary direction, E_j , expressed as ^{72,88}.

$$\Delta P_i = \epsilon_0 \chi_{ij} E_j \quad (17)$$

where ϵ_0 is the permittivity of free space, and χ_{ij} are components of the dielectric susceptibility tensor. For the case of a ferroelectric with spontaneous polarisation $P_s = (0, 0, P_3)$ defined along principal axes (x_1, x_2, x_3) , the application of a parallel electric field, $E = (0, 0, E_3)$, will lead to a change in polarisation vector, $\Delta P = (0, 0, \Delta P_3)$, according to (17). If the electric field is applied perpendicular to the polarisation vector, $E = (E_1, 0, 0)$, the polarisation will rotate away from its initial position by an angle α ⁹¹:

$$\tan \alpha = \frac{\Delta P_1}{P_3} = \frac{\epsilon_0 \chi_{11} E_1}{P_3} \quad (18)$$

The polarisation rotation angle, α , is therefore dependent on the anisotropy of the dielectric susceptibilities, i.e. χ_{11}/χ_{33} , of the material in question⁹². Large transversal dielectric susceptibility, χ_{11} , results in greater polarisation rotation with respect to the applied electric field. Phenomenological theory concerned with macroscopic material properties, gives rise to fundamental intrinsic relations between dielectric susceptibilities, electrostrictive coefficients, and piezoelectric coefficients^{70–72,88,93}:

$$d_{ijk} = 2\epsilon_0 \chi_{mk} Q_{ijmn} P_n \quad (19)$$

The relations for a tetragonal crystal with $4mm$ point group are given as⁹²:

$$d_{33} = 2\epsilon_0 \chi_{33} Q_{11} P_3 \quad d_{31} = 2\epsilon_0 \chi_{33} Q_{12} P_3 \quad d_{15} = \epsilon_0 \chi_{11} Q_{44} P_3 \quad (20)$$

It is clear from (20) that the intrinsic longitudinal, d_{33} , and shear, d_{15} , piezoelectric coefficients are affected by longitudinal, χ_{33} , and transversal, χ_{11} , dielectric susceptibilities. The longitudinal piezoelectric coefficient, $d_{33}^*(\vartheta)$, measured at an arbitrary angle ϑ away from the polar direction, i.e. $\vartheta \neq 0$, consisting of contributions from longitudinal, transversal, and shear piezoelectric coefficients, for tetragonal crystals with $4mm$ point group is given by⁹¹:

$$d_{33}^*(\vartheta) = \cos[(d_{15} + d_{31}) \sin^2 \vartheta + d_{33} \cos \vartheta] \quad (21)$$

Therefore, whenever the shear piezoelectric coefficient is large with respect to the longitudinal piezoelectric coefficient there will be a propensity for the $d_{33}^*(\vartheta)$ to be large away from the polar direction, as seen experimentally in relaxor-PT based single crystals^{4,5,81–83}. The possibility for large polarisation rotation to occur in near MPB PZT compositions can be inferred from previous phenomenological work in a series of papers by Ishibashi & Iwata^{94–100}, reporting that the stability of both tetragonal and rhombohedral PZT necessitates a divergence of transversal dielectric susceptibilities either side of the MPB. This divergence, perpendicular to the spontaneous polarisation direction, is termed ‘transversal instability’, and results in large piezoelectric anisotropy, i.e. divergence between shear and longitudinal piezoelectric coefficients ((20), along with an increase in shear elastic compliance and electromechanical coupling constants⁹⁷. The transversal instability associated with the MPB in the PZT system can be considered compositionally driven. Damjanovic *et al.*¹⁰¹ and Budimir *et al.*¹⁰² have shown large $d_{33}^*(\vartheta)$ values in the vicinity of ferroelectric-ferroelectric phase transitions (tetragonal-orthorhombic-rhombohedral) on cooling BT, highlighting temperature driven transversal instabilities and resulting piezoelectric anisotropy. A common flattening of the Gibbs free energy profile, i.e. free energy instability, has been shown for reported temperature, composition, and electric field induced piezoelectric enhancements along nonpolar directions^{103,104}. Approaching a ferroelectric-ferroelectric phase transition, irrespective of the driving force, results in both ferroelectric phases becoming energetically degenerate. Large transversal dielectric softening, along with increasing piezoelectric anisotropy, develops in anticipation of a change in polarisation direction in the ferroelectric phase on the other side of the boundary. This is realised by easy paths for polarisation rotation, with increasing shear piezoelectric coefficient (d_{15}), resulting in giant $d_{33}^*(\vartheta)$ ¹⁰⁵. As both the transversal instability and piezoelectric anisotropy arise from the flattening of the Gibbs free energy profile, it follows that the free energy instability at ferroelectric-ferroelectric phase transitions is critical in determining the tendency of polarisation rotation and resulting large $d_{33}^*(\vartheta)$. The large intrinsic $d_{33}^*(\vartheta)$ response of relaxor-PT based systems with respect to PZT can be explained by their near ambient ferroelectric-ferroelectric phase transitions and resulting huge d_{15} contribution (> 2000 pC/N)¹⁰⁶.

It is important to note that not all piezoelectric materials exhibit a maximum $d_{33}^*(\vartheta)$ along nonpolar direction (polarisation rotation). Polarisation extension, whereby the maximum $d_{33}^*(\vartheta)$ is found along spontaneous polarisation directions, i.e. $\vartheta = 0$, occurs in the case of PT. The d_{15} in PT at ambient temperatures is not large enough to bring about a maximum $d_{33}^*(\vartheta)$ away from the [001] spontaneous polarisation direction¹⁰⁵. However, it has been seen experimentally that a large piezoelectric enhancement of PT is possible under compressive stress induced phase transformations exhibited along nonpolar directions^{107–109}. It can be said that in the absence of any ferroelectric-ferroelectric transition, and therefore free energy instability, there is a tendency for ferroelectric materials to exhibit dominant polarisation extension. The terms ‘rotator’ and ‘extender’ ferroelectric have been coined to distinguish ferroelectric materials depending on the nature of their piezoelectric response⁹¹. Rotator ferroelectrics

have a piezoelectric anisotropy (d_{15}/d_{33}) above a critical value, whereby polarisation rotation is the dominant mechanism with the maximum $d_{33}^*(\vartheta)$ found away from the spontaneous polar axes. Extender ferroelectrics have a d_{15}/d_{33} below a critical value, whereby polarisation extension/contraction is the dominant mechanism of piezoelectric response with the maximum $d_{33}^*(\vartheta)$ found along the spontaneous polar axes. There is a firm consensus in the case of PZT compositions in the vicinity of the MPB, that the dominant intrinsic mechanism for the large piezoelectric response is via polarisation rotation, arising from the structural instabilities around the compositionally driven ferroelectric-ferroelectric transition (MPB) ¹¹⁰.

Utilisation of this enhanced piezoelectric response seen in oriented single crystals is the main driving force to obtain textured polycrystalline ceramics. Single crystal growth methods have several reported difficulties in synthesising homogeneous crystals ^{111,112}, whilst being costly and time consuming to fabricate. [001]-textured polycrystalline ceramics are expected to have the same macroscopic symmetry as [001]-oriented single crystals, and therefore theoretically exhibit reduced hysteresis and greatly enhanced piezoelectric coefficients at a fraction of the cost of synthesising single crystals. Ceramics also exhibit better mechanical properties compared to single crystal counterparts. Textured ceramics, whereby all the grains are oriented in a certain crystallographic direction, are potentially able to be domain engineered if sufficient microstructural control is attained, realising the large piezoelectric enhancement for ‘rotator’ ferroelectrics. In the case of texturing ‘extender’ ferroelectrics, the alignment of grains in specific orientations can alleviate the problem of grain clamping, whereby there are no domain states near the direction of the field resulting in clamping of adjacent grains, hindering them from switching. The greater alignment of polar domains to the applied field, i.e. poling efficiency, and facilitated domain wall motion, results in a larger volume fraction of the material contributing to the overall piezoelectric response compared with randomly oriented ceramics ²³.

2.10 Monoclinic phase

There exists no direct symmetry relation between the tetragonal, $P4mm$, and rhombohedral, $R3m$, phases in the PZT system. Noheda *et al.* ¹¹³ first reported the appearance of a lower symmetry monoclinic phase (space group Cm , no. 8) separating both tetragonal and rhombohedral PZT phases. The monoclinic Cm phase shares a mirror plane with both tetragonal, $P4mm$, and rhombohedral, $R3m$, structures. The proposed monoclinic unit cell for PZT (a_m , b_m , c_m , β) is rotated 45° (angle α) about the tetragonal c -axis, where a_m and b_m lie on the face diagonals of the prism base, with c_m tilted away from tetragonal c -axis by an angle $90^\circ - \beta$ (Figure 12) ¹¹⁴.

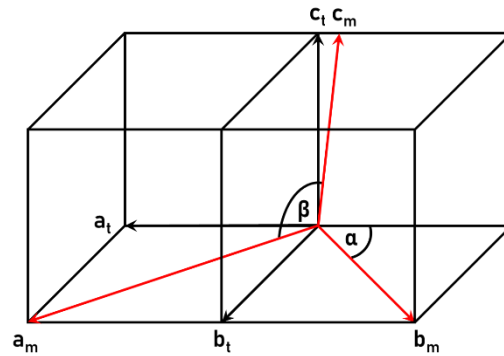


Figure 12 - Tetragonal (a_t , b_t , c_t) and monoclinic (a_m , b_m , c_m , β) unit cell representations. Adapted from Noheda *et al.* ¹¹³.

Corker *et al.* ¹¹⁵ proposed an additional off axis displacement of Pb^{2+} along three $\langle 100 \rangle$ directions, which average out to net zero, occurring on local $[111]$ shifts to explain strong anisotropic thermal factors obtained from Rietveld refinement of rhombohedral PZT. The ordering of these displacements along one of the $\langle 100 \rangle$ directions could potentially accommodate a distinct rhombohedral-monoclinic (R-M) phase transition. Further Rietveld analysis by Noheda *et al.* ¹¹⁶, aimed at deriving a possible tetragonal-monoclinic (T-M) phase transition, reported random Pb^{2+} $\langle 110 \rangle$ shifts in one of four different directions to occur on local displacements along the $[100]$ direction in tetragonal PZT. Again, the ordering of shifts along one of the $\langle 110 \rangle$ directions predicated could accommodate a possible T-M transition. The described random Pb atomic displacements in both tetragonal and rhombohedral PZT result in a local monoclinic distortion.

Poling *in-situ* X-ray diffraction studies by Guo *et al.* ¹¹⁷ found both rhombohedral and tetragonal PZT to exhibit elongations along directions associated with the previously reported monoclinic distortion ^{115,116}. Although this work did not consider the coupling of extrinsic non- 180° domain switching to intrinsic lattice strain through intergranular stresses induced during polling, identified by Hall *et al.* ¹¹⁸ from XRD analysis of $\{111\}_t$ and $\{200\}_r$ lattice spacings. First-principle modelling by Bellaiche *et al.* ¹¹⁹ also found agreement with the presence of a monoclinic phase between rhombohedral and tetragonal PZT at zero-field, and subsequently under applied electric field ¹²⁰. The existence of a monoclinic phase in the PZT system can be explained using the polarisation rotation framework, whereby the polarisation can rotate freely within certain monoclinic planes found between the $[001]$ and $[111]$ polar axes of the tetragonal and rhombohedral phases, allowing for a continuous structural change between tetragonal and rhombohedral phases across the MPB ¹²¹. A phenomenological derivation of three possible monoclinic phases: M_A ($c_m > a_m, b_m$) and M_B ($c_m < a_m, b_m$) both with space group Cm , and M_C with space group Pm was reported by Vanderbilt & Cohen ¹²². In both monoclinic structures the polarisation is no longer constrained to a symmetry axis as in the higher symmetry phases (tetragonal, rhombohedral, orthorhombic), but rather a symmetry plane. In the M_A and M_B phases the polarisation is constrained

within the monoclinic ($1\bar{1}0$) plane (Figure 13a and Figure 13b), whilst in the M_C phase the polarisation is constrained within the monoclinic (010) plane (Figure 13c).

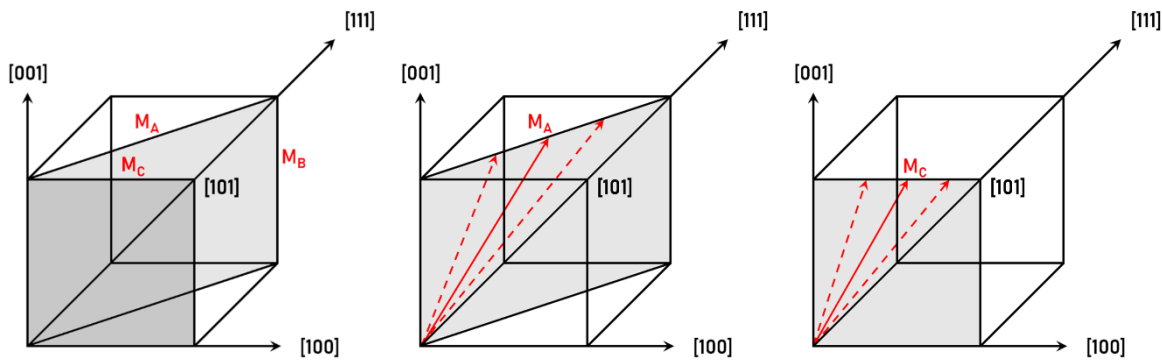


Figure 13 - a) Schematic of perovskite unit cell with M_A and M_B (110) plane (light shaded area), M_C (010) plane (dark shaded area); b) polarisation vector (solid red arrow) rotating within monoclinic M_A plane, between tetragonal $[001]$ and rhombohedral $[111]$ spontaneous polarisation directions; c) polarisation vector rotating within monoclinic M_C plane, between tetragonal $[100]$ and orthorhombic $[101]$ spontaneous polarisation direction.

The M_A phase has since been identified in PZT by high resolution diffraction studies, acting as an apparent structural bridge between the two ferroelectric phases¹¹⁴. The large increase in piezoelectric response in PZT near the MPB can be explained by the polarisation continually adjusting to the applied field via polarisation rotation through monoclinic distortions, although it is important to make the distinction that the origin of such enhancement is not symmetry related, i.e. due to the monoclinic phase, as the dielectric susceptibility is larger on the tetragonal side of the monoclinic-tetragonal boundary than within the monoclinic region¹²³.

The appearance of lower symmetry phases in the vicinity of MPBs has also been reported in PZN-PT and PMN-PT systems. X-ray diffraction studies by Cox *et al.*¹²⁴ found the appearance of an orthorhombic phase between tetragonal and rhombohedral phases in PZN-9PT single crystals. The monoclinic M_A phase has been reported in near-MPB composition PMN-35PT¹²⁵. Further neutron diffraction studies by Bai *et al.*¹²⁶ reported a discontinuous jump in polarisation path between M_A and M_C phases in PMN-30PT single crystals. Applied field experiments by Noheda *et al.*¹²⁷ on PZN-4.5PT and PZN-8PT¹²⁸ single crystals found differing polarisation rotation paths through both monoclinic M_A and M_C phases, highlighting a strong sensitivity of rotation path to crystal composition due to the near energy degeneracy of the different phases around the MPB. Davis *et al.*^{129,130} reported hysteretic electric field induced phase transitions via intermediary monoclinic (or orthorhombic) phases in PZN-PT and PMN-PT single crystals, indicating abrupt phase transformations. Partial following of polarisation paths, e.g. jump from M_A plane to M_C plane as seen by Bai *et al.*¹²⁶ and Davis *et al.*^{129,130}, suggests first-order transformations between monoclinic phases which are not completely reversible. Previous

phase diagrams for PZT by Jaffe *et al.*³², PZN-PT by Kuwata *et al.*⁴, and PMN-PT by Choi *et al.*¹³¹, have all been modified in light of the discovery of new phases in the vicinity of the MPB (Figure 14).

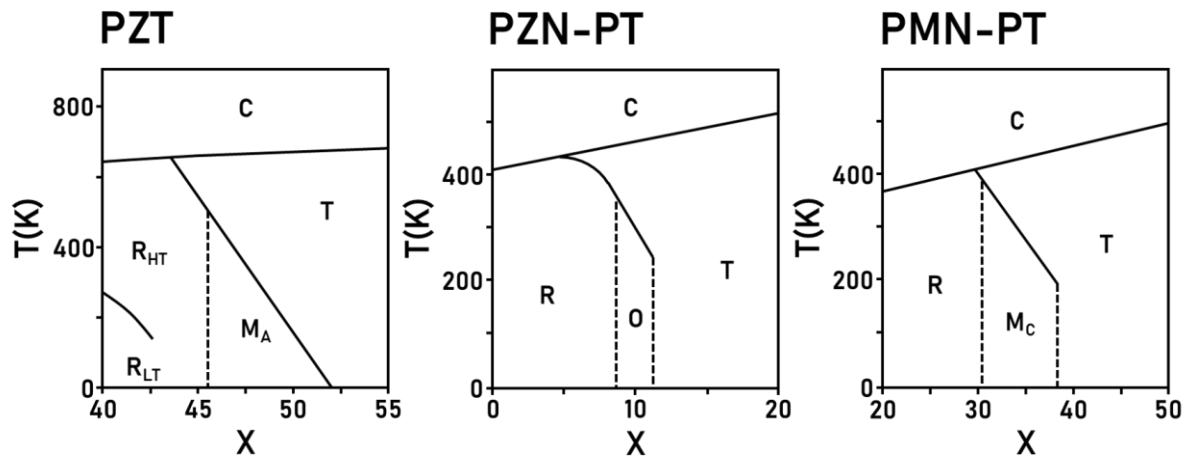


Figure 14 - a) Modified PZT phase diagram near MPB adapted from Jaffe *et al.*³²; b) modified PZN-PT phase diagram near MPB adapted from Kuwata *et al.*⁴; c) modified PMN-PT phase diagram near MPB adapted from Choi *et al.*¹³¹. Reproduction from Noheda¹¹⁴.

2.11 Adaptive phase

There is continuing debate as to whether there is a definite monoclinic phase boundary or whether it manifests as an increasingly coherent monoclinic distortion, i.e. change in range of order, within both parent tetragonal and rhombohedral structures as the MPB is approached^{132,133}. It has been proposed that uncorrelated monoclinic distortions occur throughout the PZT phase diagram, as the MPB is approached, the correlation length increases, resulting in the appearance of a monoclinic phase¹³⁴. This is supported by the reported lack of a distinct phase boundary between rhombohedral and monoclinic PZT structures and expected discontinuous transition between the two phases. Veihland¹³⁵ and Jin *et al.*¹³⁶ both proposed an ‘adaptive phase’ model to explain the apparent monoclinic phases reported in both PZN-PT and PMN-PT systems, based on a principle assumption that domain size would decrease drastically with decreasing domain wall energy. The near energy isotropy at the MPB implies a reduction in domain wall energy, and therefore domain size. Such a reduction in domain size has been reported by Wada *et al.*^{137,138} to directly affect the extrinsic piezoelectric contribution in domain engineered BT. Jin *et al.*¹³⁹ reported the miniaturisation of stress accommodating tetragonal domain states, exhibiting plate-like topology consisting of alternating twin-related domains, i.e. two tetragonal domain variants with polarisation along [100] and [001] respectively, forming an adaptive phase. The lattice parameters of this adaptive phase would appear macroscopically in X-ray and neutron diffraction studies as a monoclinic phase. Wang^{140,141} proposed an adaptive diffraction phenomenon to explain the identification of the monoclinic M_c phase from the averaging of tetragonal twin nanodomains, and

monoclinic M_A and M_B phases from the averaging of rhombohedral twin nanodomains. In the case of the adaptive phase, polarisation rotation would be realised by an increase in volume fraction of one nanodomain variant via domain wall motion. The lack of hysteresis seen in domain engineered single crystals can be explained within the adaptive phase framework by the minimised domain wall energy near the MPB, allowing for easy domain wall motion.

Experimental work by Yin & Cao ¹⁴² analysing the domain patterns of $[001]_c$ -poled rhombohedral PZN-4.5PT single crystals reported large twins (10-100 μm) containing only two of the four possible engineered domain states along with both charged and uncharged domain walls, indicating more complex domain patterns than previously assumed in domain engineered single crystals. Although the theoretical basis for charge domain walls is disputed ¹⁴³. Erhart & Cao ¹⁴⁴ predicted orthorhombic $mm2$ symmetry as the highest macroscopic symmetry in systems with two domain variants, with a lower monoclinic m symmetry obtained by varying the volume ratios of the two domain states ¹⁴⁵, as proposed by the adaptive phase model. Further experimental studies found the existence of orthorhombic $mm2$ symmetry in $[001]_c$ -poled rhombohedral PZN-4.5PT single crystals ¹⁴⁶. A similar twin domain pattern has been seen in $[001]_c$ -poled rhombohedral PMN-32PT single crystals ¹⁴⁷. Woodward *et al.* ¹⁴⁸ reported frustrated domain patterns in MPB composition PZT, with domain sizes limited to ~ 20 nm, arising from local ion clustering. The local distribution of Zr/Ti throughout the sample will therefore directly affect the distribution of domain walls and their habit planes ¹⁴⁹. It can be understood that both the monoclinic phase model and adaptive phase model can arise from the same flattening of the free energy profile ¹⁵⁰. Recent HRTEM work by Sato *et al.* ¹⁵¹ on PMN-PT single crystals reported monoclinic nanodomains which exhibit a reversible reorientation response under applied field allowing for anhysteretic strain-field curves.

2.12 Templated grain growth

Templated grain growth (TGG) is a method utilised to fabricate textured ceramics. Both fibre (axial) and sheet (biaxial) texture can be achieved, however in most cases fibre texture is sufficient to maximise the properties of interest. Fibre texture describes the case where grains are aligned in only a single crystallographic direction, whereas sheet texture involves grains being aligned in all three crystallographic directions. Sheet texture is considerably harder to attain, requiring simultaneous alignment of two crystallographic directions. Prior to green processing, large template particles are added and dispersed within the fine matrix powder in a carrier slurry designed to give suitable rheological properties for slip casting. Tape casting is employed to orient and align these template particles before TGG. During tape casting, a shear field is generated as the slurry is drawn under the doctor blade. The resulting torque acting on the templates rotates and aligns them parallel to the casting direction. The degree and quality of texture is primarily dependent on satisfactory template alignment during tape casting. If the template material is identical to the matrix, homoepitaxy occurs, with template

growth at the expense of the matrix powder encouraged during heat treatment ¹⁵². Several factors, reported initially in alumina ($\alpha\text{-Al}_2\text{O}_3$) systems, including a > 1.5 ratio of template thickness to matrix grain size, and template concentration less than a critical value required to achieve a narrow orientation distribution, must be satisfied for successful TGG ^{153,154}.

The driving force for homoepitaxial TGG is the difference in solubility between the large template particles and fine matrix. Ostwald ripening is driven by this difference, coarsening the large template particles at the expense of the fine matrix ¹⁵⁵. In the case where the template material is different to the matrix, heteroepitaxy occurs, with the growth of the newly nucleated grains on the template surface encouraged. The template material acts as an epitaxial substrate from which oriented grains can nucleate and grow. TGG in this case is primarily dependent on both physical and chemical properties of both matrix and template materials. The driving force for heteroepitaxial TGG involves the equilibrium solubilities of the matrix and template particles and their respective free surface energies. In conventional TGG, the matrix powder is in the form of the desired final phase. If the matrix powder is not in the desired final phase, i.e. the matrix powder is a mixture of precursor oxides, the process is termed 'reactive' templated grain growth (RTGG). In RTGG, the template particles act similar as in the heteroepitaxial TGG case, with the combined role of providing nucleation sites for the desired phase formation and imparting the desired texture during grain epitaxy. The principle for texturisation by TGG is illustrated in Figure 15-Figure 16.

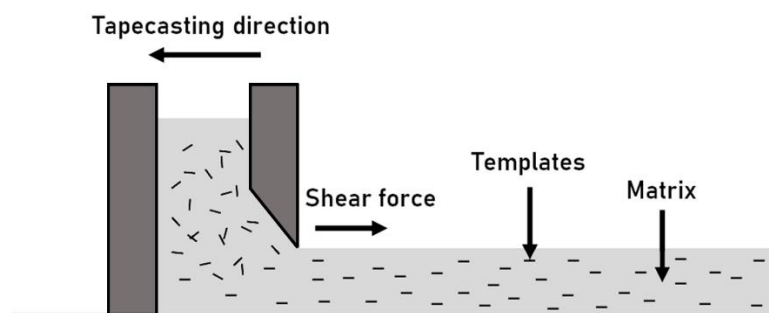


Figure 15 - Schematic of template alignment by tapecasting. Reproduction from Messing *et al.* ²³.

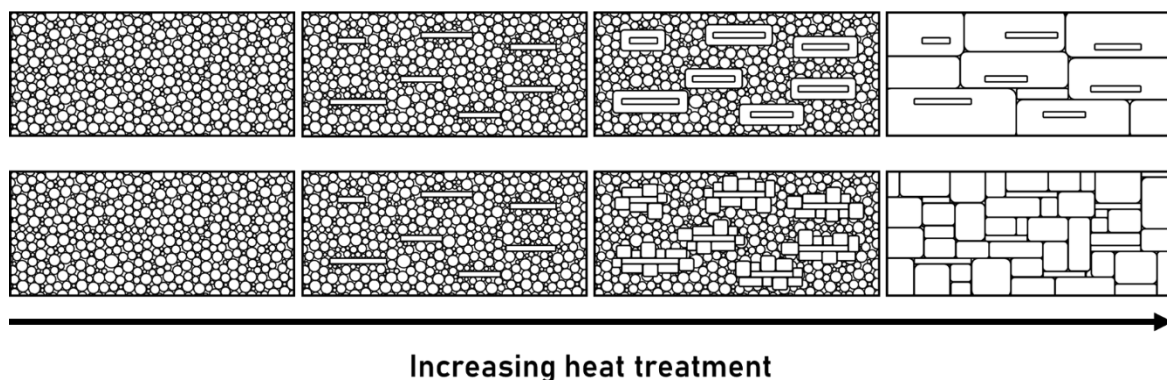


Figure 16 - Schematic of texture evolution via different texturing mechanisms with increasing sintering time (left to right); (top) continuous textured layer forms prior to substantial grain growth; (bottom) discontinuous layer forms with several nucleation sites on template interface before coarsening. Adapted from Moriana & Zhang ¹⁵⁶.

Irrespective of whether the matrix is in the desired phase or a mixture of precursors, the grain size must be sufficiently small when compared with the templates, to maintain the driving force for TGG after initial densification. This requires attaining small starting matrix particle sizes prior to green body fabrication and heat treatment. The ceramic body must achieve sufficient density prior to grain coarsening, as any porosity will hinder subsequent grain growth. Liquid phase formers can be added to help relieve the stresses formed around the template particles from constrained sintering and further aid in exaggerated grain growth. The size distribution of the template particles and vol. % loading is critical in moderating the impingement of growing textured grains. The boundaries between impinged grains have a lower driving force for grain growth, resulting in a significant decrease in overall growth rate. Once significant impingement has occurred, further heat treatment times will have a reduced effect on promoting further textured grain growth. Reported piezoelectric enhancement via TGG of first/second/third generation relaxor-PT based systems are shown in Table 2.

Table 2 - Comparison between piezoelectric coefficients of reported [001]-textured Pb-based perovskite ceramics.

Material composition	Reference	Template material	$f_{(001)}$	d_{33} (pC/N)
PMN-32.5PT	ref. ¹⁵⁷	5 vol. % BT	0.90	*1150
PMN-32.5PT	ref. ¹⁵⁸	5 vol. % ST	0.69	*1660
PMN-32PT	ref. ¹⁵⁹	5 vol. % BT	0.99	877
PMN-25PT	ref. ¹⁶⁰	7 vol. % NBT-0.6PT	0.92	†855
Mn-doped PMN-25PT	ref. ¹⁶⁰	7 vol. % NBT-0.6PT	0.49	†517
PMN-32.5PT	ref. ¹⁶¹	1 vol. % BT	0.98	1000
PMN-37PZ-21PT	ref. ¹⁵⁹	5 vol. % BT	0.94	*878
PMN-25PZ-35PT	ref. ¹⁶²	5 vol. % BT	0.90	1100
Mn-doped PMN-25PZ-35PT	ref. ¹⁶³	3 vol. % BT	0.93	720
PIN-40PMN-32PT	ref. ¹⁶⁴	5 vol. % BT	0.93	824
PIN-30PMN-34PT	ref. ¹⁶⁵	5 wt. % BT	0.95	780
Mn-doped PIN-40PMN-35PT	ref. ¹⁶⁶	5 vol. % BT	0.90	*846
PYN-46.5PMN-38PT	ref. ¹⁶⁷	5 vol. % BT	0.91	*1340
PYN-41PMN-38PT	ref. ¹⁶⁸	5 vol. % BT	0.93	*754

* denotes values obtained from strain-electric field curves at low field (< 5 kV/cm).

† denotes values obtained from resonance-antiresonance measurements.

Seabaugh *et al.* ¹⁶⁹ reported the first case of TGG utilising tapecasting to texture α -Al₂O₃ ceramics. Since then, several publications on TGG of Pb-based piezoelectric ceramics utilising various template materials have emerged. PMN-32.5PT ceramics were first successfully textured by Sabolsky *et al.* ¹⁵⁷ using 5 vol. % (001)-oriented BT templates (> 75 μ m). Measured d_{33}^* and T_c values were 1150 pC/N and 164 °C respectively, however the resulting large grain sizes (> 100 μ m) diminished the overall mechanical properties of the ceramic. Work by Kwon *et al.* ¹⁵⁸ on utilising SrTiO₃ (ST) templates to texture PMN-32.5PT, found ST would preferentially dissolve into the matrix at temperatures > 1150 °C. This resulted in a lowered T_c of 120 °C, with an improved low-field d_{33}^* of 1660 pC/N. A low temperature annealing step prior to sintering resulted in textured grain epitaxy on the template surface prior to dissolution. There exists a general trend of T_c values being depressed for textured ceramics, originating from the inclusion of heterogeneous templates with lower Curie temperatures, e.g. BT with $T_c \sim 130$ °C, ST with $T_c \sim -168$ °C. The interdiffusion of less polarisable aliovalent A-site cations (Ba²⁺, Sr²⁺) into the matrix is known to lower the T_c of the final matrix phase. Subsequent work on PMN-PT was aimed at developing and utilising smaller templates with suitable geometries to attain finer textured grain sizes. Richter *et al.* ¹⁵⁹ produced near completely [001]-textured PMN-32PT and PMN-37PZ-21PT ceramics (reported $f_{(001)} \sim 0.99$ for PMN-PT and 0.94 for PMN-PZT) using 5 vol. % BT templates

(~ 10 μm). The PMN-PZT ceramic exhibited a greater T_c of 216 °C and comparable d_{33}^* of 878 pC/N to PMN-PT. Greater piezoelectric enhancement of [001]-textured PMN-32.5PT by Yan *et al.*¹⁶¹ was achieved by reducing the BT template addition to 1 vol. %. Static d_{33} of 1000 pC/N and T_c 162 °C were reported. This increase, when compared with 5 vol. % BT additions, is explained by the stability of BT in the PMN-PT matrix resulting in residual BT inclusions. The low piezoelectric activity of BT ($d_{33} \sim 190$ pC/N) reduces the strain response of the textured ceramic due to mechanical clamping. Poterala *et al.*¹⁶⁰ utilised 7 vol. % NBT-0.6PT platelets to textured PMN-PT ceramics, alleviating the problem of residual template inclusions. A d_{33} of 855 pC/N and T_c of 129 °C was reported, with Mn-doped PMN-PT ceramics having a d_{33} of 517 pC/N and T_c of 130 °C. Recent efforts have been focused on texturing new relaxor-PT based systems with higher T_{r-f} and T_c values. Chang *et al.*¹⁶⁴ obtained a large d_{33} of 824 pC/N and improved T_c of 203 °C in textured PIN-40PMN-32PT ceramics (reported $f_{(001)} \sim 0.93$) using 5 vol. % BT. Beecher *et al.*¹⁶⁶ reported successful RTGG of Mn-doped PIN-PMN-PT ceramics utilising CuO as a low temperature sintering aid, with a slightly improved T_c of 219 °C and low-field d_{33}^* of 846 pC/N. TGG of other ternary Pb-based systems, e.g. PYN-PMN-PT, with improved T_c suitable for high power transducer applications, have also been studied extensively with a new focus on lowering sintering temperatures¹⁶⁸. Much of the literature on TGG to date is concerned with binary and ternary relaxor-PT based systems, e.g. PMN-PT, PIN-PMN-PT.

2.13 Template synthesis

Several template parameters need to be fulfilled to achieve successful texturisation via TGG. Template particles must have a similar crystal structure to the matrix material, with small lattice mismatch, to enable the desired phase to nucleate and grow during heat treatment. As liquid phase formers may be added to aid densification and grain growth, the template material must have sufficient stability within the liquid phase/matrix material so as not to dissolve prior to the epitaxy of oriented nuclei or form any secondary phases hindering initial epitaxy. After nucleation of textured grains has occurred, the template material is no longer required to be chemically inert and may go into solution with the surrounding matrix. This is more important in the case of using heterogenous templates, whereby dissolution after textured nucleation can result in better piezoelectric properties due to there no longer being a difference in polarisation between the matrix and the template material.

The template particles must have an anisometric morphology with a high aspect ratio, e.g. platelets, whiskers, rods, to allow for orientation under the generated shear field during tapecasting. Ideally the template material would be the same composition as the matrix to avoid substantial reductions in piezoelectric and dielectric properties from the inclusion of remnant secondary phases. However, this is dependent on the ability to synthesise the desired material in suitable particle morphologies. Conventional molten salt synthesis methods for growing cubic perovskite materials usually result in equiaxed crystallites that do not possess suitable aspect ratios to be easily aligned via tapecasting¹⁷⁰⁻

¹⁷². To produce high aspect ratio templates of cubic perovskites, growth along certain crystallographic directions must be constrained. Strong anisometric growth results from anisotropic surface energies/nucleation energies introduced by poisoning crystal growth on specific crystallographic faces, achieved primarily using melt dopants. Reported melt dopants include MnCl_2 ¹⁷³, PbCl_2 ¹⁷⁴, LiF ^{173,174}, LiCl ¹⁷⁴, NaF ¹⁷⁴. The addition of alkaline halide salts into the molten melt can control resulting particle size and morphology due to the interactions between the large anions/cations present in the molten salt and the forming crystallographic faces of the perovskite structure.

The formation of anisometric particles of conventional perovskites is inherently hindered during molten synthesis due to the high crystal symmetry of the structure (cubic above T_c) at the required melt temperatures (melting points of NaCl ~ 801 °C and KCl ~ 770 °C respectively). Moon *et al.* ¹⁷⁵ first reported successfully synthesising PT crystallites with tabular morphology via hydrothermal synthesis at low supersaturations, circumventing the problems identified with molten salt synthesis. Takeuchi *et al.* ^{176,177} first reported epitaxial growth of ST on tabular $\text{Sr}_3\text{Ti}_2\text{O}_7$, and PT on platelet $\text{Bi}_4\text{Ti}_3\text{O}_{12}$ particles during hydrothermal synthesis. $\text{Sr}_3\text{Ti}_2\text{O}_7$ has a Ruddlesden-Propper layered perovskite structure, whilst $\text{Bi}_4\text{Ti}_3\text{O}_{12}$ has an Aurivillius structure. Both structures have large crystal anisotropy ($a \ll c$), forming platelets with large (001)-faces from molten synthesis methods. Watari *et al.* ¹⁷⁸ found similar epitaxial growth via a molten salt synthesis route by reacting $\text{Sr}_3\text{Ti}_2\text{O}_7$ with excess TiO_2 in a KCl molten flux. The resulting ST platelets had an 10-20 μm edge length, with ~ 2 μm thickness. The continued growth of ST inwards, consuming the $\text{Sr}_3\text{Ti}_2\text{O}_7$ precursor phase, reinforced the possibility of synthesising anisotropic cubic perovskite materials from layer perovskite precursors. The use of ‘structural’ precursors has since been termed topochemical microcrystal conversion (TMC). Saito *et al.* ¹⁷⁹ reported a new 2-step synthesis method for plate-like NaNbO_3 (NN) via TMC of bismuth layered structure $\text{Bi}_{2.5}\text{Na}_{3.5}\text{Nb}_5\text{O}_{18}$, (BiNN5), suitable for RTGG of lead-free KNN piezoelectrics (Table 3). Further work by Saito & Takao ¹⁸⁰ developed a 2-step method for synthesising (001)-platelet ST particles from precursor Aurivillius $\text{SrBi}_4\text{Ti}_4\text{O}_{15}$ (SBIT) reacted at much lower temperatures (950 °C).

Table 3 - Reported synthesis sequences for NN, ST, and BT template materials with suitable morphologies for use in TGG.

ref. Yan <i>et al.</i> ¹⁸¹	ref. Saito & Takao ¹⁸⁰	ref. Liu <i>et al.</i> ¹⁸²
$5\text{Bi}_2\text{O}_3 + 10\text{Nb}_2\text{O}_5 + 7\text{Na}_2\text{CO}_3$ (NaCl flux) ↓*	$\text{SrCO}_3 + 2\text{Bi}_2\text{O}_3 + 4\text{TiO}_2$ (KCl flux) ↓*	$2\text{Bi}_2\text{O}_3 + 3\text{TiO}_2$ (1:1 NaCl:KCl flux) ↓*
$4\text{Bi}_{2.5}\text{Na}_{3.5}\text{Nb}_5\text{O}_{18} + 7\text{CO}_2$	$\text{SrBi}_4\text{Ti}_4\text{O}_{15} + \text{CO}_2$	$\text{Bi}_4\text{Ti}_3\text{O}_{12}$
$4\text{Bi}_{2.5}\text{Na}_{3.5}\text{Nb}_5\text{O}_{18} + 3\text{Na}_2\text{CO}_3$ (NaCl flux) ↓†	$\text{SrBi}_4\text{Ti}_4\text{O}_{15} + 3\text{SrCO}_3$ (KCl flux) ↓†	$\text{Bi}_4\text{Ti}_3\text{O}_{12} + \text{BaCO}_3 + 4\text{TiO}_2$ (1:1 BaCl ₂ :KCl flux) ↓*
$20\text{NaNbO}_3 + 10\text{Bi}_2\text{O}_3 + 3\text{CO}_2$	$4\text{SrTiO}_3 + 2\text{Bi}_2\text{O}_3 + 3\text{CO}_2$	$\text{BaBi}_4\text{Ti}_4\text{O}_{15} + \text{CO}_2$
		$\text{BaBi}_4\text{Ti}_4\text{O}_{15} + \text{BaCO}_3$ (1:1 NaCl:KCl flux) ↓†
		$2\text{BaTiO}_3 + 2\text{Bi}_2\text{O}_3 + \text{CO}_2$

* denotes molten salt synthesis (MSS) reaction of precursors.

† denotes topochemical microcrystal conversion (TMC) reaction of desired phase.

Several TMC methods specific to BT have also been reported for fabrication of particles with anisometric crystal faces. Suitable (001) BT platelets with edge lengths between 5-10 μm, and thicknesses ~ 0.5 μm were synthesised by Liu *et al.* ¹⁸² from the conversion of BaBi₄Ti₄O₁₅. (110)- and (111)-oriented BT microcrystals have also been reported utilising specific topotaxial relations of various precursor materials ^{183,184}. The versatility of Aurivillius phases in TMC, with structural formula [Bi₂O₂]_{A_{n-1}B_nO_{3+n}}, where *n* is the number of pseudo-perovskite blocks in between the [Bi₂O₂]²⁺ interlayers (Figure 17), is evident from its reported use to fabricate various perovskite templates. Aurivillius structures exhibit wide compositional flexibility in incorporating various cations such as Na⁺, K⁺, Ca²⁺, Sr²⁺, Ba²⁺, Pb²⁺, Bi³⁺, Ln³⁺ on A-sites, and higher valence cations such as Fe³⁺, Cr³⁺, Ti⁴⁺, Nb⁵⁺, W⁶⁺ on B-sites ¹⁸². However, there is an added complexity in the need to remove the [Bi₂O₂]²⁺ interlayers from the precursor phase, to give the desired perovskite structure.

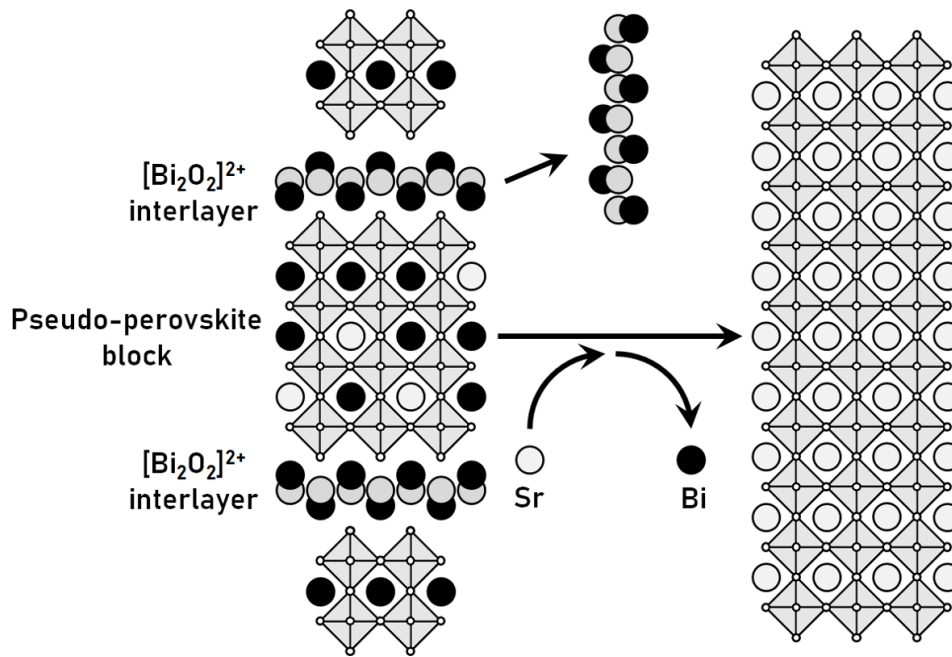


Figure 17 - a) Schematic of Aurivillius SrBi₄Ti₄O₁₅ structure with highlighted [Bi₂O₂]²⁺ interlayers; b) perovskite ST structure after TMC via removal of [Bi₂O₂]²⁺ layer and substitution of Bi³⁺ with Sr³⁺. Adapted from Saito & Takao¹⁸⁰.

Work by Poterala *et al.*¹⁸⁵ provided an in-depth understanding of the topochemical process occurring during BT, PT, and NN platelet synthesis. Intermediate Aurivillius type phases were found to hinder the complete formation of phase pure PT. The incorporation of Na⁺ from the NaCl flux was reported to necessitate the formation of the perovskite phase by charge balancing the persistent Bi³⁺ on the perovskite A-site, resulting in a solid solution of 0.4Na_{0.5}Bi_{0.5}TiO₃-0.6PT¹⁸⁶.

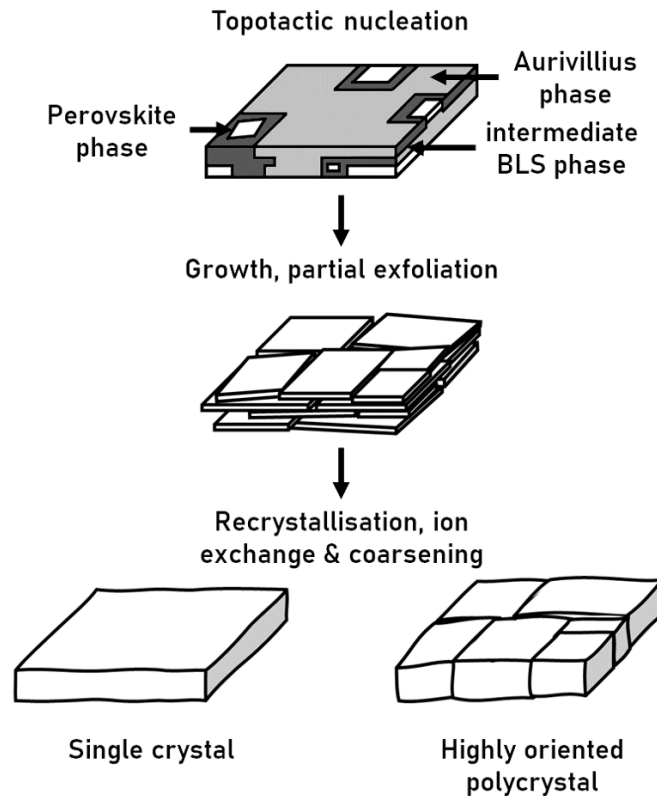


Figure 18 - a) Initial topotactic nucleation of perovskite phase on Aurivillius precursor; b) growth and partial exfoliation of perovskite phase crystallites; c) further recrystallisation and grain growth results in either single crystal or highly oriented polycrystalline template particles. Adapted from Poterala *et al.*¹⁸⁵.

Initial premature exfoliation of the converted microcrystals from the Aurivillius phase substrate can result in the loss of epitaxy, forming oriented perovskite phase polycrystalline aggregates (Figure 18b). Further heat treatment allows for the recrystallisation of the slightly misaligned crystallites into dense perovskite phase platelets (Figure 18c). The resulting perovskite platelets are either coherent single crystals or highly oriented polycrystals, exhibiting low angle grain boundaries. The degree of misalignment is dependent on the temperature and time allowed for recrystallisation and grain growth after exfoliation¹⁸⁵.

2.14 Textured PZT ceramics

There is minimal literature on the successful TGG of PZT, believed to be due to inherent fabrication difficulties seen during PZT single crystal growth. Incongruent melting across the whole PT-PZ system, results in significant segregation of the Zr component from the bulk, and as a result only very small crystals of PZT can be produced by high temperature solution growth¹⁸⁷.

Conventional TGG of PZT has been reported by Muramatsu & Kimura¹⁸⁸ utilising 40 vol. % perovskite layered structure $\text{Ba}_6\text{Ti}_{17}\text{O}_{40}$ (B6T17) templates. A maximum $f_{(111)} \sim 0.6$ was reported, with the resulting crystallographic texture obtained in the [111] orientation. The large vol. % template addition raises questions as to final composition of the bulk material, and whether this in turn, would negatively affect the piezoelectric properties of the textured sample. However, the use of PbO (1 wt. % excess) as a transient liquid phase was identified as critical in enabling texture formation. No textured grain epitaxy was observed in samples without excess PbO. Miwa *et al.*¹⁸⁹ reported a maximum $f_{(001)} \sim 0.77$ for novel [001]-textured PZT multilayers using compositional modification with $\text{Pb}(\text{Ni}_{1/3}\text{Nb}_{2/3})\text{O}_3$ (PNN), magnetically aligned during tapecasting under high magnetic field (9 T), due to the large magnetic moment exhibited by Ni^{2+} ions. Resulting k_{31} values ~ 0.44 , ~ 1.3 times greater than untextured counterparts, were obtained, suggesting that large piezoelectric enhancements of PZT via TGG are experimentally possible.

3. Aims and objectives

The aim of this project is to improve the piezoelectric properties of PZT multilayers by utilising texture in conjunction with appropriate compositional modification. [001]-texture is achieved by TGG of PZT multilayers and the MPB composition is retained through modification of the starting Zr:Ti ratio to accommodate the use of heterogenous seed templates.

The main objectives are:

- i) Synthesis of $x\text{Na}_{0.5}\text{Bi}_{0.5}\text{TiO}_3$ - $1-x\text{PbTiO}_3$ (NBT-PT) templates via topochemical conversion of Aurivillius phase $\text{PbBi}_4\text{Ti}_4\text{O}_{15}$ (PBT) to explore their use as a template material. Alternative perovskite phase materials may be necessary if difficulties arise during the synthesis procedure, from poor template microstructure/morphology or in facilitating satisfactory TGG.
- ii) Anisometric templates will be used to attempt TGG of PZT multilayers to establish a proof of concept. Further investigation of the critical processing parameters necessitating textured grain epitaxy, whilst promoting sufficient densification, is required for further for optimisation. Analysis of the chemical stability and interaction between template material and matrix during TGG will be important to tailor further template and liquid phase additions.
- iii) Modification of the starting Zr:Ti ratio of matrix PZT composition will be conducted to account for the use of heterogeneous template material to obtain textured multilayers close to the MPB, thereby maximising piezoelectric properties. Both microstructural and electric characterisation techniques will be used to determine the optimised starting PZT composition. This optimised composition, along with TGG parameters, will be used to synthesise textured multilayers. TGG of the optimised starting composition is expected to result in a significant enhancement of piezoelectric properties fulfilling the aim of the project.

4. Characterisation methods

The following section details sample preparation, specific parameters used when obtaining data sets, and post data collection analyses for specific characterisation techniques common across all chapters or which have been included for simplicity of presentation. Chapter specific techniques are discussed in subsequent sections.

4.1 Density measurements

The densities of sintered pellets were determined via a buoyancy method, utilising Archimedes principle, using an analytical laboratory balance (Mettler Toledo). The temperature of the water was read from a thermometer and input into the measurement routine to calculate the density of the water prior to the pellets being weighed. The pellets were weighed in air, and then in a sample basket fully immersed in water. The density of each individual sample, ρ_{solid} , can be calculated according to the following formula:

$$\rho_{solid} = \rho_{liquid} \left(\frac{m_{air}}{m_{air} - m_{immersed}} \right) \quad (22)$$

where ρ_{liquid} is the density of water, m_{air} is the mass of the pellet in air, and $m_{immersed}$ is the mass of the pellet immersed in water. Several determinate errors can arise due insufficient wetting of measured specimens, i.e. trapped air bubbles along surface porosity, and fluctuations in water temperature. These systematic errors can be minimised by satisfactory measurement practice. To account for indeterminate errors, all density values obtained across 3 individual samples sintered under the exact same conditions are reported.

4.2 X-ray diffraction

4.2.1 D2 PHASER

Phase identification and qualitative structural analysis was achieved using both ceramic and powder X-ray diffraction. A D2 PHASER X-ray diffractometer (Bruker) operated in Bragg-Brentano geometry with a Cu K_{α} radiation source ($\lambda = 1.5408 \text{ \AA}$), fitted with 2.5° Soller slits, a 1 mm divergence slit, and 0.5 mm and 2.5 mm Ni filters to remove Cu K_{β} radiation, was used to obtain data for ceramic and powder phase analysis. Selected sintered disks were mounted using Apiezon putty in a polymer specimen holder. The samples were carefully pressed using a glass slide to ensure the specimen height

was level with the specimen holder to avoid significant height displacement errors. Free powder samples were placed in a Si zero background holder, and carefully pressed using a glass slide to ensure the specimen height was level with the specimen holder. Ceramic and powder samples were scanned between the 2θ range of either $10\text{-}60^\circ$ or $20\text{-}80^\circ$ depending on the predicted crystal structure, with the sample rotation set at 15 rpm, using a step size of 0.02° and a $0.4\text{ sec}/^\circ$ scan rate. Standard X-ray tube working conditions were 30 kV and 10 mA.

4.2.2 D2 PHASER data analysis

Obtained ceramic and powder X-ray diffraction patterns were analysed using the International Centre for Diffraction Data (ICDD) PDF-4+ phase identification and quantification software with integrated Sleve+ search-indexing program. An initial database filter based on known sample elements was applied. Accepted database reference entries were selected according to goodness of match and visual inspection of experimental peaks with matched data.

4.2.3 Lotgering factor

The most common characterisation method for texture achieved via TGG is through reporting of a Lotgering factor (f)¹⁹⁰. f is calculated from the X-ray diffraction pattern intensities of a textured specimen and randomly oriented polycrystalline reference according to the following equations:

$$P = \frac{\sum I_{(001)}}{\sum I_{(hkl)}} \quad (23)$$

$$P_0 = \frac{\sum I_0(001)}{\sum I_0(hkl)} \quad (24)$$

$$f_{(001)} = \frac{P - P_0}{1 - P_0} \quad (25)$$

where P is the sum of the maximum peak intensities (counts) of the textured peaks ($\sum I_{(001)}$) divided by the sum of the intensities of all the peaks ($\sum I_{(hkl)}$) present in the X-ray diffraction pattern of the textured sample ((23), and P_0 the same but for the reference sample ((24). Comparing the different absolute intensity values in (25) gives a Lotgering value between 0 and 1. $f = 1$ indicates the sample is fully textured in a specific crystallographic orientation, i.e. (001) in the case of the equations shown, whereas $f = 0$ signifies a randomly oriented sample. Although minimal information about the alignment of

textured grains is obtained from the Lotgering technique, it is a time efficient characterisation method to report semi-quantitative texture formation¹⁹⁰. Integrating textured peak intensities using XRD rocking curve analysis is a more inclusive method to give a full description of textured volume fraction and texture orientation^{17,191}. The use of absolute peak intensity values, allows for both indeterminate and determinate errors to be reflected in the final Lotgering factor, arising from sample preparation and the resolution of the X-ray diffractometer, however calculation of the Lotgering factor still holds merit as a semi-quantitative metric for texture characterisation.

4.2.4 STOE STADI P (CuPSD)

Lattice parameters and structural characterisation was achieved using powder X-ray diffraction. Selected pellets were crushed in a pellet crusher and ground using a pestle and mortar in preparation for powder X-ray diffraction. STOE STADI P (CuPSD) X-ray diffractometer (STOE & Cie. GmbH) operated in transmission geometry with a monochromated Cu K α radiation source ($\lambda = 1.5408 \text{ \AA}$), fitted with fixed 6 mm divergence and detector slits, was used to obtain data for structural analysis. Selected powders were mixed with a small amount of Si standard reference material (SRM 640d, National Institute of Standards & Technology (NIST)) in a pestle and mortar. The mixed powder was adhered to an acetate disk using PVA glue, left to dry, and screw tightened in a metal specimen holder. Powder samples were scanned between the 2θ range of 20-80 $^\circ$, using a step size of 0.02 $^\circ$. Standard X-ray tube working conditions were 40 kV and 40 mA.

4.2.5 STOE STADI P (CuPSD) data analysis

Obtained powder diffraction data was analysed using WinX^{POW} (STOE & Cie GmbH) software package. Peak calibration was performed to obtain correction terms for the raw 2θ data scale utilising the known peak positions of the included Si standard reference material prior to determining lattice parameters. Lattice parameters were calculated using DICVOL04 indexing routine¹⁹², and further refined using the refinement tool in the WinX^{POW} software suite. It is important to highlight the error propagation of systematic errors, originating from the manual assignment of peak position within the WinX^{POW} software, to the final computed lattice parameters. This is especially the case when trying to deconvolute diffraction peaks of multiple phases, seen in near MPB compositions. Lattice parameter errors are expected to increase when prior peak deconvolution is required, therefore reported values should be viewed as indicative of a trend, and not individually exact.

4.3 Scanning electron microscopy

Microstructural characterisation of prepared samples (sections 4.3.1 and 4.3.2) was performed using both an Inspect F and Inspect F50 scanning electron microscope (SEM, FEI Company). Standard

working conditions were using a spot size of 3, with electron beam energy set a 10 keV. Both secondary electron (SE) and backscattered electron (BSE) images were taken at certain magnifications to obtain suitable images for both topographical and elemental analysis.

Average grain sizes for inspected samples were obtained using the mean liner intercept method based on ASTM standard E112-13¹⁹³. 10 lines, each 15 cm long, were randomly drawn on BSE images of revealed ceramic microstructures. The total grain boundary intersection count from all lines, computed by assigning a value of 1 for grain boundary intersections and 1.5 for triple point intersections, were used in the following relation:

$$G_{\text{avg}} = 1.5 \times \frac{\text{Total length of lines } (\mu\text{m})}{\text{Total grain boundary count}} \quad (26)$$

where G_{avg} is the averaged grain size of the sample, and the Mendelson correction factor of 1.5. Microstructural images revealing a sufficient number of grain boundaries (> 200) were analysed to ensure statistical accuracy.

Energy dispersive X-ray spectroscopy (EDS) was accomplished using Aztec 2.1 (Oxford Instruments NanoAnalysis) software package. Point X-ray spectra were obtained using the Point & ID application utilising imported BSE images, with pre-defined elements of known specimen compositions set for peak identification.

4.3.1 Ceramic sample preparation

Textured multilayers were purposely broken to reveal fracture surfaces. Selected pieces were adhered to 12.7 mm \varnothing , 45/90 $^\circ$ chamfer aluminium SEM pin stubs using double sided adhesive carbon dots, and subsequently Au sputter coated in preparation for SEM analysis.

Ceramic pellets were mounted in epoxy resin to analyse sample grain sizes. Mounted samples were initially ground using 800 grit SiC sandpaper using a manual EcoMet 30 polishing machine (Buehler) with platen rotation speed set at 200 rpm, using water lubricant. Further polishing was achieved using the same parameters with 1200, 2500, 4000 grit SiC sandpaper in ascending order, followed by a manual polish using a ChemoMet polishing cloth (Buehler) with 1 μm diamond paste and subsequent 0.05 μm colloidal Si suspension. The polished samples were removed from the epoxy resin mount by soaking in acetone. Thermal etching was necessary to reveal the grain boundaries on the surface of the polished pellets. Selected polished samples were placed on platinum foils sitting on a bed of PZ powder in an alumina crucible and individually enclosed using smaller upturned alumina crucibles to avoid PbO loss, then placed in a box furnace at 1100 $^\circ\text{C}$ for 1 min, with a heating/cooling rate of 10 $^\circ\text{C}/\text{min}$. Thermally

etched pellets were attached to 12.5 mm \varnothing aluminium SEM pin stubs using double sided adhesive carbon dots, and subsequently carbon sputter coated in preparation for SEM analysis.

4.3.2 Powder sample preparation

Small amounts of desired powders (< 0.1 g) were mixed with ethanol (absolute, $\geq 99.9\%$ purity, Sigma-Aldrich) in 25 mL glass vials and sonicated for 1 minute to ensure satisfactory dispersion. The solutions were pipetted on to a carbon dots adhered to 12.5 mm \varnothing aluminium SEM pin stubs and left to dry, in preparation for SEM analysis.

4.4 Dielectric measurements

The top and bottom surfaces of the sintered disks were lightly ground using 400 grit SiC sandpaper to remove any attached debris and to achieve a thickness < 1 mm in preparation for the application of Au electrodes. Au paste (no. C5729, Heraeus Materials Ltd) was applied by hand on both roughened top and bottom surfaces, and subsequently fired in a box furnace at 850 $^{\circ}\text{C}$ for 1 hour, with a heating/cooling rate of 10 $^{\circ}\text{C}/\text{min}$, to ensure adhesion.

The dielectric response of Au electroded samples were measured using a E4980A Precision LCR meter (Agilent Technologies Inc.) linked to a tube furnace. Capacitance and $\tan \delta$ measurements at set frequencies of 1 kHz, 10 kHz, 100 kHz, 250 kHz, and 1 MHz were taken in the temperature range from 25-500 $^{\circ}\text{C}$ on heating at a ramp rate of 1 $^{\circ}\text{C}/\text{min}$. Recorded capacitance values were converted into ϵ_r using following relation:

$$C = \epsilon_r \epsilon_0 \frac{A}{d} \quad (27)$$

where C is the capacitance, d is the disk thickness, A is the surface area of the top face, and ϵ_0 is the permittivity of free space.

4.5 Poling and quasi-static d_{33} measurements

Au electroded pellets with measured thicknesses of < 1 mm were poled in silicone oil (suitable for oil baths from -50 - 200 $^{\circ}\text{C}$, Sigma-Aldrich) at 180 $^{\circ}\text{C}$ under an applied electric field of 4 kV/mm for 15 minutes. The electric field was increased gradually in steps of 0.1 kV. The electric field was removed after 15 minutes, and the pellets removed at temperature. The poled samples were left to stand for 5 minutes to cool to room temperature before being measured. Quasi-static d_{33} measurements were obtained using a Berlincourt PM300 d_{33} PiezoMeter System (Piezotest Pte. Ltd), with an applied force

of 0.25 N and frequency of 110 Hz. The d_{33} coefficients were recorded after a dwell time of 5 minutes. Secondary d_{33} coefficients were recorded again 24 hours after poling under the same conditions, to provide an indication of indeterminate measurement errors.

4.5.1 Polarisation/strain hysteresis measurements

Large signal bipolar polarisation and displacement data was obtained at Hallam University, characterized using an aixACCT TF Analyzer 2000 system (aixACCT Systems GmbH). P-E/S-E hysteresis measurements were conducted at ambient temperature. An electric field was applied at a frequency of 2 Hz, with the electric field amplitude starting from 10 kV/cm up to a maximum of 50 kV/cm. The electric field strength was increased gradually using a 10 kV step size. S-E data was averaged over 4 cycles. The obtained P-E/S-E data was rendered and exported using the aixPlover Software (aixACCT Systems GmbH).

5. Suitable NBT-PT templates to texture PZT via TGG

As PT has a tetragonal perovskite structure (space group $P4mm$, no. 99) and is an end member of the PZT solid solution, it follows that PT in theory would make a suitable template material to favourably texture PZT via TGG. Previous literature on the synthesis of PT templates outlined in section 2.13, reports a two-step molten flux approach to grow anisometric perovskite phase templates from Aurivillius precursors via topochemical conversion, yielding a template material consisting of a solid solution of NBT-PT¹⁸⁶. Following this method PBT platelets were initially synthesised from precursor oxide powder using a molten flux method (section 5.1). The second stage topochemical conversion of Aurivillius phase PBT into perovskite phase NBT-PT is outlined in section 5.4. X-ray diffraction studies were performed to determine phase formation and phase purity of both stage one (Aurivillius PBT, section 5.2) and stage two (perovskite NBT-PT, section 5.5) products, with specific interest in validating the synthesis procedure. Microstructural characterisation of Aurivillius phase PBT is discussed in section 5.3. Further microstructural analysis using secondary electron imaging of the perovskite NBT-PT platelet product with respect to varying dwell times is explored in section 5.6. The suitability of the NBT-PT templates synthesised via this route, specifically for TGG of PZT is discussed with respect to ease of synthesis, product yield, and template quality.

5.1 Synthesis methodology for PBT precursor

PbO (99.9 % purity, Alfa Aesar), Bi₂O₃ (99.9 % purity, ACROS Organics), TiO₂ (rutile, ≥ 99.9 % purity, Sigma-Aldrich) were used as starting reagents, with KCl (99 % purity, Alfa Aesar) used as a molten flux. The starting reagents were individually weighed to give the desired 5 g batches according to the batch calculations shown in Appendix A, to give a target stoichiometric composition of PbBi₄Ti₄O₁₅ with an addition of equal weight (1:1) of KCl flux (5 g)¹⁸⁶. A 20:1 mass ratio of cylindrical yttria stabilized zirconia (YSZ) milling media (10 mm \varnothing x 10 mm) to reagent powder was placed in a 125 mL HDPE Nalgene bottle along with the weighed starting reagents and a 5:1 volume ratio of isopropanol (≥ 99.9 % purity, Merck) to reagent powder. The reagent powders were subsequently mixed via ball milling for 24 hours. The milling media was removed using a sieve and the mixed reagent powders were placed in a box furnace at 80 °C overnight to evaporate off the remaining solvent. The dried mixed powder was sieved using a 150 μ m mesh size sieve to ensure no significant powder agglomeration and then placed in a closed platinum crucible in preparation for calcination. The dried mixed powder was calcined in a box furnace at 1050 °C for 5 hours, with a heating/cooling rate of 10 °C/min. The synthesised PBT powder was washed with hot (70 °C) de-ionized water for 1 hour to dissolve the KCl flux and separated from the solution via vacuum filtration. The resulting PBT powder was placed in a box furnace set at 80 °C to dry overnight.

5.2 X-ray diffraction analysis of PBT precursor

X-ray diffraction pattern of the synthesised precursor PBT powder was obtained following the procedure outlined in section 4.2.1. Phase identification and peak indexing was done according to the procedure outlined in section 4.2.2. The powder X-ray diffraction pattern for the synthesised PBT is shown in Figure 19.

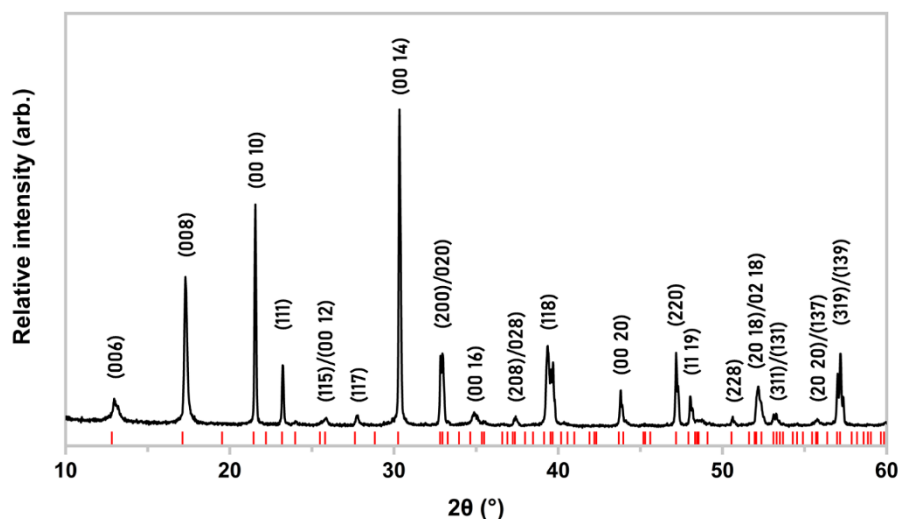


Figure 19 - X-ray diffraction pattern for synthesised stage one precursor Aurivillius phase PBT powder after 5 hour dwell time at 1050 °C, with major peaks indexed according to PDF 04-014-4545¹⁹⁴.

The synthesised PBT powder may be indexed according to a single orthorhombic Aurivillius structure (space group *Bb21m*, no. 36). The X-ray diffraction pattern (Figure 19) shows agreement with the matched entry in the International Centre for Diffraction Data (ICDD) database: PDF 04-014-4545 for $\text{PbBi}_4\text{Ti}_4\text{O}_{15}$ ¹⁹⁴. No impurity peaks relating to unreacted starting reagents, secondary phases, or remnant flux can be observed in the X-ray diffraction data. The single-phase Aurivillius phase present demonstrates that the 5 hour calcination time is suitable to ensure complete reaction of the starting mixed oxide powders. The lack of any peaks corresponding to the molten flux additive KCl, indicates that the washing procedure after calcination is sufficient in isolating the desired PBT product.

5.3 Microstructural characterisation of PBT precursor

SE images of the precursor Aurivillius phase PBT powder were obtained following the procedure detailed in section 4.3.2. SE images of the precursor Aurivillius phase PBT powder are shown in Figure 20.

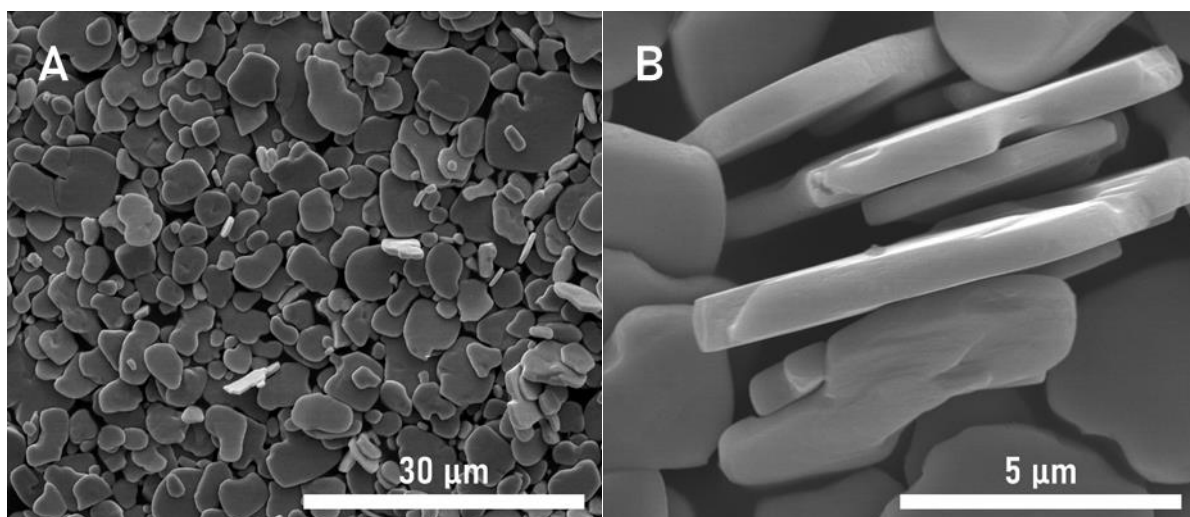


Figure 20 - a) SE image of PBT platelets synthesised after 5 hour dwell time at 1050 °C; b) SE image of edge facing PBT platelets.

The SE images of the precursor PBT platelets synthesised after 5 hour dwell time (Figure 20a) show large anisometric growth, consistent with conventionally flux grown Aurivillius phase materials arising from the large lattice parameter anisotropy ($a \ll c$) of the Aurivillius structure. A large platelet size distribution can be seen, with particle sizes ranging between 2 - 10 μm . Large PBT particles, with high aspect ratios, are desirable to successfully retain the platelet morphology during and after stage two topochemical conversion. The thickness edges of the platelets are comparably much smaller ($\sim 1 \mu\text{m}$) than the top planar surface (Figure 20b), giving rise to high aspect ratio platelets which can provide a suitable framework for topochemical conversion into the desired perovskite phase NBT-PT. Small PBT particles are therefore unwanted due to their low aspect ratios. Closer inspection of the PBT platelets show flat and clean surfaces free from any debris or artifacts potentially arising from the washing process. A small number of PBT particles show the appearance of discontinuous secondary growths on the platelets surface, suggesting possible sub-grain boundary formation, resulting from misaligned coarsening during flux growth. The larger PBT particles with clean faces are deemed suitable for the next step of topochemical conversion.

5.4 Synthesis methodology for NBT-PT templates

Dried precursor PBT powder, PbO (99.9 % purity, Alfa Aesar), and NaCl (≥ 99 % purity, Sigma-Aldrich) were weighed out to give a 5 g target mass according to a PBT:PbO:NaCl molar ratio of 1:4.5:21 (Appendix A) ¹⁸⁶. The weighed powders were placed in a FlackTek cup, and then dry mixed using a SpeedMixer (Hauschild GmbH & Co. KG) for 20 minutes at 800 rpm. The mixed powders were placed in a closed platinum crucible and heated in a box furnace at 1100 °C for 1-2 hours, with a heating/cooling rate of 10 °C/min. The synthesised NBT-PT powders were washed with hot (70 °C) de-ionized water for 1 hour to dissolve the NaCl flux, and subsequently separated out via vacuum filtration.

The remaining powders were washed with hot (70 °C) 30 % HNO₃ (≥ 99 % purity, Sigma-Aldrich) for 1 hour to dissolve any excess PbO and Bi₂O₃, vacuum filtered again to separate the acid, and placed in a box furnace set at 80 °C to dry overnight.

5.5 X-ray diffraction analysis of NBT-PT templates

X-ray diffraction patterns of the synthesised NBT-PT powders were obtained following the procedure outlined in section 4.2.1. Phase identification and peak indexing was done according to the procedure outlined in section 4.2.2. The powder X-ray diffraction patterns for the synthesised NBT-PT platelets after 1 and 2 hour hold times at temperature (dwell) are shown in Figure 21-Figure 22, respectively.

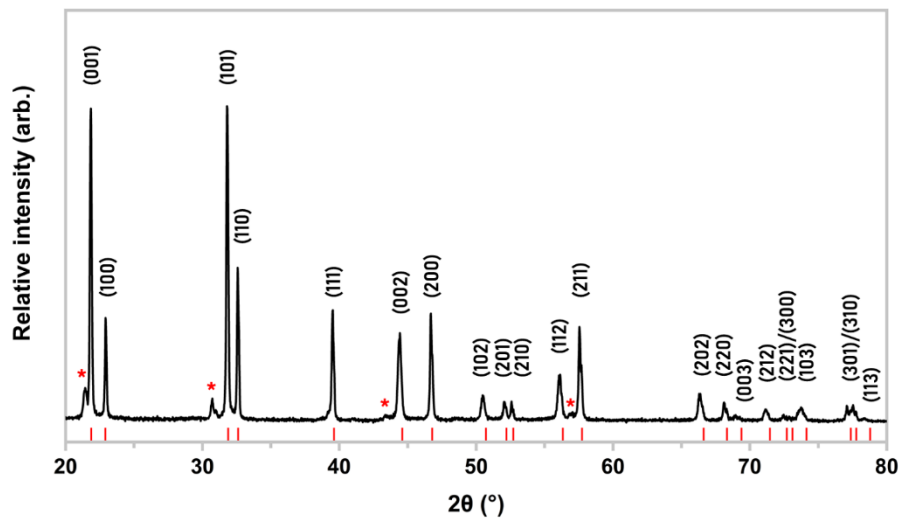


Figure 21 - X-ray diffraction pattern for synthesised stage two perovskite phase NBT-PT platelets after 1 hour dwell time at 1100 °C, indexed according to PDF 04-005-9744¹⁹⁵. Secondary phase peaks denoted with *.

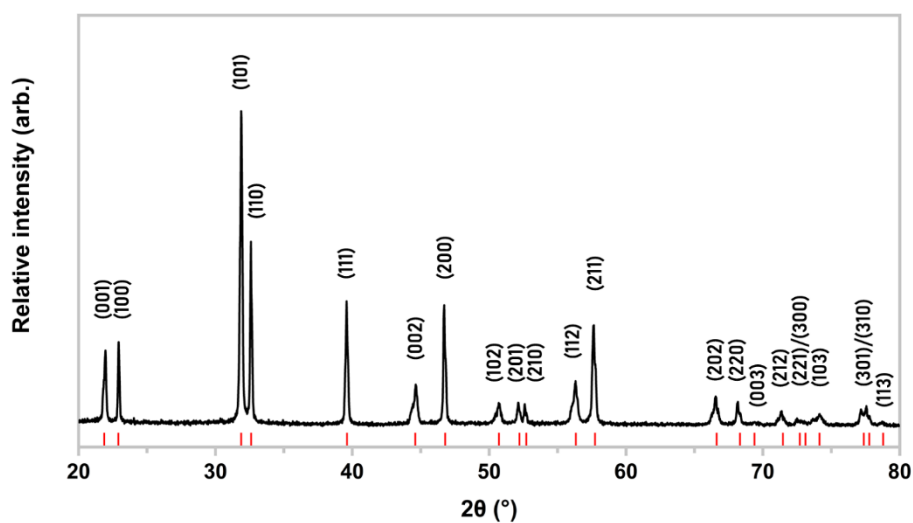


Figure 22 - X-ray diffraction pattern for synthesised stage two perovskite phase NBT-PT platelets after 2 hour dwell time at 1100 °C, indexed according to PDF 04-005-9744 ¹⁹⁵.

Both NBT-PT samples may be indexed according to a single tetragonal perovskite structure (space group $P4mm$, no. 99). The X-ray diffraction patterns (Figure 21-Figure 22) show good agreement with the matched ICDD entry PDF 04-005-9744 for $0.5\text{Na}_{0.5}\text{Bi}_{0.5}\text{TiO}_3\text{-}0.5\text{PT}$ ¹⁹⁵. Secondary phase peaks can be seen in the X-ray diffraction data for the 1 hour dwell sample (Figure 21), however due to their low intensity they are not able to be indexed satisfactorily using the ICDD software. The appearance of secondary phase peaks suggests that incomplete topochemical conversion has occurred after heating for 1 hour. The secondary phase cannot be explicitly identified as remnant PBT from comparison with the X-ray diffraction pattern obtained for the Aurivillius phase PBT precursor (section 5.2, Figure 19), however the shoulder peaks on both the (001) and (002) peaks of the identified perovskite phase suggests that the secondary phase has a similar structure, albeit with varying structural parameters.

No impurity peaks relating to unreacted starting reagents, secondary phases, or remnant flux can be seen in the X-ray diffraction data for the 2 hour dwell sample (Figure 22). Complete topochemical conversion of the Aurivillius phase PBT into the perovskite phase NBT-PT has occurred after heating for 2 hours. The indexed peak positions of the NBT-PT powders are those expected of a tetragonal perovskite structure, with doublets consistent with splitting of (001) peaks visible, however they do not match up with ICDD entries exclusively for either single-phase PT or NBT. No compositional data with respect to the ratio of PT and NBT members has been confirmed from the X-ray diffraction data obtained, although an approximate composition of $0.4\text{NBT-}0.6\text{PT}$ has been previously reported in literature ¹⁸⁶. This reported composition agrees with best reference composition match of $0.5\text{NBT-}0.5\text{PT}$ for the synthesised NBT-PT powder in this work. It is believed that only partial substitution of A-site Bi^{3+} with Pb^{2+} has occurred, with Na^+ from the NaCl flux also being incorporated into the structure,

necessary to maintain electroneutrality. It is not known if complete substitution of Bi^{3+} with Pb^{2+} is possible varying the quantity of starting PbO . The inclusion of the NBT component in the template material may have a detrimental effect in achieving textured PZT multilayers.

5.6 Microstructural characterisation of NBT-PT templates

SE and BSE images of the NBT-PT platelets synthesised via topochemical conversion of PBT with varying dwell times at 1 and 2 hours were obtained following the procedure defined in section 4.3.2. SE and BSE images for NBT-PT synthesised after 1 and 2 hours are shown in Figure 23-Figure 26 and Figure 28-Figure 31, respectively. Point EDS spectra for both NBT-PT samples are shown in Figure 27 and Figure 32.

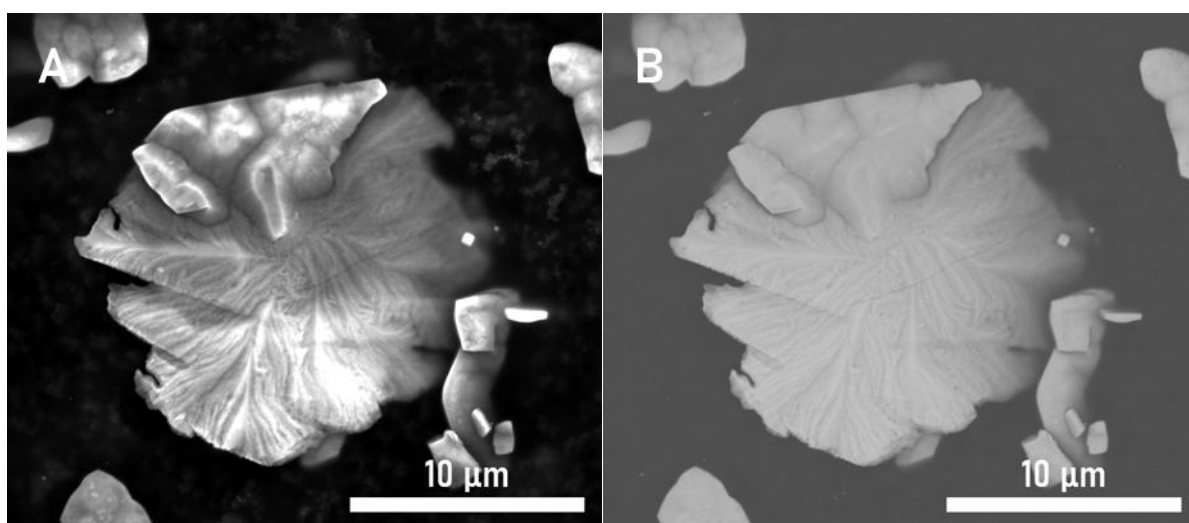


Figure 23 - a) SE image of partial NBT-PT platelet synthesised after 1 hour dwell time at 1100 °C, showing initial topotactic nucleation of NBT-PT on secondary phase host material; b) BSE image.

The NBT-PT particles synthesised after 1 hour dwell at 1050 °C show varying stages of topochemical conversion. From Figure 23-Figure 24, it is clear that incomplete topochemical conversion of the precursor Aurivillius phase PBT has occurred. This results in significant number of NBT-PT particles exhibiting substantial defects which render them unsuitable for use as templates for TGG. The most abundant defect is the formation of holes within particles, resulting in non-rectangular particles and ring particle shapes. Cracking along phase boundaries, indicative of partial exfoliation, is visible in dual phase particles (Figure 24). The premature exfoliation of either the perovskite or host phase during the reaction stage, i.e. prior to completion, results in a loss of epitaxy and a discontinuation of the host platelet morphology. The difference in surface topography between the host phase and topotactic NBT-PT is evident in Figure 23. Incomplete topochemical conversion, does not enable secondary stage densification of the formed perovskite phase, resulting in partial NBT-PT platelets with secondary phase inclusions. The resulting particle size distribution suggests that larger particles (~ 10 μm, Figure 23)

have undergone incomplete topochemical conversion, whilst much smaller particles ($< 5 \mu\text{m}$, Figure 25) exhibit complete topochemical conversion. Those smaller particles that have undergone complete topochemical conversion exhibit significant mosaicity, which can be explained by the imperfect alignment of several nucleation sites for the growing perovskite phase followed by subsequent ejection from the host crystal. Sufficient densification has occurred in these smaller particles, resulting in oriented polycrystalline platelets.

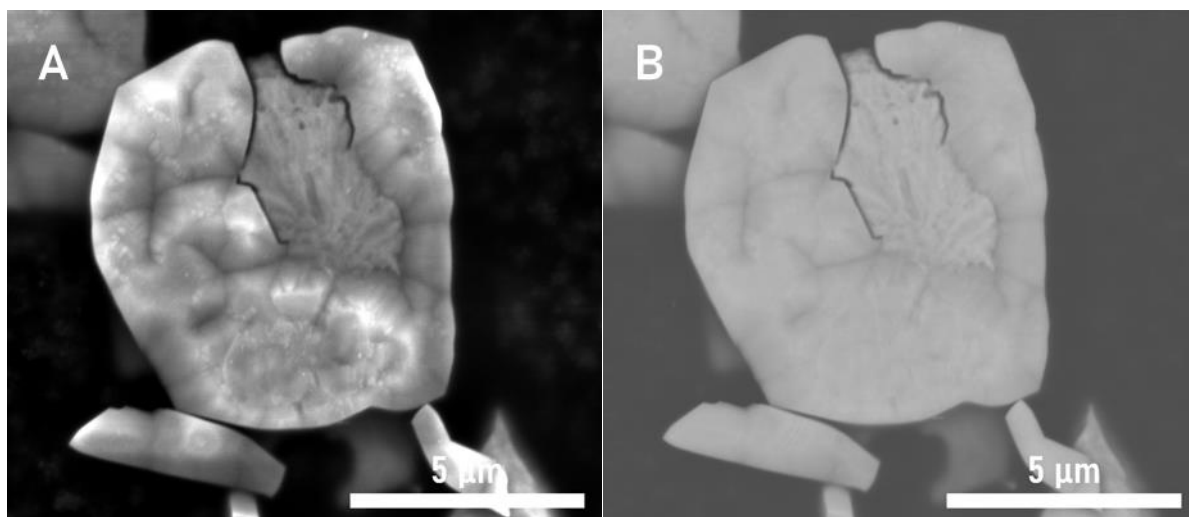


Figure 24 - a) SE image of partial NBT-PT platelet synthesised after 1 hour dwell time at $1100 \text{ }^\circ\text{C}$, showing near complete topochemical conversion into perovskite phase NBT-PT, with partial exfoliation of secondary phase; b) BSE image.

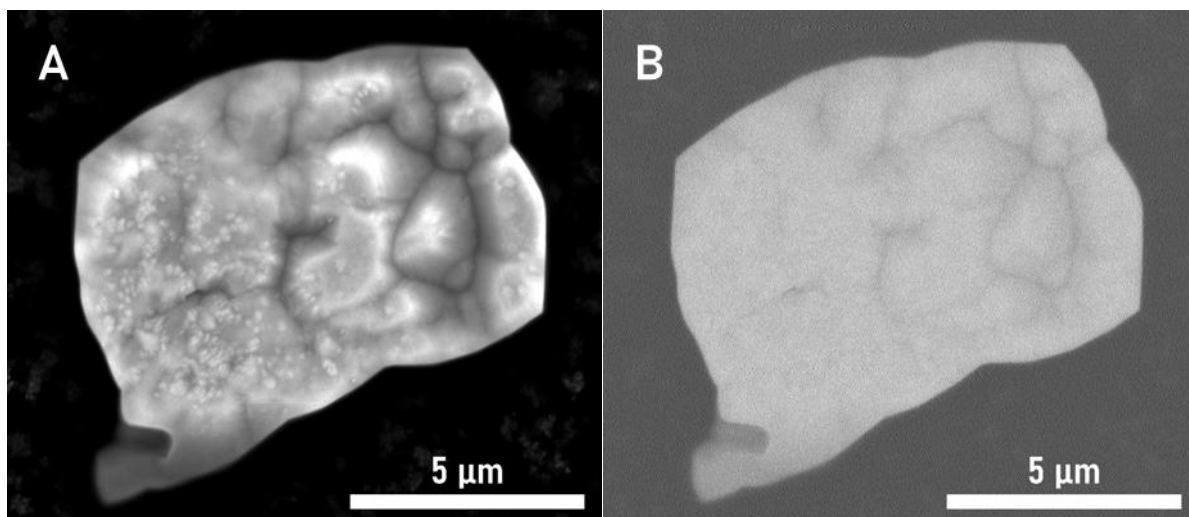


Figure 25 - a) SE image of NBT-PT platelet synthesised after 1 hour dwell time at $1100 \text{ }^\circ\text{C}$, showing complete topochemical conversion of Aurivillius phase PBT into perovskite phase NBT-PT; b) BSE image.

Inspection of the EDS spectra obtained from a suspected dual phase particle (Figure 26), believed to have originated from incomplete topochemical conversion of the Aurivillius phase PBT, shows a

marked variation in Bi concentrations between the two points and incorporation of Na within the structure of the NBT-PT phase (Figure 27). Whilst it is difficult to deconvolute the strong Pb and Bi $M\alpha$ peaks (~ 2.3 keV), the difference in Na $K\alpha_1$ (1.04 keV) intensities between the two points agrees with reports that Na^{2+} incorporation necessitates perovskite NBT-PT formation during topochemical conversion (Figure 27a)¹⁸⁶. The area around point 1 can therefore be identified as the desired perovskite phase NBT-PT, with an approximate composition deduced from the obtained At. % values of 0.4NBT-0.6PT. In contrast, point 2 has significant Bi and negligible Na concentrations (Figure 27b), consistent with reported intermediate bismuth layer structures (BLS) which are known to persist during the synthesis of PT via topochemical conversion¹⁸⁵.

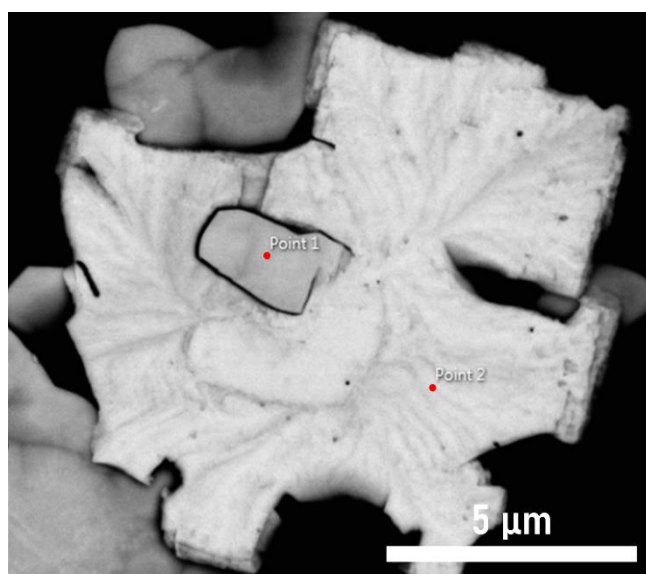


Figure 26 - BSE image of partial NBT-PT platelet synthesised after 1 hour dwell time at 1100 °C, used for EDS analysis.

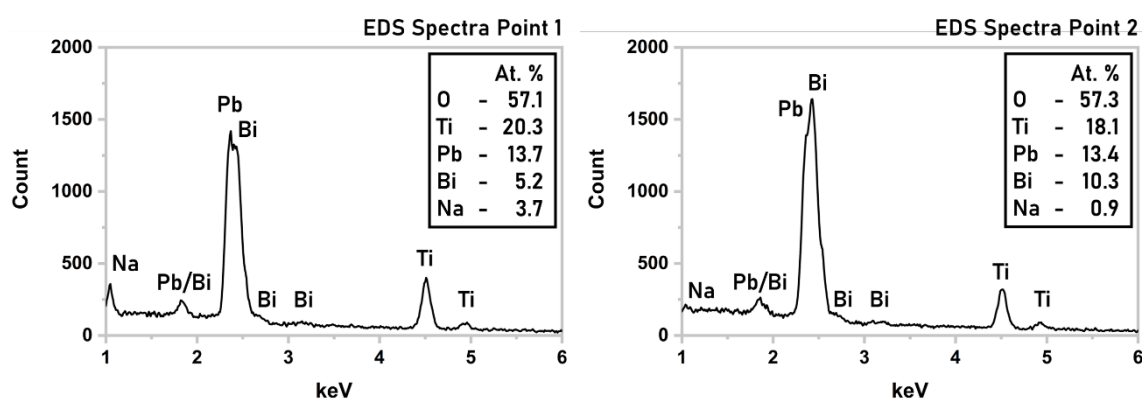


Figure 27 - a) Annotated EDS spectra for point 1 (from Figure 26); b) point 2.

The 1 hour dwell time is not sufficient in achieving complete formation of the NBT-PT reaction product. Synthesised polycrystalline NBT-PT platelets require further grain growth, necessary to achieve single crystals or highly oriented templates suitable for TGG. Use of these polycrystalline NBT-PT templates

may have a minor effect on texture formation in PZT due to the small lattice mismatch between both matrix and template perovskite phases, however it may affect the degree of orientation between crystallographically aligned grains, i.e. texture quality, originating from different misaligned areas of the same template. Due to the limited number of polycrystalline NBT-PT particles that show the desired morphology and apparent incomplete topochemical conversion seen in several particles, longer dwell times (> 1 hour) are necessary to synthesise suitable platelets.

The NBT-PT particles synthesised after 2 hour dwell at $1050\text{ }^{\circ}\text{C}$ show remarkably different particle morphologies than those synthesised after 1 hour (Figure 28a). Well defined rectangular particles are visible, often attached to smaller rectangular growths (Figure 28b). The longer dwell time of 2 hours may provide sufficient time for recrystallisation of the nucleated perovskite aggregates into dense rectangular platelets, i.e. complete topochemical conversion, and further grain growth to give near single crystal like particles. The lack of topographical features (mosaicity) seen in Figure 29, compared to Figure 25, suggests a lack of grain boundaries, and therefore misalignment within the dense particles, further indicating the possible formation of single crystal NBT-PT template particles. The well faceted particles seen, indicate that significant recovery (grain growth) has occurred after 2 hour dwell time.

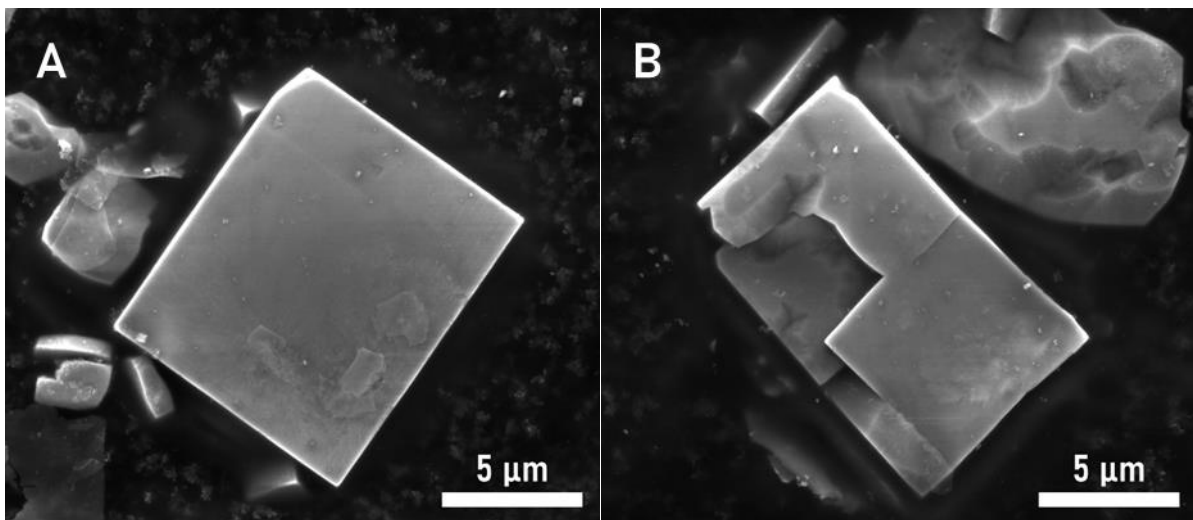


Figure 28 - a) SE image of singular clean NBT-PT platelet synthesised after 2 hour dwell time at $1100\text{ }^{\circ}\text{C}$; b) distorted NBT-PT platelet with misaligned growth.

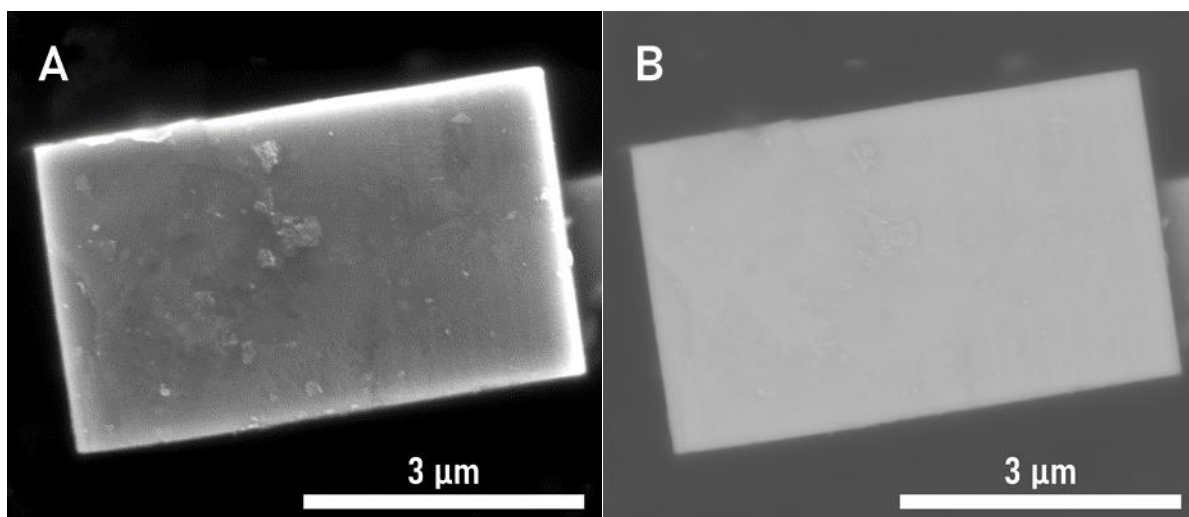


Figure 29 - a) SE image of top down surface of NBT-PT platelet synthesised after 2 hour dwell time at 1100 °C; b) BSE image.

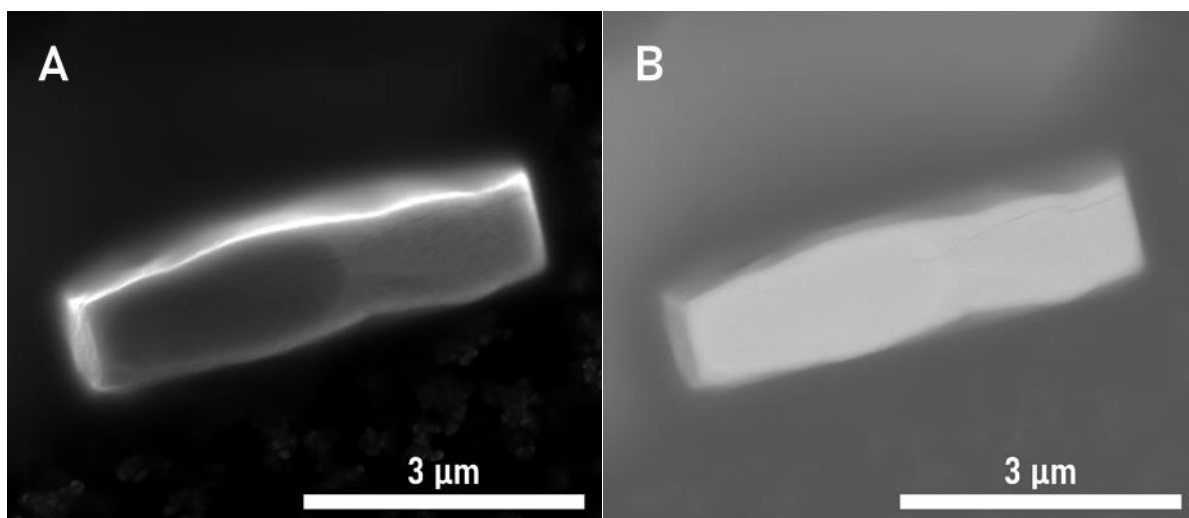


Figure 30 - a) SE image of edge surface of NBT-PT platelet synthesised after 2 hour dwell time at 1100 °C; b) BSE image.

There exists a combination of both large aggregates with irregular shape and well defined rectangular particles which have retained the host PBT platelet morphology. The particle sizes obtained after 2 hour dwell are slightly smaller ($< 5 \mu\text{m}$) than those seen after 1 hour dwell. The appearance of large aggregates with low aspect ratio indicates that further cubic equiaxed growth, expected from perovskite phase materials during molten flux growth due to their cubic structure at high temperatures, has occurred after topochemical conversion. This is accompanied by a visible increase in platelet thickness ($\sim 1 \mu\text{m}$, Figure 30). Significant growth of the template thickness is undesirable, reducing the particle aspect ratio, making alignment during tapecasting more difficult. The 2 hour dwell time is sufficient in promoting grain growth in polycrystalline particles and obtaining oriented dense platelets, however continued growth significantly reduces their aspect ratio. Separation of the required rectangular shaped

particles from the irregular shape particles is difficult due to their small size ($< 10 \mu\text{m}$). The EDS spectrum obtained for a visible single-phase particle (Figure 31) shows Na incorporation and reduced Bi concentration (Figure 32) in comparison with the EDS spectrum for dual phase particles that have undergone incomplete topochemical conversion (Figure 27a). The obtained At. % values give a composition based on the ratio of A site cations, (Na + Bi):Pb, of 0.54NBT-0.46PT with an increased NBT component compared to the reported idealised 0.4NBT-0.6PT composition¹⁸⁶. It is concluded that whilst an optimum dwell time between 1 and 2 hours, ensuring complete topochemical conversion and densification without further equiaxed coarsening, would give suitable perovskite phase NBT-PT templates, the difficulty in separating the templates from defective particles renders this process unsatisfactory in producing consistent and reproducible perovskite templates for the texturing of PZT in this work.

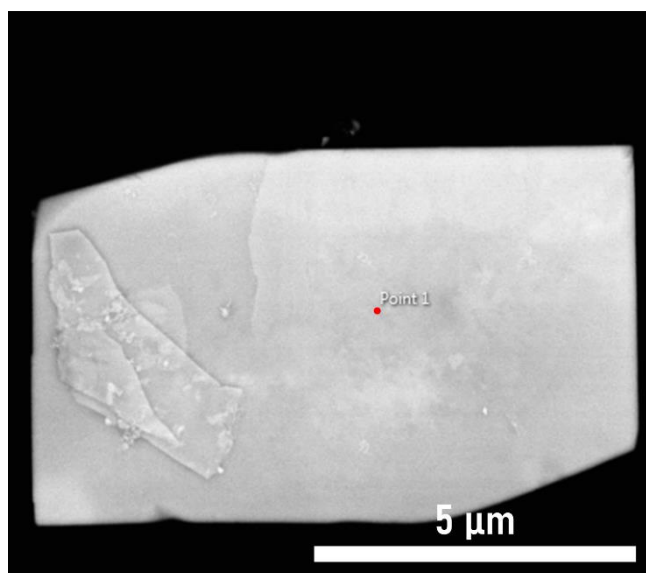


Figure 31 - BSE image of NBT-PT platelet synthesised after 2 hour dwell time at 1100 °C, used for EDS analysis.

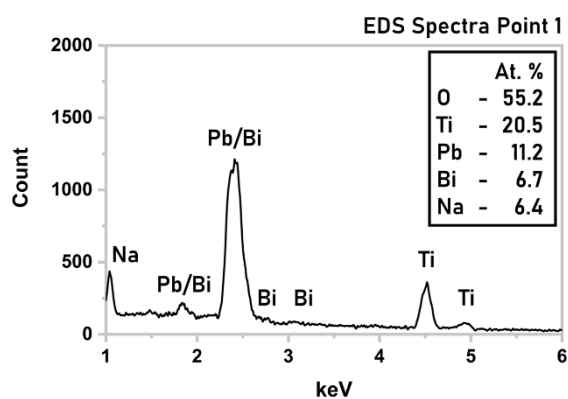


Figure 32 - Annotated EDS spectrum for point 1 (from Figure 31).

5.7 NBT-PT templates results summary

Perovskite phase NBT-PT templates have been synthesised via a two-step process consisting of molten flux growth of precursor Aurivillius phase PBT, followed by topochemical conversion into NBT-PT. The X-ray diffraction pattern for the NBT-PT templates synthesised after 1 hour dwell time show partial topochemical conversion has occurred, with unidentified secondary low intensity peaks visible. The X-ray diffraction pattern for the NBT-PT templates synthesised after 2 hour dwell time show complete topochemical conversion has occurred, with no secondary/impurity phases present. The varying dwell time employed in stage two from 1 to 2 hours, resulted in remarkably different particle morphologies. After 1 hour dwell time, the synthesised particles exhibit multiple defects associated with the premature exfoliation from the Aurivillius phase PBT host and subsequent loss of epitaxy. Dual phase particles are visible with contrasting surface topography, along with cracking along phase boundaries. The majority of fabricated particles exhibit irregular shapes without faceted edges, with larger particles ($> 10 \mu\text{m}$) showing secondary inclusions. EDS analysis of dual phase particles shows a marked difference in Na incorporation between the two regions, which is known to facilitate perovskite phase formation by charge balancing remnant Bi^{3+} . Smaller polycrystalline particles ($< 10 \mu\text{m}$) have undergone complete topochemical conversion into the desired perovskite NBT-PT phase.

From the resulting particle morphologies and apparent incomplete topochemical conversion, a 1 hour dwell time is not sufficient for this process. The 2 hour dwell time resulted in complete topochemical conversion into the desired phase. Small ($< 5 \mu\text{m}$) well faceted rectangular particles are seen, without any significant topographical features, along with large ($\sim 10 \mu\text{m}$) dense aggregates. Densification and secondary recrystallisation is evident, with single crystal-like particles formed. Further heating time is believed to cause equiaxed particle growth, increasing the through thickness of the platelets, lowering the high particle aspect ratio required for use in TGG. At. % values obtained from point EDS analysis give an approximate composition of 0.54NBT-0.46PT.

Overall, due to the complexity of the two stage process to synthesise high aspect ratio NBT-PT platelets and large variances in obtained particle morphologies/composition after both 1 and 2 hour dwell times, this procedure may not be suitable for large scale synthesis of templates necessary for TGG of PZT without complete optimisation of processing parameters beyond the scope of this work. The difficulty in controlling particle morphologies and reproducing consistent particle shapes necessitates the exploration of alternative perovskite template materials. BT has been reported in successful TGG of various relaxor-PT compositions^{157,159,161–168}. BT has a perovskite structure and similar lattice parameters (room temperature $a_t = 3.992 \text{ \AA}$, $c_t = 4.032 \text{ \AA}$)³² to PZT (room temperature $a_t = 4.037$, $c_t = 4.138$)¹¹³. This suggests that BT platelets may be a suitable alternative template material to PT, supported by literature on BT template synthesis [references], which is currently synthesised commercially.

6. Platelet shaped BT templates

Commercially sourced BT platelets (Entekno Materials) were identified as an alternative template material to the NBT-PT synthesised in section 5.4. BT has a tetragonal perovskite structure (space group $P4mm$, no. 99) at room temperature. BT templates have previously been reported in the successful TGG of several Pb-based perovskite piezoelectric materials, e.g. PMN-PT, PIN-PMN-PT etc. (section 2.12). This suggests that BT, in theory, should be a prime template material to achieved texturisation of PZT. A large batch (100 g) of BT platelet shape particles was purchased from Entekno Materials to explore their use in texturing PZT. X-ray diffraction studies were performed to confirm phase purity of the obtained platelet powder, believed to be synthesised industrially using a similar topochemical conversion method as that employed to fabricate NBT-PT templates in house (section 6.1). In the size separation procedure, formulated by researchers at Pennsylvania State University and adopted at the University of Sheffield, it is necessary to limit the size distribution of the BT platelet powder for optimal use during tapecasting, and is discussed in section 6.2. Microstructural characterisation of the BT powder is shown in section 6.3, to inspect the desired platelet shape and qualify the suitability of the purchased BT platelet powder for use in TGG.

6.1 X-ray diffraction analysis of BT templates

The X-ray diffraction pattern of the purchased BT platelet powder was obtained following the procedure outlined in section 4.2.1. Phase identification and peak indexing was carried out according to the procedure outlined in section 4.2.2. The powder X-ray diffraction pattern for the BT platelets is shown in Figure 33.

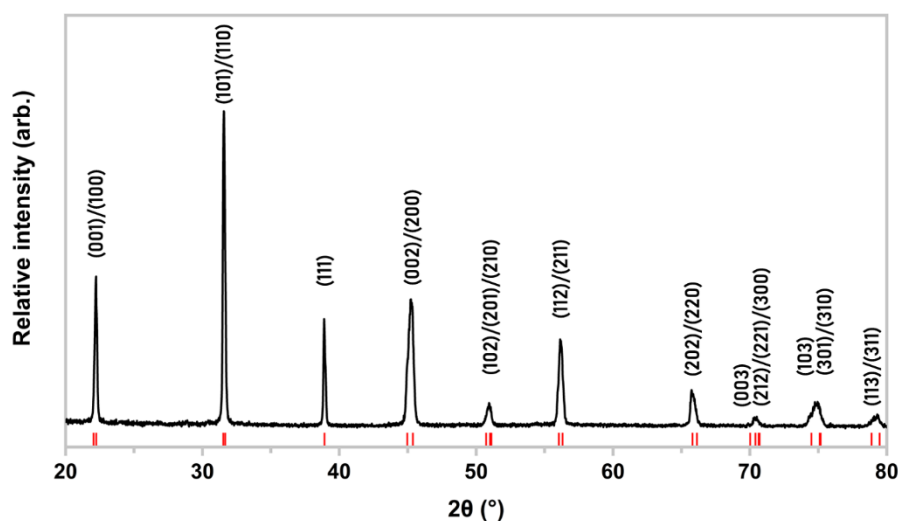


Figure 33 - X-ray diffraction pattern for BT platelets (Entekno Materials), indexed according to PDF 00-066-0829¹⁹⁶.

The BT platelets may be indexed according to a single tetragonal perovskite structure (space group $P4mm$, no. 99). The X-ray diffraction pattern (Figure 33) shows good agreement with the matched ICDD entry PDF 00-066-0829 for BT¹⁹⁶. No impurity peaks relating to the topochemical conversion process can be seen in the X-ray diffraction data.

6.2 Size separation methodology for BT templates

The BT platelet powder was separated into different size ranges via a 5-stage sedimentation process. 20 g of BT platelet powder was mixed with 500 mL of de-ionised water and 0.1 wt. % dispersant DS001 (Polymer Innovations Inc.) in a glass beaker. The mixture was agitated using a magnetic stir bar on a hot plate set at 80 °C for 20 minutes. The mixture was then quickly removed from the hot plate and placed in an ultrasonic bath for 1 minute. After sonication, the mixture was left to stand for 2 minutes before decanting into another glass beaker. The decanted product, consisting of < 30 μm platelets, was placed in a box furnace set at 80 °C to evaporate off the de-ionised water in preparation for further separation. The segregation process was repeated 3 times using the sediment product each time. The final sedimented product after 3 iterations was placed in a box furnace set at 80 °C to evaporate off the de-ionised water and stored as > 30 μm platelets (stage 1, $x < 2$ min). The decanted products were combined and mixed with 500 mL of de-ionised water and 0.1 wt. % DS001 in preparation for stage 2. Stage 2 followed the same process as stage 1 with the mixture allowed to settle for 8 minutes before decanting. The segregation process was repeated 3 times using the sediment product each time. The decanted products were combined and stored as low aspect ratio < 30 μm platelets (stage 2, $x > 8$ min).

The final sedimented product after 3 iterations, consisting of high aspect ratio $< 30 \mu\text{m}$ platelets, was mixed with 500 mL of de-ionised water and 0.1 wt. % DS001 in preparation for stage 3. Stage 3 followed the same process as stage 1 with the mixture allowed to settle for 3 minutes before decanting. The segregation process was repeated 3 times using the sediment product each time. The final sedimented product after 3 iterations was placed in a box furnace set at $80 \text{ }^\circ\text{C}$ to evaporate off the de-ionised water and stored as $> 20 \mu\text{m}$ platelets (stage 3, $2 \text{ min} < x < 3 \text{ min}$). The decanted products, consisting of $< 20 \mu\text{m}$ platelets, were combined and mixed with 500 mL of de-ionised water and 0.1 wt. % DS001 in preparation for stage 4. Stage 4 followed the same process as stage 1 with the mixture allowed to settle for 6 minutes before decanting. The segregation process was repeated 3 times using the sediment product each time. The decanted products were combined and stored as low aspect ratio $< 15 \mu\text{m}$ platelets (stage 4, $x > 6 \text{ min}$). The final sedimented product after 3 iterations, consisting of high aspect ratio $< 15 \mu\text{m}$ platelets, was stored as (stage 5, $3 \text{ min} < x < 6 \text{ min}$) in preparation for use during tapecasting.

6.3 Microstructural characterisation of BT templates

SE images of the purchased BT platelet powder after size segregation were obtained following the procedure outlined in section 4.3.2. The SE images of the purchased BT powder after size separation show an obtained controlled particle size distribution ($\sim 15 \mu\text{m}$) of BT platelets with high aspect ratio (Figure 34). The majority of BT particles have a suitable platelet morphology with visible mosaicity, suggesting that the particles consist of highly oriented polycrystals similar to the NBT-PT particles synthesised previously via topochemical conversion. It is believed that BT platelet powder is manufactured by a topochemical conversion route, and therefore the inclusion of highly oriented polycrystalline particles is to be expected. The large BT platelet size ($\sim 15 \mu\text{m}$) compared with the NBT-PT platelets synthesised in house ($< 5 \mu\text{m}$) is beneficial in avoiding dispersion issues during tapecasting slurry preparation, facilitating alignment during tapecasting due to having greater particle aspect ratios, and providing a lower energy surface for textured grain nucleation during heat treatment. No large irregular aggregates, a common artifact from the topochemical conversion processes, can be seen within the purchased powder sample. However, the inclusion of ring-shaped particles (Figure 35) indicates that separation of low aspect ratio particles is required prior to use in TGG. The majority of the defect particles, also seen in the fabricated NBT-PT product, should be satisfactorily removed during the long time sedimentation steps (stages 2 and 4, section 6.2).

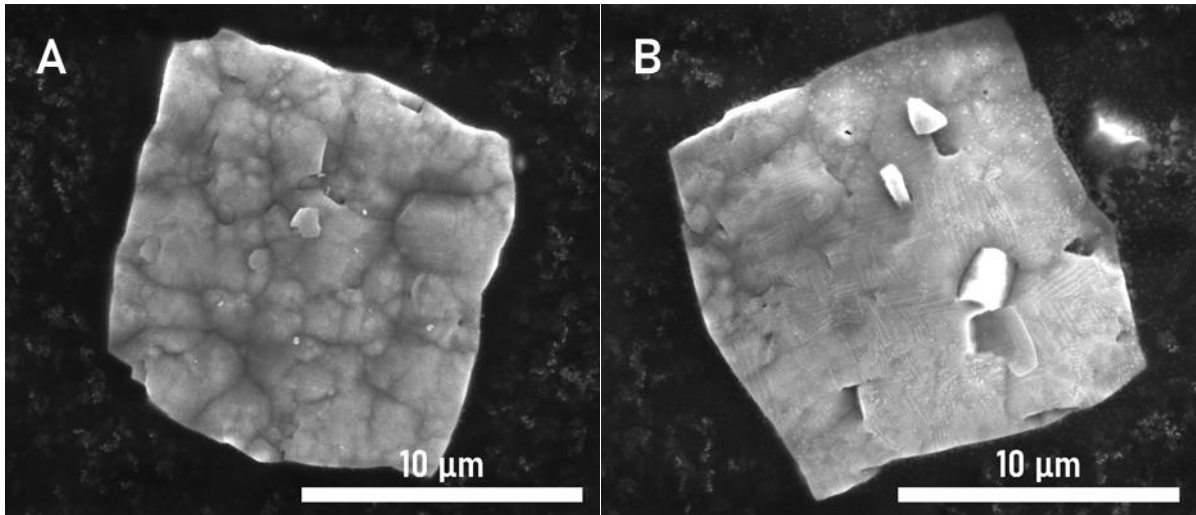


Figure 34 - a) SE image of size separated BT platelet with visible mosaicity; b) similar BT platelet.

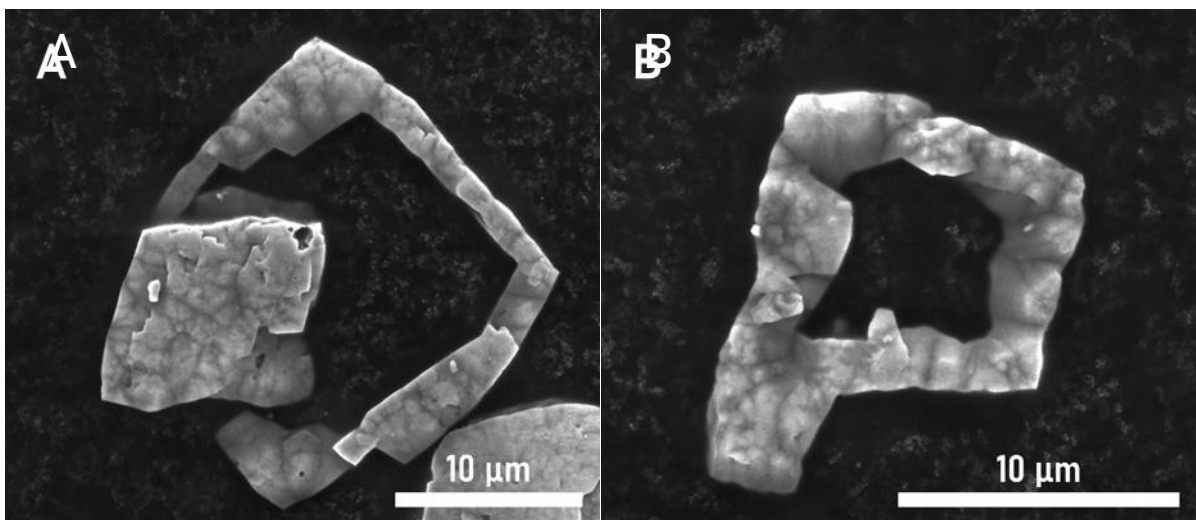


Figure 35 - a) SE image of ring-shaped BT platelet with partially ejected core; b) similar ring-shaped BT platelet.

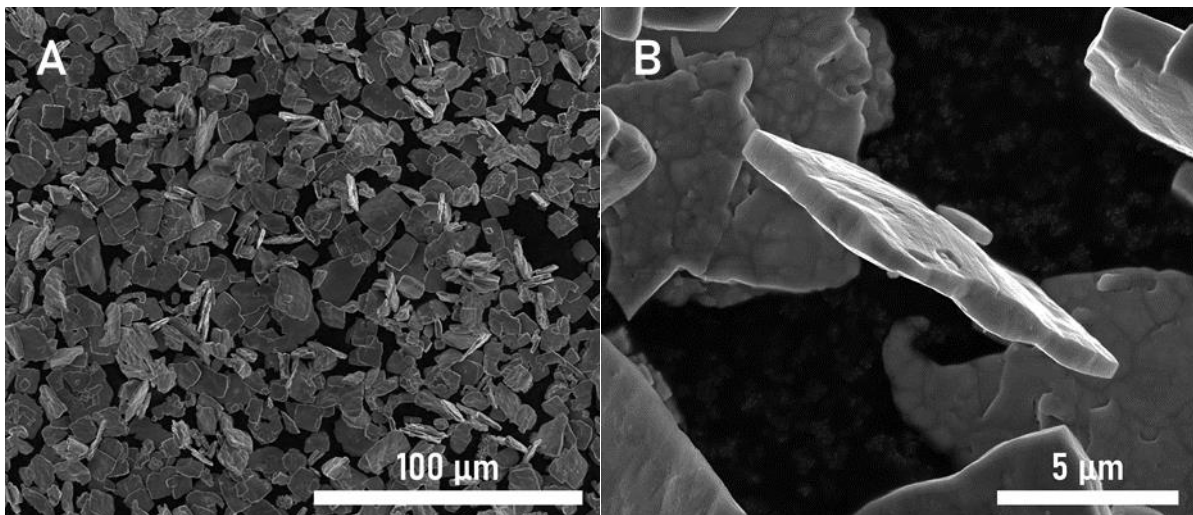


Figure 36 - a) SE image of size separated BT platelets; b) SE image of edge facing BT platelet.

6.4 BT templates results summary

Commercially sourced BT templates (Entekno Materials) provide a strong alternative to in house fabricated NBT-PT templates. The X-ray diffraction pattern of the BT platelet powder indicated complete phase purity. The size separation procedure to segregate specific size ranges of BT platelets is qualified via qualitative SEM analysis. Platelets with particle sizes $\sim 15 \mu\text{m}$ are obtained, exhibiting visible mosaicity. The distinct platelet shapes are free from known defects observed from the topochemical conversion process, along with suitable platelet sizes ($> 10 \mu\text{m}$) necessary for alignment during tapecasting, indicates that the size-controlled BT platelet powder is satisfactory for use in texturing PZT via TGG, overcoming the synthesis issues with fabricated NBT-PT platelets.

7. Textured PZT multilayers via TGG

BT templates are the prime candidate for use in TGG of PZT, due to their current commercial availability and compatible lattice parameters and crystal structure with PZT. Although other forms of templates were fabricated in house (section 5.4), procedures were complex, difficult to control, difficult to reproduce, and resulted in low volumes. Therefore, the selection of commercially available BT templates is grounded not only in the interest in achieving textured PZT multilayers, but also in the need for scale-up for industrial applications. Although many textured ceramics have been described in literature (section 2.12) satisfactory synthesis of textured PZT multilayers via conventional TGG has not yet been reported in literature (section 2.14).

PZT, with a starting Zr:Ti ratio of 52:48, + 5 vol. % BT templates (PZT52-5BT) with 5 wt. % PbO excess added based on previous literature on TGG of PZT¹⁸⁸, along with PZT-5A1 (Morgan Technical Ceramics) + 10 vol. % BT templates tapecast multilayers were synthesised according to the procedure outlined in section 7.1. PZT-5A1 is a commercially available ‘soft’ PZT variant, with a commercially sensitive composition, thereby influencing the volume template addition as a compensating factor. Untextured PZT samples were synthesised to provide a reference for texture characterisation (section 7.2). Bulk X-ray diffraction studies were performed to determine phase formation and establish texture evolution as a function of sintering time/temperature (section 7.3). Lotgering factors for texture characterisation were achieved by comparing multilayer X-ray diffraction patterns with those obtained for untextured PZT samples. Secondary electron imaging explored the microstructure and textured grain growth of multilayers with respect to sintering times and added excess PbO (section 7.4). This data is used to formulate a hypothesis on the formation of textured microstructures seen in both PZT52-5BT and PZT-5A1 samples with regard to critical processing parameters and microstructural evolution (section 7.4.1)

7.1 Synthesis methodology for [001]-textured PZT multilayers

PZT + 5 vol. % BT templates + 5 wt. % excess PbO multilayers with starting Zr:Ti ratio of 52:48 (PZT52-5BT), were synthesised using PbO (99.9 % purity, Alfa Aesar), ZrO₂ (TZ-0 Tosoh), and TiO₂ (≥ 99.5 % purity, Aeroxide P25, Evonik) powder reagents. Both ZrO₂ and TiO₂ starting reagents were dried at 900 °C for 8 hours prior to weighing. The starting reagents were individually weighed to make desired 50 g batches according to batch calculations shown in Appendix B. 120 g of 3 mm \varnothing , 5 mm \varnothing , and 10 mm \varnothing , spherical YSZ milling media was placed in a 1 L HDPE Nalgene bottle along with the weighed starting reagents. A 1:1 mass ratio of 190 proof ethanol to reagent powder (50 g) was added to act as a milling solvent. The reagent powders were subsequently mixed via vibratory milling for 72 hours. The milling media was removed using a sieve and the mixed reagent powders placed in a box furnace set at 80 °C overnight to evaporate the remaining solvent. Dried mixed powders were sieved

using a 100 μm mesh size sieve to prevent agglomeration and then placed in closed alumina crucibles for calcination. The dried mixed powders were calcined in a box furnace at 800 $^{\circ}\text{C}$ for 2 hours, with a heating/cooling rate of 10 $^{\circ}\text{C}/\text{min}$. 5 wt.% excess PbO (99.9 % Alfa Aesar), which acts as a transient liquid phase during sintering, was added to one calcined batch prior to all the batches being re-milled via vibratory milling for 72 hours, using the same media to powder and solvent to powder ratios previously stated. The milling media was removed using a sieve and the calcined powders placed in a box furnace at 80 $^{\circ}\text{C}$ overnight to evaporate the remaining solvent. The dried calcined powders were re-sieved using a 100 μm mesh size sieve to prevent agglomeration, in readiness for tapecast slurry formulation. PZT-5A1 + 10 vol. % BT templates multilayers were synthesised using commercial ‘soft’ PZT-5A1 powder (Morgan Technical Ceramics) provided by Leeds university, following the same powder processing methodology employed for the synthesis of undoped PZT from starting mixed oxide powders. No excess PbO was added to the PZT-5A1 powder. The importance of achieving a suitable particle size within the nano scale is deduced from previous unsatisfactory attempts at TGG using micro-sized PZT matrix powder, prepared via ball milling. The reduction from micron to nano scale tips the driving force in favour of initial textured grain epitaxy and sufficient grain growth compared to the matrix, to further promote exaggerated textured grain growth during the later stages of sintering.

The desired tapecast slurry formulation consisted of a water based acrylic binder WB4101 (Polymer Innovations Inc.), defoamer DF002 (Polymer Innovations Inc.), dispersant DS001 (Polymer Innovations Inc.), plasticizer PL008 (Polymer Innovations Inc.), and de-ionized water acting as a solvent, measured according to slurry calculations shown in Appendix B. either 5 or 10 vol. % of pre-segregated BT platelet powder (Entekno Materials), for a 30 g target matrix slurry composition, was weighed out and added to a measured solution consisting of de-ionised water, DF002, DS001, and PL008 in a FlackTek cup. The solution was sonicated for 1 minute to ensure satisfactory dispersion of the BT platelets. 30 g of matrix powder was then added to the solution, with a small cavity made in the centre off the added matrix powder subsequently filled with WB4101. The slurry was mixed using a DAC 150 SpeedMixer (FlackTek Inc.), initially at 800 rpm for 4 minutes, then at 1200 rpm for 4 minutes, repeating the latter stage three times, to give a total mix time of 20 minutes. The resulting slurry was cast on Mylar film with the casting blade height set at 200 μm and a casting rate of 2.8 $\text{mm}\cdot\text{s}^{-1}$, and then left to dry overnight. Good alignment of the BT templates, with the (001) faces parallel to the casting direction is critical to avoid large regions with apparent grain misalignment. If the casting height and speed deviate, the possibility of BT grains aligned randomly throughout the specimen, compounded by significant textured grain growth during sintering, will result in a poorly textured sample. Once dried, the tape was sectioned into 3 x 3 cm squares, carefully peeled from the Mylar backing, and stacked to form 20-layer green bodies. The green bodies were hot uniaxially pressed (75 $^{\circ}\text{C}$) at 10.8 MPa and subsequently hot isostatically laminated for 20 minutes. Both pressing regimens are important to further reduce interparticle spacings and aid in promoting as high a green density as

possible prior to sintering. This is beneficial during sintering, allowing for sufficient densities for TGG to be achieved prior to large uncontrolled grain growth. The laminated green bodies were rested on coarse alumina in an alumina crucible in preparation for binder burnout. The laminated green bodies were heated in a box furnace to 100 °C with an initial heating rate of 1 °C/min, then held 9 hours at 350 °C with a heating rate of 0.2 °C/min, followed by holding 5 hours at 450 °C with a final heating rate of 0.2 °C/min. After the binder burnout, the green bodies were placed in a vacuumed nitrile glove and cold isostatically pressed for 30 minutes. The pressed green bodies were embedded in matrix PZT or PZT-5A1 powder sitting on top of a bed of PZ powder in an alumina crucible and individually enclosed using smaller upturned alumina crucibles. The seals between the outer and smaller upturned crucibles, encapsulating the pressed green bodies, were covered further with PZ powder to regulate the PbO partial pressure during sintering and to avoid substantial PbO loss. The inclusion of PbO as a transient liquid phase is noted to be critical in enabling initial textured grain epitaxy prior to significant coarsening, as mass transport is enhanced within liquids phases by orders of magnitude, compared to solid state diffusion¹⁵⁵. No textured grain epitaxy was observed in samples without liquid phase additions. The final pressed green bodies were sintered for 2, 4, and 8 hours in a box furnace to at 1200 °C hours with a heating/cooling rate of 10 °C/min.

7.2 Synthesis methodology for PZT/PZT-5A1 ceramics

PZT ceramics, with Zr:Ti ratio of 52:48, were synthesised using PbO (99.9 % purity, Alfa Aesar), ZrO₂ (99 % purity, Sigma-Aldrich), TiO₂ (rutile, ≥ 99.9 % purity, Sigma-Aldrich). Both ZrO₂ and TiO₂ starting reagents were dried at 900 °C for 8 hours prior to weighing. PZT-5A1 ceramic powder (Morgan Technical Ceramics) did not require any prior calcination. The starting reagents were weighed to give a final stoichiometric composition. A 20:1 mass ratio of cylindrical yttria stabilized zirconia (YSZ) milling media (10 mm \varnothing x10 mm) to reagent powder was placed in individual 125 mL HDPE Nalgene bottles along with the weighed starting reagents and a 5:1 volume ratio of isopropanol (≥ 99.9 % purity, Merck) to reagent powder. The reagent powders were subsequently mixed via ball milling for 24 hours. The milling media was removed using a sieve and the mixed reagent powders transferred into a box furnace set at 80 °C overnight to evaporate off the remaining solvent. The dried mixed powders were sieved using a 150 μ m mesh size sieve to ensure no significant agglomeration and then placed in closed alumina crucibles in preparation for calcination. The dried mixed powders were calcined in a box furnace at 800 °C for 2 hours, with a heating/cooling rate of 10 °C/min.

The calcined PZT powders and PZT-5A1 powder were ball-milled individually for 24 hours using the same media to powder and solvent to powder ratios stated previously, with an additional 10 wt. % polyvinyl acetate (PVA) solution (5 wt. % PVA, 95 wt. % de-ionised water) to act as a binder. The milling media was removed using a sieve and the powders transferred into a box furnace set at 80 °C overnight to evaporate the remaining solvent. The dried powders were re-sieved using a 150 μ m mesh

to ensure no significant agglomeration. The separate prepared powders were loaded into a 10 mm \varnothing die and pressed at \sim 125 MPa for 10 seconds using a uniaxial press. The pressed green pellets were placed on platinum foils sitting on a bed of PZ powder in an alumina crucible and individually enclosed using smaller upturned alumina crucibles. The seals between the outer and smaller upturned crucibles encapsulating the pellets were covered further with PZ powder to regulate the PbO atmosphere formed during sintering and to avoid substantial PbO loss from the pellets. The pellets were heated in a box furnace to 550 $^{\circ}$ C for 3 hours, with a heating rate of 1 $^{\circ}$ C/min, to ensure complete binder burnout and then sintered at 1250 $^{\circ}$ C for 2 hours, with a heating/cooling rate of 10 $^{\circ}$ C/min.

7.3 X-ray diffraction analysis of [001]-textured PZT multilayers

The X-ray diffraction patterns for the reference PZT and PZT-5A1 ceramics, along with patterns for [001]-textured PZT52-5BT and PZT-5A1 multilayers, sintered for varying times, were obtained according to the procedure in section 4.2.1. The corresponding X-ray diffraction patterns for PZT and PZT-5A1 ceramics, [001]-textured PZT52-5BT and PZT-5A1 multilayers are shown in Figure 37- Figure 40, respectively.

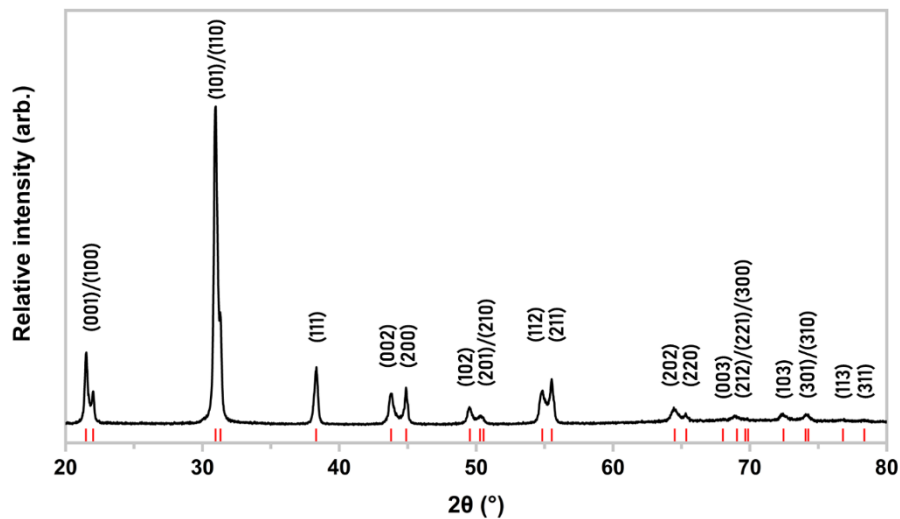


Figure 37 - X-ray diffraction pattern for reference PZT ceramic sample synthesised after 2 hour dwell time at 1250 $^{\circ}$ C, indexed according to PDF 01-070-4264¹⁹⁷.

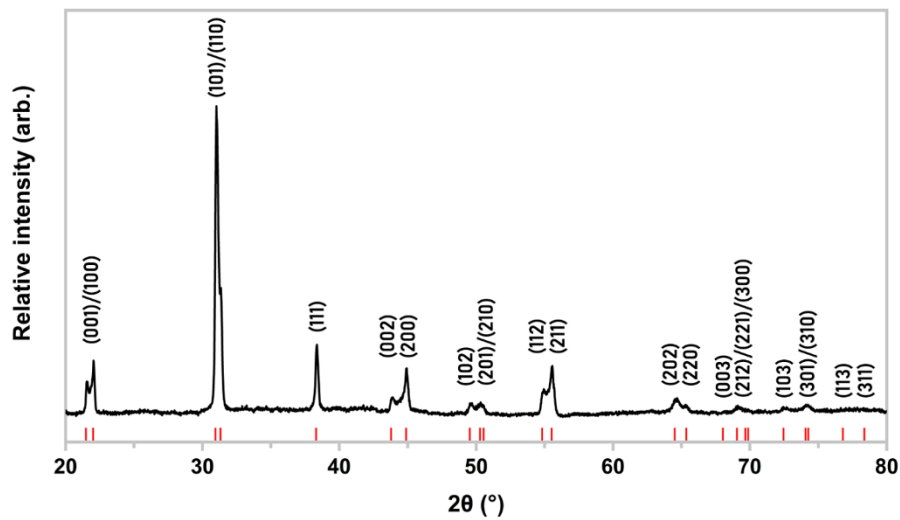


Figure 38 - X-ray diffraction pattern for reference PZT-5A1 ceramic sample synthesised after 2 hour dwell time at 1250 °C, indexed according to PDF 01-070-4264 ¹⁹⁷.

The poled randomly oriented reference PZT ceramic may be indexed according to a tetragonal perovskite structure (space group $P4mm$, no. 99). The X-ray diffraction pattern (Figure 37) shows good agreement with the matched ICDD entry PDF 01-070-4264 for $\text{PbZr}_{0.53}\text{Ti}_{0.47}\text{O}_3$ ¹⁹⁷. The peak profile of the $\{200\}$ suggests possible preferred domain orientation along the surface of the sample. This can result from domain switching caused by grinding and polishing of the samples, however such preferred orientation should not impact the $f_{(001)}$ values obtained when used as a reference against [001]-textured specimens. No impurity peaks relating to unreacted starting reagents or significant PbO loss can be seen in the X-ray diffraction data. Phase coexistence is known to occur in near MPB PZT compositions, therefore there may be a small rhombohedral phase fraction present. The reference PZT-5A1 ceramic may also be indexed according to the same tetragonal perovskite structure (space group $P4mm$, no. 99). The X-ray diffraction pattern (Figure 38) shows good agreement with the matched ICDD entry PDF 01-070-4264 for $\text{PbZr}_{0.53}\text{Ti}_{0.47}\text{O}_3$ ¹⁹⁷. Clear splitting of the $(00l)$ peaks is indicative of a c/a ratio greater than unity, indicating that the predominate phase in the PZT-5A1 composition has a tetragonal perovskite structure.

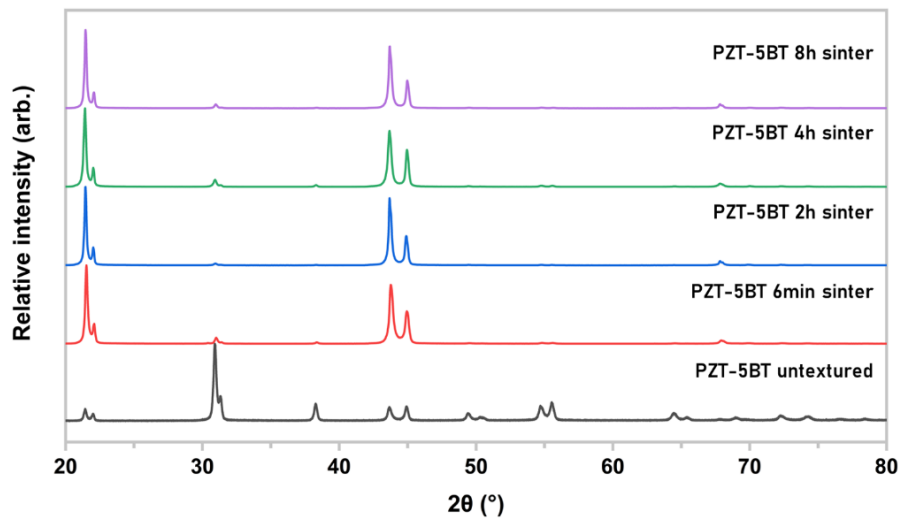


Figure 39 - X-ray diffraction patterns for [001]-textured PZT52-5BT multilayers with 5 wt. % PbO, sintered varying dwell times at 1200 °C, and randomly oriented reference tetragonal PZT52-5BT sample.

The intensities of the $(00l)$ peaks are clearly visible in the X-ray diffraction patterns for the PZT52-5BT + 5 wt. % PbO multilayers (Figure 39), with all the other (hkl) peak intensities being suppressed. The recognisable doublets of the $(001)_t/(100)_t$ and $(002)_t/(200)_t$ peaks around $\sim 22^\circ$ and $\sim 44^\circ$ respectively, indicate that the bulk structure can be indexed to a single tetragonal perovskite structure (space group $P4mm$, no. 99). No secondary or impurity phases (remnant PbO or BT templates) can be identified from the X-ray diffraction data. From Figure 39, all textured samples show a slight increase in tetragonality, with the splitting distances between the $(00l)_t$ and $(100)_t$ peaks larger than the reference MPB sample (Figure 37). There is also no apparent phase coexistence between tetragonal and rhombohedral structures, associated with near MPB compositions. This increase in tetragonality can only be explained by the inclusion of tetragonal BT templates. BT is known at room temperature to exhibit a tetragonal perovskite phase, similar to that of Ti-rich PZT compositions³². It can be assumed from both the increase in tetragonality and the lack of any secondary peaks, that up to 5 vol. % BT is thermally unstable within the PZT matrix after sintering at 1200 °C, and consequently forms a solid solution with the PZT matrix. This can be considered analogous to isovalent doping with Ba^{2+} replacing Pb^{2+} , although the additional Ti component from the BT source will change the overall Zr:Ti ratio. Using an initial PZT Zr/Ti ratio of 1.083 for the MPB composition, the addition of 5 vol. % BT gives a final Zr/Ti ratio of 0.972 for the [001]-textured PZT52-5BT multilayer, far in the tetragonal side of the MPB.

The suppression of all (hkl) peak intensities apart from $(00l)$ peaks in Figure 39 is a clear indication of [001]-texture. As the surface grains of the sample are all aligned in the [001] direction, the reflection of the incident X-ray beam will show only reflections related to the atoms present in the $(00l)$ planes. The

evolution of the X-ray diffraction data with respect to the randomly oriented sample confirms that TGG of [001]-textured PZT is possible using anisometric (001) BT templates. Such an increase in texture of the PZT specimen after just 6 mins is unexpected. Multilayers with the same composition, without added excess PbO acting as a transient liquid phase, failed to exhibit any texture in the [001] direction after sintering for up to 8 hours. This suggests that the addition of excess PbO is critical in enabling texture formation in the PZT52-5BT system. It is known that diffusion rates during liquid-phase sintering are enhanced by orders of magnitude with respect to solid-state sintering¹⁵⁵. It can be seen that significant textured grain heteroepitaxy and subsequent textured grain growth, enabled and aided by the presence of a liquid phase, occurs rapidly due to the suppression of certain X-ray diffraction peaks after just 6 mins sintering at 1200 °C. This reflected in an initial, $f_{(001)} = 0.91$, achieved. Longer sintering times appear to have a minimal increase in texture evolution, with only a small improvement, $f_{(001)} = 0.94$, after sintering for up to 8 hours. This suggests that significant textured grain growth has occurred rapidly during the early stages of densification, with the driving force for further growth quickly decreasing with increasing time. As both grain growth and densification are competing processes, this is likely to have a detrimental effect on final multilayer densities.

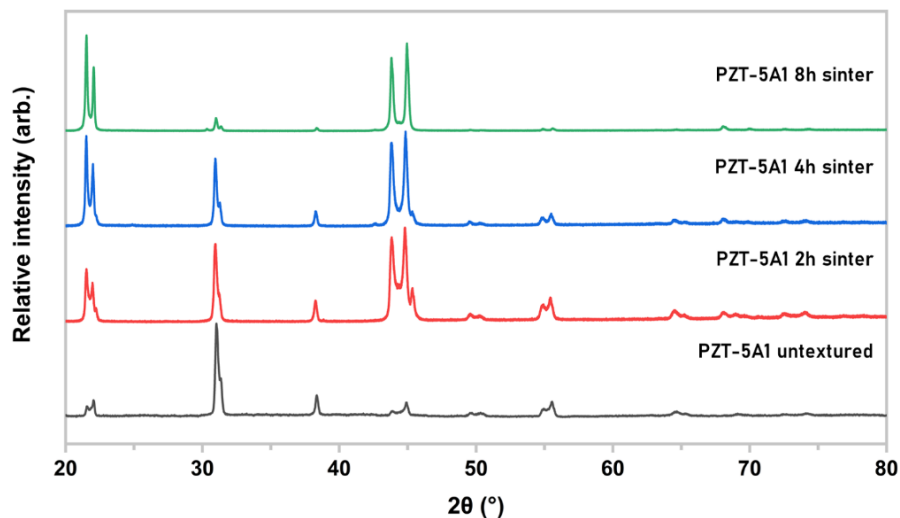


Figure 40 - X-ray diffraction patterns for [001]-textured PZT-5A1 multilayers with 10 vol. % BT templates, sintered varying dwell times at 1200 °C, and randomly oriented reference PZT-5A1 sample.

The X-ray diffraction patterns for the PZT-5A1 multilayers (Figure 40) show a steady increase in (00 l) peak intensities with increasing sintering times. The appearance of (001)_t/(100)_t and (002)_t/(200)_t doublet peaks indicates that the bulk crystal structure is again tetragonal perovskite (space group P4mm, no. 99). The lack of any excess PbO added prior to sintering indicates that texture evolution in the PZT-5A1 multilayers is dependent on liquid phase formers/sintering aids present in the starting material. The exact composition of these additives is not known due to commercial confidence.

The appearance of shoulders on the $(001)_r/(100)_t$ doublet $\sim 22^\circ$ and $(002)_r/(200)_t$ doublet $\sim 44^\circ$ are believed to be due to the inclusion of a Ba- and Ti-rich phase in the PZT-5A1 matrix, as BT has a tetragonal structure at room temperature. Efforts to directly match the shoulder peaks with ICDD entries for tetragonal BT failed, suggesting that the peaks relate to a tetragonal perovskite phase with a mixture of Ba^{2+} and Pb^{2+} on the A-site, and more Ti^{4+} than Zr^{4+} on the B-site to satisfy the increase in tetragonality. The apparent lack of any tetragonal shoulder peaks in the PZT52-5BT X-ray diffraction data (Figure 39) points to complete dissolution of the BT templates into the PZT solid solution and homogenisation of Ba throughout the matrix. As the sintering time is increased the intensities of the shoulder peaks in the PZT-5A1 diffraction data decreases, disappearing completely after 8 hours. A maximum $f_{(001)} = 0.84$ was obtained for the PZT-5A1 multilayer sintered for 8 hours. The evolution of the X-ray diffraction data with respect to the randomly oriented sample confirms that TGG of commercially available [001]-textured PZT-5A1 is possible using anisometric (001) BT templates.

Both PZT52-5BT and PZT-5A1 multilayers exhibit texture without any major variation in the established TGG process, including the addition of significant dopants/elements known to affect microstructural properties of PZT, albeit with the addition of excess PbO to form a transient liquid phase. Therefore, the apparent difficulties in texturing PZT can be overcome with specific regard to the fundamental parameters that govern the efficacy of the TGG process as discussed in section 7.4.1.

7.4 Microstructural characterisation of [001]-textured PZT multilayers

SE images of the fracture surfaces of textured PZT52-5BT and PZT-5A1 multilayers were obtained following the procedure defined in section 4.3.1. SE images for template alignment within the matrix pre-sintering are shown in Figure 41, with both textured PZT52-5BT and PZT-5A1 multilayers microstructures seen in Figure 42-Figure 43, respectively.

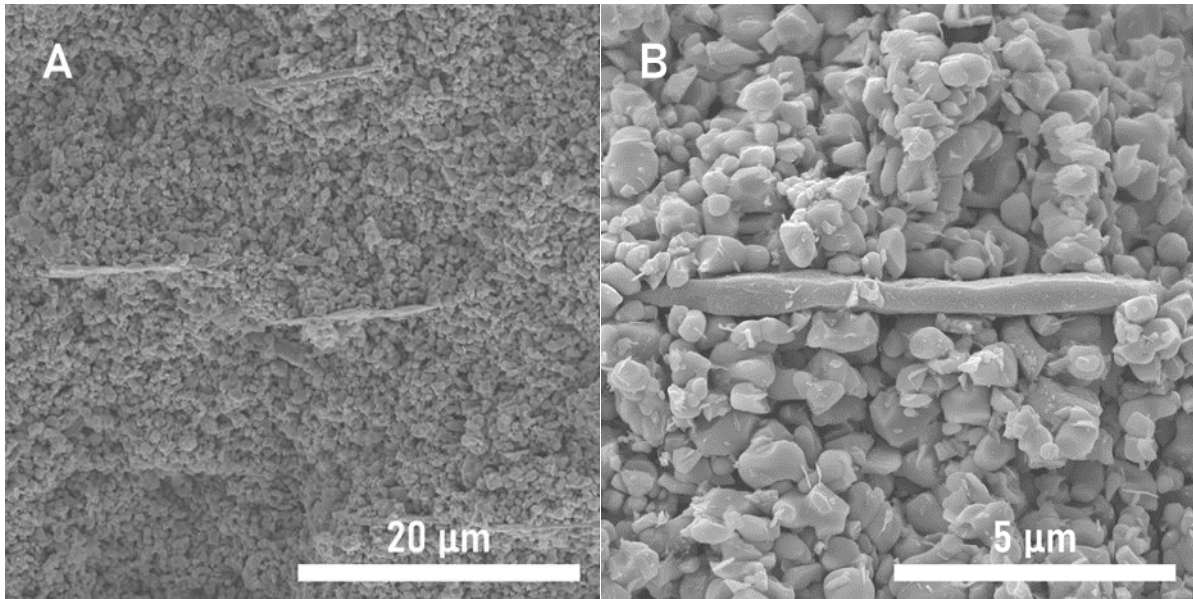


Figure 41 - a) SE image of pre-sintered pressed multilayer showing aligned BT templates within fine PZT matrix; b) individual BT template.

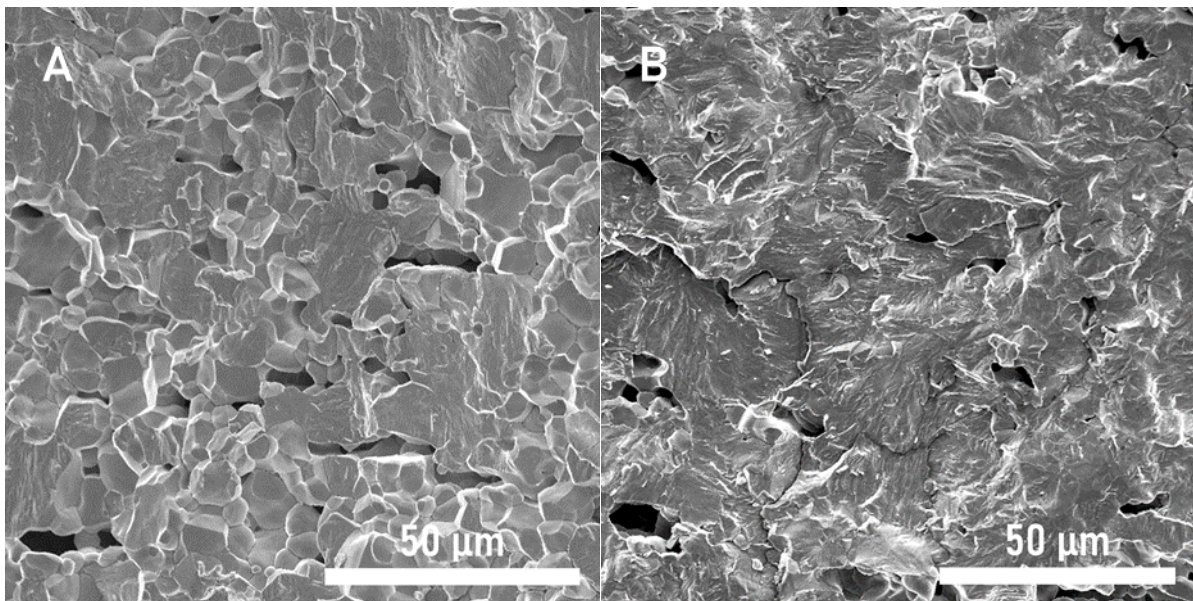


Figure 42 - a) SE image of PZT52-5BT microstructure after sintering for 2 hours at 1200 °C; b) 8 hours.

The SE image of the PZT52-5BT multilayer microstructure after 2 hours (Figure 42a) shows an inhomogeneous microstructure with significant elongated pores. The pore morphology closely resembles the shape of template grains, however constrained sintering may underline the appearance of such porosity. No template grains can be identified within the bulk, confirming that BT is not thermally stable within the PZT matrix at sintering temperature (1200 °C). Fine equiaxed grains can be seen ($< 5 \mu\text{m}$) along with much larger coarsened grains ($> 20 \mu\text{m}$), believed to originate from heteroepitaxial grains deposited on the (001) crystal faces of the template grains prior to their dissolution. There is no singular continuous textured layer surrounding the remnant pores typically reported during TGG,

suggesting that initial dissolution-precipitation has occurred accompanied by rapid grain textured grain coarsening. The microstructural evolution can best be represented by the schematic shown in section 2.12, Figure 16.

The disappearance of equiaxed grains with increasing sintering time seen in Figure 42b, along with a slight increase in texture fraction from X-ray diffraction data, suggests they are initial coarsened matrix grains, that are subsequently consumed by the larger textured grains during exaggerated grain growth. The fracture mechanisms can be described as intergranular for the small equiaxed grains and intragranular for larger textured grains from the rough fracture surface. Complete textured grain coarsening results in a homogeneous microstructure after sintering for 8 hours. Large exaggerated grains ($> 50 \mu\text{m}$) can be observed, along with a slight closure of porosity, with the remnant pores no longer distinctly platelet shaped.

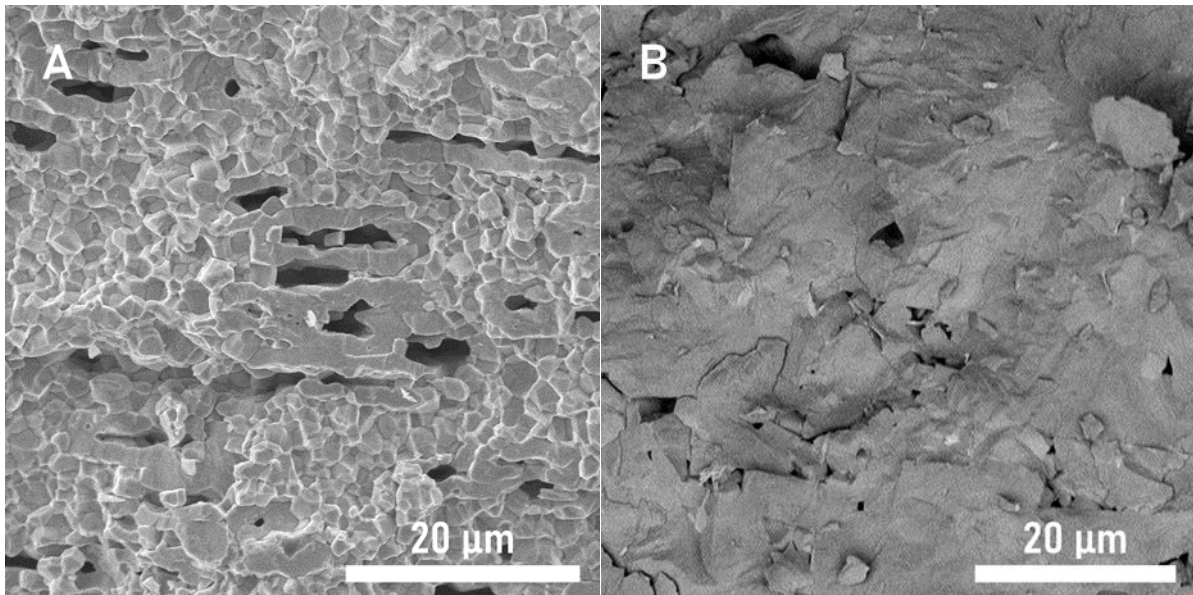


Figure 43 - a) SE image of PZT-5A1 microstructure after sintering for 2 hours at $1200 \text{ }^\circ\text{C}$; b) 8 hours.

The SE image of the PZT-5A1 microstructure after 2 hours (Figure 43a) shows an inhomogeneous microstructure with significant elongated pores as seen in the PZT52-5BT sample. A well-defined and singular textured grain layer (thickness $\sim 2 \mu\text{m}$) surrounds the remnant pores. Slight grain coarsening of the adjacent matrix grains ($\sim 1 \mu\text{m}$) has occurred, although the difference in volume between the textured grains and matrix grains remains large enough to provide significant driving force for exaggerated grain growth. No template grains can be identified within the bulk, confirming that BT is not thermally stable within the PZT-5A1 matrix. The X-ray diffraction data in section 7.3, Figure 40 suggests that there may be a compositional gradient due to the dissolution of the template grains, that is alleviated with increasing sintering time. Increasing the sintering time results in a homogeneous microstructure with extensive grain growth ($> 20 \mu\text{m}$) as seen in Figure 43b.

Comparing both PZT52-5BT and PZT-5A1 microstructures, the degree and rate of textured grain growth after initial heteroepitaxy, in the PZT-5A1 multilayers is substantially lower than that seen in the PZT52-5BT multilayers. This is believed to be due to the amount of excess PbO added, causing rapid mass transport, enabling early exaggerated grain growth prior to complete densification. The microstructural evolution of the PZT-5A1 multilayers is more controlled, with textured grain growth occurring after longer sintering times. It can be inferred that 5 wt. % PbO is far from the ideal liquid phase quantity needed to balance the rate of texture formation, i.e. grain growth, and final multilayer density, i.e. densification. Such rapid grain growth seen in the PZT52-5BT multilayers after just 6 minutes at 1200 °C, along with significant porosity and low obtained final densities (~ 91 % relative density), demonstrates the need to optimise the amount of liquid phase former within the system. As densification and grain growth are competing processes, there exists a fine balance to achieve fully textured dense multilayers (> 95 % relative density) suitable for piezoelectric applications.

Initial heteroepitaxy on top of the (00 l) template surface is reported to occur ~ 88 % relative density¹⁹⁸. After which textured grains grow via homoepitaxy, with continued dissolution-precipitation of the matrix. Further exaggerated grain growth occurs once densification has reached 92-94 % relative density. This is because pores are known to exert a drag on grain boundary migration, which if sufficiently large, will pin the grain boundary and inhibit further grain growth^{199,200}. The dissolution of the template grains in both PZT52-5BT and PZT-5A1 multilayers relieves the problem of final grain clamping due to secondary inclusions and alleviates internal sintering stresses that may result in cracking defects. However the subsequent remnant porosity is an unwanted artifact, potentially exacerbated by anisotropic densification. Further investigation into modulating the liquid phase addition is necessary, along with potentially utilising a low temperature pre-densification step to encourage texture grain formation and densification prior to significant grain growth²⁰¹.

7.4.1 Parameters affecting texture evolution in PZT multilayers

The presence of a liquid phase is critical in enabling TGG of PZT utilising heterogeneous templates. No textured grain epitaxy was noted to occur in multilayer samples without PbO additions. As the PbO liquid phase forms during heating of the PZT52-5BT multilayer, liquid flows into the channels between template and surrounding matrix grains by differences in capillary pressure. This compressive force between solid particles results in rapid particle rearrangement, i.e. reduction in interparticle distance, provided sufficient particle wetting occurs²⁰². The high particle curvature of the sub-micron matrix grains (high solubility) relative to the flat (00 l) crystal faces of the large template grains (low solubility), promotes greater dissolution of the matrix material into the liquid phase which subsequently precipitates on the template grains²⁰³. This is most clearly seen by the epitaxy layer surrounding presumed dissolved template grains in Figure 43a. This Ostwald ripening-type process, driven by the reduction in surface free energy of the system, proceeds in coarsening both newly nucleated textured grains and matrix

grains until there is no longer any liquid phase present to accommodate further dissolution-precipitation. Coarsening of the matrix is also expected to occur via this mechanism, as seen by inspecting the matrix grain sizes seen in Figure 41a-Figure 42a. Provided the initial liquid phase assisted growth of textured grains is greater than the surrounding matrix, exaggerated grain growth driven by a reduction in grain boundary surface area can result in a fully textured coarse grained microstructure.

The growth rate of the initial textured grains during dissolution-precipitation, either interface controlled and/or diffusion controlled, has a dependency on the difference in solubilities between the textured grains and the matrix grains, and hence the supersaturation of the liquid phase²⁰⁴. The matrix grain size directly affects the degree of solubility. This is especially clear by the lack of texture formation seen in PZT52-5BT multilayers when using starting micron-sized matrix powder²⁰⁵. If textured grain growth is diffusion controlled, shrinkage would be expected to be proportional to the sintering time, $t^{1/3}$, with the volume of liquid phase also becomes an important parameter affecting the growth rate^{206,207}. Higher liquid phase volumes will act to retard shrinkage, due to an increase in liquid film thickness between particles. Shrinkage for an interface controlled mechanism would be expected to be proportional to the sintering time, $t^{1/2}$. Unlike reported relaxor-PT based systems that have a certain tolerance for starting micron sized matrix grains, texturing of PZT via the TGG approach requires a substantial reduction in starting matrix grain size (sub-micron) to be successful¹⁸⁸. PZ is known to have a lower limiting solubility in PbO liquid than PT, indicating that any supersaturated liquid phase formed during the dissolution of matrix grains, is likely to have a higher Ti concentration with respect to Zr^{21,208}. It may not be unreasonable to expect slight compositional variation, and even greater tetragonality, in the region extending from the textured-template grain boundary. Future dilatometry tests should provide an indication of the rate controlling mechanism for densification, allowing for the optimisation of critical parameters, e.g. particle size, template concentration, volume liquid phase addition, affecting textured formation in the PZT system.

Constrained sintering is known to occur when sintering green bodies with large non-densifying agglomerates during TGG²⁰⁹. Before dissolution, the BT template grains can be considered as rigid, i.e. non-densifying inclusions, surrounded by low density matrix grains as seen in Figure 41, prior to sintering. Densification results from a shrinkage of the matrix, exerting a consistent compressive stress on the dense template grains²¹⁰. The PbO liquid phase addition in the PZT52-5BT matrix encourages premature densification of heteroepitaxial grains on the surface of the template grains, rendering them susceptible to significant grain growth after short sintering times²¹¹. This is exemplified by the apparent degree of [001]-texture obtained in PZT52-5BT multilayers after sintering for just 6 minutes. This dense, non-deformable textured region can grow to surround the template grains to give a textured layer as seen in [001]-textured PZT-5A1 multilayers (Figure 43a), provided the BT template remains chemically stable. For the PZT52-5BT case, dissolution of the BT templates occurs rapidly making complete texture layer growth not possible (Figure 42a). The balance between the coarsening of

nucleated textured grains versus matrix coarsening is tipped towards textured grain growth by virtue of the already large textured grain sizes obtained, most likely due to the large liquid phase content. Further densification of the matrix may result in any remnant BT templates being placed under tension and subsequently aiding in their dissolution²¹². Anisotropic sintering and the ensuing rapid grain growth, results in low final densities as the driving force for densification is retarded once grain growth begins. This is demonstrated by the maximum obtained relative density ~ 92 % for the PZT52-5BT multilayer sintered for 8 hours. The determination of a critical template concentration below which densification is enhanced and the effects of constrained sintering are negated, warrants further investigation if sufficiently dense samples are to be achieved²¹³.

7.5 [001]-textured PZT multilayers results summary

PZT + 5 vol. % BT templates and 5 wt. % PbO addition multilayers have been successfully textured via TGG. The achieved texture fraction, $f_{(001)} = 0.91$, after just 6 minutes at 1200 °C indicates rapid texturisation. A maximum $f_{(001)} = 0.94$ was obtained after 8 hours. The X-ray diffraction patterns for the PZT52-5BT samples show a slight increase in expected tetragonality, with no secondary/impurity phases present. PZT-5A1 + 5 vol. % BT templates multilayers have also been successfully textured via TGG, with a maximum $f_{(001)} = 0.86$ after sintering for 8 hours. X-ray diffraction patterns for the PZT-5A1 samples show a secondary tetragonal phase present, that decreases in volume fraction with increase sintering time. Inhomogeneous microstructures are seen in both PZT52-5BT and PZT-5A1 multilayers after relatively short sintering times (< 2 hours). PZT52-5BT shows large textured grain growth, with textured grain sizes reaching > 20 µm, along with finer matrix grains (< 5 µm) after 2 hours. The fracture surfaces suggest partial textured grain heteroepitaxy followed by rapid coarsening has occurred. Longer sintering times (> 8 hours) result in a homogeneous microstructure consisting of large textured grains (> 50 µm). PZT-5A1 shows more controlled textured grain growth after sintering for 2 hours, with a single continuous textured layers observed with thicknesses ~ 2 µm. Only after 8 hours, is a complete coarse textured microstructure observed.

In both cases it is evident that the BT templates dissolve in the PZT matrix at sintering temperature (1200 °C). Low final densities for both PZT52-5BT and PZT-5A1 multilayers are reported due to a combination of both rapid early stage grain growth and significant remnant porosity, the closure of which occurs after long sintering times (> 8 hours). Particle size has been identified as critical in enabling successful texture formation via TGG in PZT. No texture was observed in PZT52-5BT multilayers using micron-sized starting powder. The limiting solubility of the PZ member in PbO liquid is predicted to result in initial compositional variation within textured heteroepitaxial grains. Both liquid phase addition and template concentration have been highlighted as important parameters affecting constrained sintering and controlling textured grain growth, both warranting further investigation. It is now essential to perform compositional work to study the effect of 5 vol. % BT addition on the bulk

properties, including optimising the starting Zr:Ti ratio to account for BT dissolution. It is also important to know the properties of an equivalent untextured ceramic to provide a comparison with which to quantify texturisation in enhancing piezoelectric properties.

8. Compositional modification of starting PZT matrix powder

As undoped PZT has been shown to undergo TGG with 5 vol. % BT + 5 wt. % PbO in section 7.3, it is necessary to characterise the $\text{PZT}_x\text{-5BT}$ system. The MPB of undoped PZT is reported to lie at $x = 0.52$, $\text{Pb}(\text{Zr}_x\text{Ti}_{1-x})\text{O}_3$ ³². The inclusion of BT, with Ti being an end member of the PZT system, is expected to shift the MPB towards the Zr-rich side of the phase diagram. A higher Zr:Ti ratio is therefore required to attain a final bulk composition near the MPB. Compositional modification of the starting matrix powder, considering the addition of heterogeneous template materials in TGG has not been widely reported, even though attaining a final textured bulk composition near the MPB is crucial to maximise piezoelectric properties and realise the potential of novel textured fabrication with compositional optimisation. Literature on PZT-BT solid solutions prepared by mixed oxide methods report diffuse phase transition behaviour and a lowering of T_c from 390 °C to 129 °C with increasing BT content²¹⁴. There exists a wide band of compositions that exhibit relaxor phase characteristics near ferroelectric rhombohedral, ferroelectric tetragonal, and paraelectric cubic phases²¹⁵. Ikeda²¹⁶ reports the main contributing factor to stability of either ferroelectric rhombohedral/tetragonal phases to be dominated by Zr:Ti ratio and not Ba concentration. The addition of Ba^{2+} on the A-site, acts to reduce the space for the B-site cation rattling, consequently lowering the T_c and weakening ferroelectricity. There is minimal work however, looking at the effects of low level Ba-doping of PZT (< 5 mol. % Ba), modulating only the Zr:Ti ratio to attain near MPB compositions.

PZT compositions with different Zr:Ti ratio from $x = 0.52$ to 0.61, with a fixed BT addition of 5 vol. %, were synthesised according to the procedure in section 8.1. Ceramic and powder X-ray diffraction studies were performed to determine phase formation, lattice parameters, and structural information for each individual composition (section 8.2). This data is used to resolve the MPB in the $\text{PZT}_x\text{-5BT}$ system and to obtain an optimum desired starting composition for TGG experiments. Analysis of inhomogeneous samples highlights fundamental synthesis issues and illustrates major factors affecting Ba^{2+} diffusion (section 8.2.1). Density measurements combined with SEM was conducted to verify the suitability of the pellet synthesis procedure in fabricating dense samples for dielectric and piezoelectric characterisation (section 8.3). Dielectric measurements as a function of temperature were performed to determine the ferroelectric nature of the $\text{PZT}_x\text{-5BT}$ system and to identify the effect of BT on the T_c , ϵ_r , and $\tan \delta$ (section 8.4). The effect of sample homogeneity on the dielectric properties of $\text{PZT}_x\text{-5BT}$ compositions is also explored (section 8.4.1). Berlincourt measurements provide piezoelectric coefficients for randomly oriented samples within the $\text{PZT}_x\text{-5BT}$ system, from which a comparison with textured multilayers may be made (section 8.5). Electrical hysteresis and strain measurements were obtained for the optimised $\text{PZT}_x\text{-5BT}$ composition to provide a more detailed electrical overview for future reference (section 8.6). Considering all the factors, ranging from synthesis to piezoelectric

characterisation, will provide a suitable foundation to optimise the texturisation of PZT, and more generally provide a better scope for Pb-based material optimisation using TGG.

8.1 Synthesis methodology for PZTx-5BT ceramics

PZT + 5 vol. % BT pellets with modified starting Zr:Ti ratios ($x = 0.52, 0.53, \dots 0.61$) were synthesised using PbO (99.9 % purity, Alfa Aesar), ZrO₂ (99 % purity, Sigma-Aldrich), TiO₂ (rutile, ≥ 99.9 % purity, Sigma-Aldrich), and BT (Entekno Materials) powder reagents. Both ZrO₂ and TiO₂ starting reagents were dried at 900 °C for 8 hours prior to weighing. The starting reagents were weighed into individual 5 g (small) and 10 g (large) batches according to batch calculations shown in Appendix C. A 20:1 mass ratio of cylindrical yttria stabilized zirconia (YSZ) milling media (10 mm \varnothing x10 mm) to reagent powder was placed in individual 125 mL HDPE Nalgene bottles along with the weighed starting reagents and a 5:1 volume ratio of isopropanol (≥ 99.9 % purity, Merck) to reagent powder. The reagent powders were subsequently mixed via ball milling for 24 hours. The milling media was removed using a sieve and the mixed reagent powders transferred into a box furnace set at 80 °C overnight to evaporate off the remaining solvent. The dried mixed powders were sieved using a 150 μ m mesh size sieve to ensure no significant agglomeration and then placed in closed alumina crucibles in preparation for calcination. The dried mixed powders were calcined in a box furnace at 800 °C for 2 hours, with a heating/cooling rate of 10 °C/min.

Table 4 - Final stoichiometric PZTx-5BT compositions with starting Zr/Ti ratios of PZT component.

composition	chemical formula	starting Zr/Ti ratio	final Zr/Ti ratio
PZT52-5BT	Pb _{0.948} Ba _{0.052} Zr _{0.493} Ti _{0.507} O ₃	1.083	0.972
PZT53-5BT	Pb _{0.948} Ba _{0.052} Zr _{0.502} Ti _{0.498} O ₃	1.128	1.008
PZT54-5BT	Pb _{0.947} Ba _{0.053} Zr _{0.512} Ti _{0.488} O ₃	1.174	1.049
PZT55-5BT	Pb _{0.947} Ba _{0.053} Zr _{0.521} Ti _{0.479} O ₃	1.222	1.088
PZT56-5BT	Pb _{0.947} Ba _{0.053} Zr _{0.531} Ti _{0.469} O ₃	1.273	1.132
PZT57-5BT	Pb _{0.947} Ba _{0.053} Zr _{0.540} Ti _{0.460} O ₃	1.326	1.174
PZT58-5BT	Pb _{0.947} Ba _{0.053} Zr _{0.549} Ti _{0.451} O ₃	1.381	1.217
PZT59-5BT	Pb _{0.947} Ba _{0.053} Zr _{0.559} Ti _{0.441} O ₃	1.439	1.268
PZT60-5BT	Pb _{0.947} Ba _{0.053} Zr _{0.568} Ti _{0.432} O ₃	1.500	1.315
PZT61-5BT	Pb _{0.947} Ba _{0.053} Zr _{0.578} Ti _{0.422} O ₃	1.564	1.370

*reported undoped MPB PZT compositions has Zr/Ti value ~ 1.083

The calcined powders were ball-milled for 24 hours using the same media to powder and solvent to powder ratios stated previously, with an additional 10 wt. % polyvinyl acetate (PVA) solution (5 wt. % PVA, 95 wt. % de-ionised water) to act as a binder. The milling media was removed using a sieve and

the calcined powders transferred into a box furnace set at 80 °C overnight to evaporate the remaining solvent. The dried calcined powders were re-sieved using a 150 µm mesh to ensure no significant agglomeration. The calcined powders were loaded into a 10 mmØ die and pressed at ~ 125 MPa for 10 seconds using a uniaxial press. The pressed green pellets were weighed, then placed on platinum foils sitting on a bed of PZ powder in an alumina crucible and individually enclosed using smaller upturned alumina crucibles. The seals between the outer and smaller upturned crucibles encapsulating the pellets were covered further with PZ powder to regulate the PbO atmosphere formed during sintering and to avoid substantial PbO loss from the pellets. The pellets were heated in a box furnace to 550 °C for 3 hours, with a heating rate of 1 °C/min, to ensure complete binder burnout and then sintered at 1250 °C for 2 hours, with a heating/cooling rate of 10 °C/min. The sintered pellets were re-weighed to give an approximation for PbO loss.

8.2 X-ray diffraction analysis of PZTx-5BT ceramics

Powder X-ray diffraction patterns for all PZTx-5BT compositions synthesised from the 5 g batch were analysed according to the procedures outlined in sections 4.2.4 and 4.2.5. The powder X-ray diffraction patterns for all studied compositions are shown in Figure 44-Figure 45.

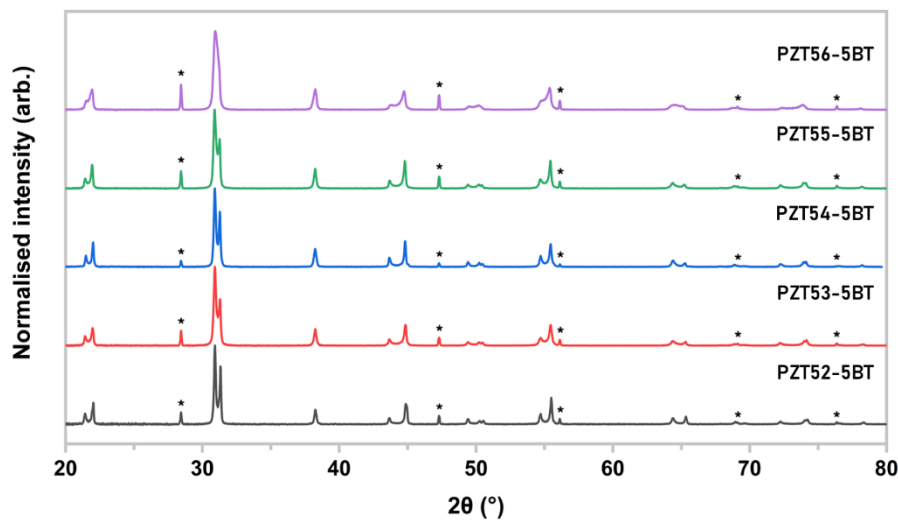


Figure 44 - X-ray diffraction patterns for tetragonal PZTx-5BT compositions, with starting 52-56 Zr mol. %, after 2 hour dwell time at 1250 °C. NIST640d Si reference material peaks are denoted with *.

The PZTx-5BT compositions with $0.52 \leq x \leq 0.55$ (Figure 44) may be indexed according to a single tetragonal perovskite structure (space group $P4mm$, no. 99). No secondary tetragonal or impurity peaks relating to the inclusion of BT are present. The doublets of the $(001)_t/(100)_t$ and $(002)_t/(200)_t$ peaks around $\sim 22^\circ$ and $\sim 44^\circ$ respectively (Figure 46a) are an indication of the reported structure due to differences in the tetragonal unit cell parameters: $a \neq c$. As the starting PZT Zr:Ti ratio increases, the

doublet $(001)_t/(100)_t$ and $(002)_t/(200)_t$ peaks move closer together, finally merging into a singlet $(001)_r$ and $(002)_r$ peak (Figure 46b). This change occurs over a narrow compositional interval, and there exists phase coexistence typical of the MPB in PZT based systems due to the flattening of the free energy profiles of tetragonal and rhombohedral structures. The X-ray diffraction patterns of compositions with $0.55 \leq x \leq 0.57$, exhibit phase coexistence with a decrease in intensity of the $(002)_t/(200)_t$ doublet peaks, accompanied by an increase in the $(002)_r$ singlet peak as Zr concentration increases. The volume fractions of tetragonal and rhombohedral phases in the samples exhibiting phase coexistence have not been obtained due to the difficulty deconvoluting the merged peaks and lack of a suitable ICDD reference for Ba-doped PZT. A Rietveld refinement method would be necessary to obtain accurate phase fractions.

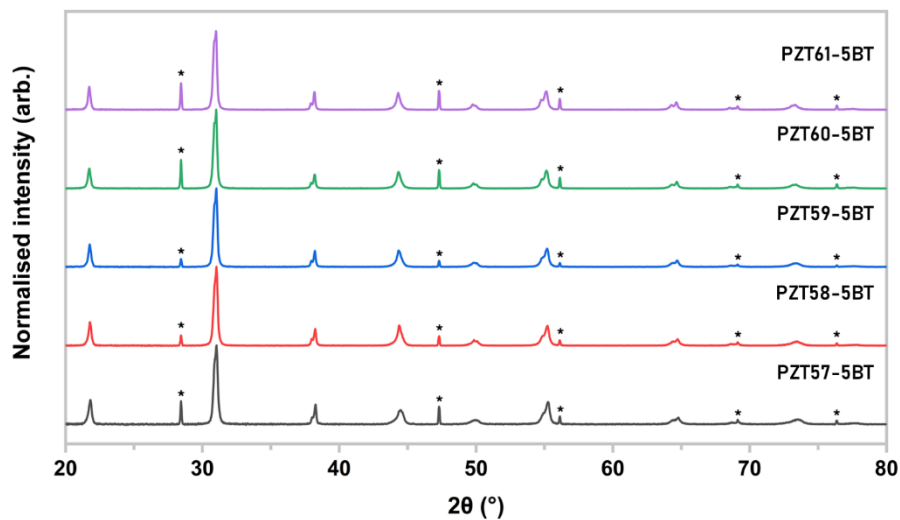


Figure 45 - X-ray diffraction patterns for rhombohedral PZT_x-5BT compositions, with starting 57-61 Zr mol. %, after 2 hour dwell time at 1250 °C. NIST640d Si reference material peaks are denoted with an *.

The compositions with $0.57 \leq x \leq 0.61$ (Figure 45) exhibit a single perovskite phase, consistent with a rhombohedral structure (space group $R3m$, no. 160). Only singlet peaks are observed and no secondary tetragonal peaks relating to the inclusion of BT can be seen in the X-ray diffraction patterns.

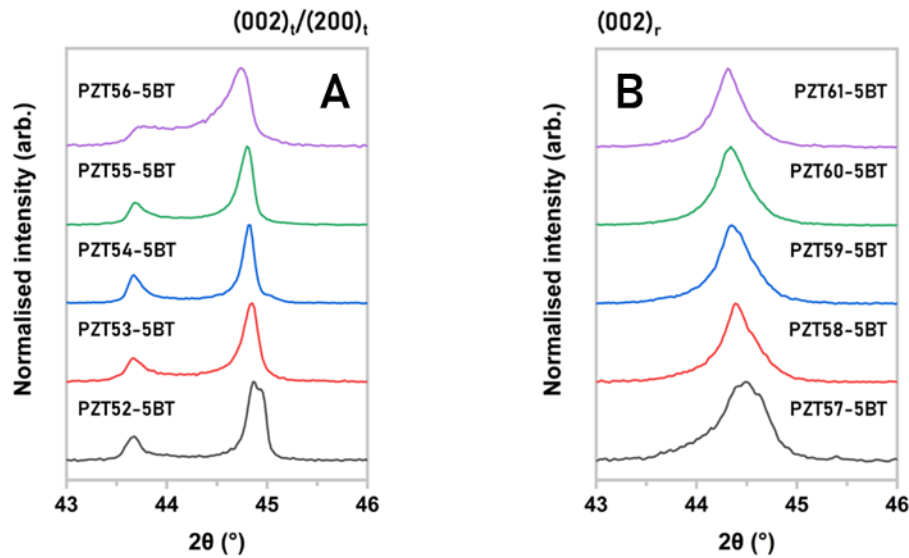


Figure 46 - a) Enlargement of $(002)_t/(200)_t$ doublet peaks for tetragonal PZT_x-5BT compositions (from Figure 44); b) $(002)_r$ singlet peaks for rhombohedral PZT_x-5BT compositions (from Figure 45).

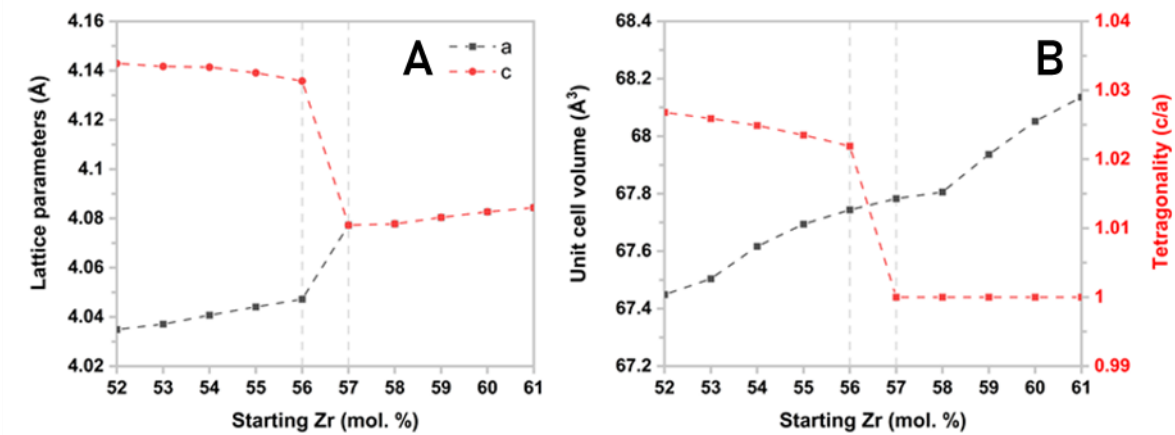


Figure 47 - a) Calculated a and c unit cell parameters vs. starting Zr mol. %; b) cell volume and c/a ratio vs. starting Zr mol. %.

The obtained unit cell parameters for the PZT_x-5BT compositions are shown in Figure 47a. The transition from tetragonal to rhombohedral is highlighted by the decrease in c/a ratio, converging to unity in the rhombohedral phase (Figure 47b). In practice, it is very difficult to fully deconvolute the merged peaks of both tetragonal and rhombohedral structures present in the near MPB compositions and therefore distinguish their respective unit cell parameters. The degree of error in the calculated unit cell parameters for samples with phase coexistence is dependent on the satisfactory deconvolution of such peaks.

For $PZT56-5BT$, the composition nearest to the MPB, deconvolution of merged peaks was necessary to obtain lattice parameters of the dominant tetragonal phase. A pseudo-Voigt function was fitted on

certain convoluted peaks using the Multiple Peak Fit tool in OriginPro 2020 (OriginLab Corporation), and the obtained 2θ angles for both phases distinguished using tetragonal²¹⁷ and rhombohedral²¹⁸ reference patterns from the ICDD database analysed in CrystalDiffract (CrystalMaker Software Ltd.). The identified 2θ angles for the tetragonal phase were input directly into the .pks file generated by the peak finding module, part of the WinX^{POW} (STOE & Cie GmbH) software suite. Whilst this approach resulted in large calculated errors when running the DICVOL4 indexing routine¹⁹² (section 4.2.5) to obtain lattice parameters, it is sufficient to highlight the general trend of decreasing c/a ratio as the MPB is approached. Thus it should be stressed that the obtained lattice parameters should be treated as indicative rather than exact. A more complete approach would be to extract lattice parameters by refining both tetragonal and rhombohedral structures simultaneously using a Rietveld refinement method.

From the X-ray diffraction data, the MPB for the PZT_x-5BT system lies ~ 56 starting Zr mol. %. The optimised PZT matrix composition tailored to an addition of 5 vol. % BT templates for TGG is PbZr_{0.56}Ti_{0.44}O₃.

8.2.1 Secondary phase in synthesised PZT_x-5BT ceramics

Although small batches of PZT with 5 vol. % BT templates could be fabricated readily, extensive characterisation of TGG requires relatively large amounts of powder (> 50 g) for multiple tapecasting attempts. Therefore, larger batch sizes were fabricated. Whilst the X-ray diffraction patterns for compositions with $x < 0.57$ were similar to those of the small batch reported in section 8.2, significant phase coexistence was identified in certain large batch compositions with $x \geq 0.57$ (rhombohedral). Ceramic X-ray diffraction patterns for rhombohedral PZT_x-5BT samples synthesised from certain larger batches are shown in Figure 48.

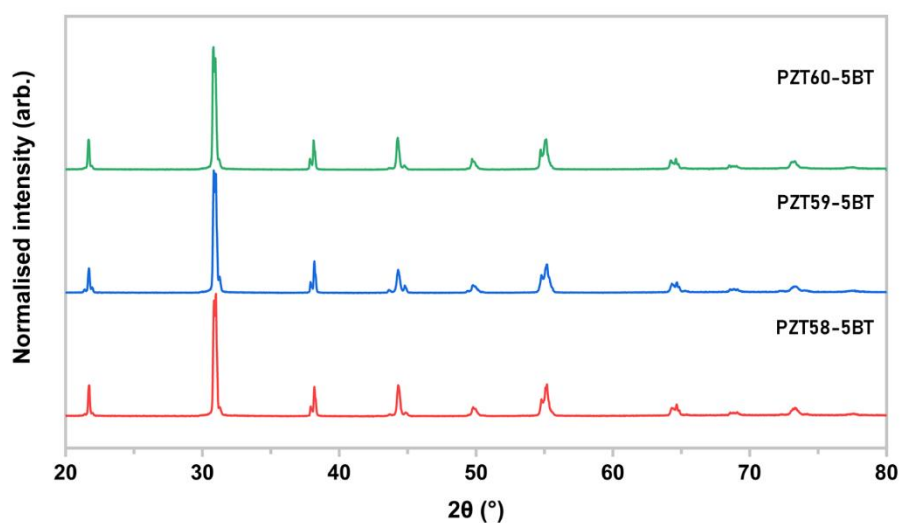


Figure 48 - X-ray diffraction patterns for inhomogeneous rhombohedral PZT_x-5BT compositions exhibiting phase coexistence after 2 hour dwell time at 1250 °C.

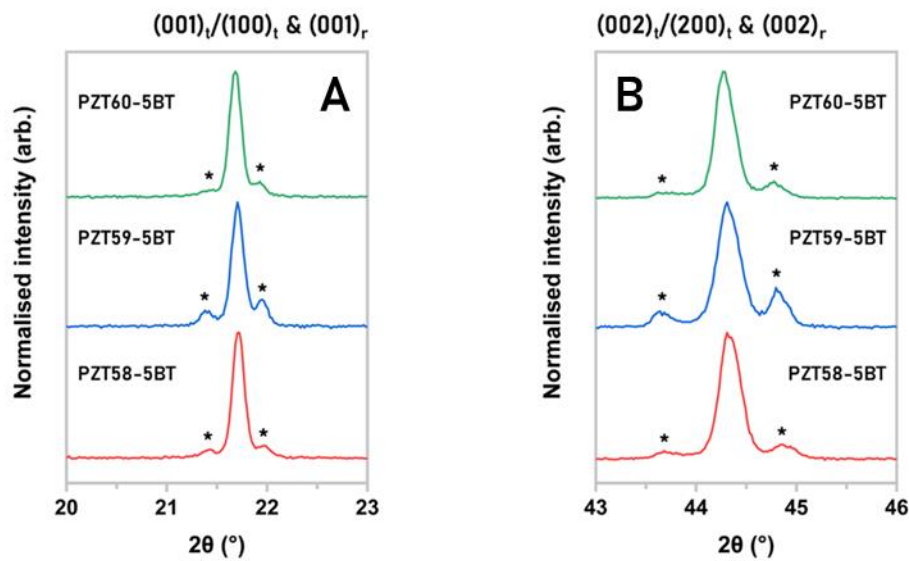


Figure 49 - a) Enlargement of coexisting (001)_t/((100)_t doublet and (001)_r singlet peaks for inhomogeneous rhombohedral PZT_x-5BT compositions (from Figure 48); b) coexisting (002)_t/((200)_t doublet and (002)_r singlet peaks.

Phase coexistence is best exemplified by the peaks $\sim 22^\circ$ and $\sim 44^\circ$ (Figure 49) with both the (00l)_t/((100)_t tetragonal doublet and (00l)_r singlet peaks present. Phase coexistence on the rhombohedral side of the MPB suggests that the apparent tetragonal phase is due to the inhomogeneous distribution of Ba within the system. Undoped PZT compositions undergo significant diffusion of Ti⁴⁺ and Zr⁴⁺ during sintering to overcome residual phase coexistence after calcination, with PZT exhibiting broad convoluted X-ray diffraction peaks at 800 °C (calcination temperature)²¹⁹. As no excess PbO was added to the PZT_x-5BT samples prior to sintering, the comparison between the peaks present in the X-ray diffraction data for the textured PZT-5A1 samples sintered for 2 hours (section 7.3, Figure 40) and the phase coexistence shown in Figure 48, both point to insufficient interdiffusion of A-site cations leading to compositional inhomogeneity. Possible synthesis problems giving rise to such inhomogeneity, and consequently phase coexistence, are explored further in sections 8.3 and 8.4.1.

8.3 Microstructural characterisation of PZT_x-5BT ceramics

The densities of all the sintered pellets, fabricated from varying batch sizes were measured using the Archimedes principle according to the procedure in section 4.1, along with examination of polished microstructures for both single-phase and suspected inhomogeneous PZT_x-5BT samples via SEM (sections 4.3 and 4.3.1). The obtained densities with calculated percentage theoretical densities are

shown in Table 5-Table 6. SEM images for both homogeneous and inhomogeneous samples are shown in Figure 50-Figure 51, and Figure 52-Figure 53, respectively.

All sintered PZTx-5BT ceramics achieved theoretical densities greater than 95 %. Such high densities are necessary to avoid detrimental effects of porosity or other microstructural defects on electrical properties, and to qualify the suitability of the sintering regime (section 8.1) employed with specific regard to PbO loss and binder burnout.

Table 5 - PZTx-5BT sample density measurements fabricated from smaller batch sizes with calculated percentage theoretical densities.

composition	sample 1 density		sample 2 density		sample 3 density	
	(g/cm ³)	(%)*	(g/cm ³)	(%)*	(g/cm ³)	(%)*
PZT52-5BT	7.526	95.27	7.535	95.38	7.538	95.42
PZT53-5BT	7.597	96.16	7.566	95.77	7.568	95.80
PZT54-5BT	7.573	95.86	7.582	95.97	7.558	95.67
PZT55-5BT	7.583	95.99	7.562	95.72	7.587	96.04
PZT56-5BT	7.519	95.18	7.533	95.35	7.527	95.28
PZT57-5BT	7.584	96.00	7.585	96.01	7.590	96.08
PZT58-5BT	7.557	95.66	7.534	95.37	7.523	95.23
PZT59-5BT	7.627	96.54	7.639	96.70	7.623	96.49
PZT60-5BT	7.563	95.73	7.534	95.48	7.532	95.34
PZT61-5BT	7.576	95.90	7.517	95.15	7.527	95.28

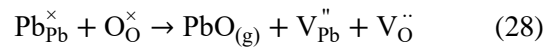
*maximum calculated theoretical density approximated to 7.9 g/cm

Table 6 - PZTx-5BT sample density measurements fabricated from larger batch sizes with calculated percentage theoretical densities.

composition	sample 1 density		sample 2 density		sample 3 density	
	(g/cm ³)	(%)*	(g/cm ³)	(%)*	(g/cm ³)	(%)*
PZT52-5BT	7.565	95.76	7.557	95.66	7.567	95.78
PZT53-5BT	7.575	95.89	7.596	96.15	7.570	95.82
PZT54-5BT	7.642	96.73	7.610	96.33	7.614	96.38
PZT55-5BT	7.673	97.13	7.682	97.24	7.674	97.14
PZT56-5BT	7.641	96.72	7.619	96.44	7.626	96.53
PZT57-5BT	7.717	97.68	7.714	97.65	7.668	97.06
PZT58-5BT	7.650	96.84	7.640	96.71	7.656	96.91
PZT59-5BT	7.641	96.72	7.645	96.77	7.657	96.92
PZT60-5BT	7.657	96.92	7.643	96.75	7.663	97.00
PZT61-5BT	7.660	96.96	7.646	96.78	7.616	96.41

*maximum calculated theoretical density approximated to 7.9 g/cm³

The averaged density across all of the samples synthesised from larger batch sizes suggest a slight improvement. This may be explained by the varying loss of PbO during sintering. The Kröger-Vink notation of PbO volatilisation from the bulk material is shown below:



PbO loss becomes significant at higher temperatures, especially at those required for sintering (> 1200 °C). If the atmospheric PbO partial pressure is less than the PbO vapour pressure (dissociation pressure) of the material, the sample will give up PbO until an equilibrium has been reached. In this case however, the use of PZ as a sacrificial powder is intended to avoid any PbO loss from the green pellets during sintering. It is understood that slight PbO deficient samples have been reported to have improved final densities than starting stoichiometric/excess PbO samples⁴², suggesting densification in the PZT system is dependent on oxygen vacancy concentration⁴⁸. BT requires higher sintering temperatures > 1300 °C to achieve adequate densities³². The slight decrease in sample densities in certain batches may be an indication of satisfactory Ba incorporation throughout the bulk, as Ba²⁺ has been reported to suppress oxygen vacancy formation in PZT by nature of having a stronger oxygen bond energy than Pb²⁺ (Ba-O 562 kJ/mol, Pb-O 382 kJ/mol)²²⁰.

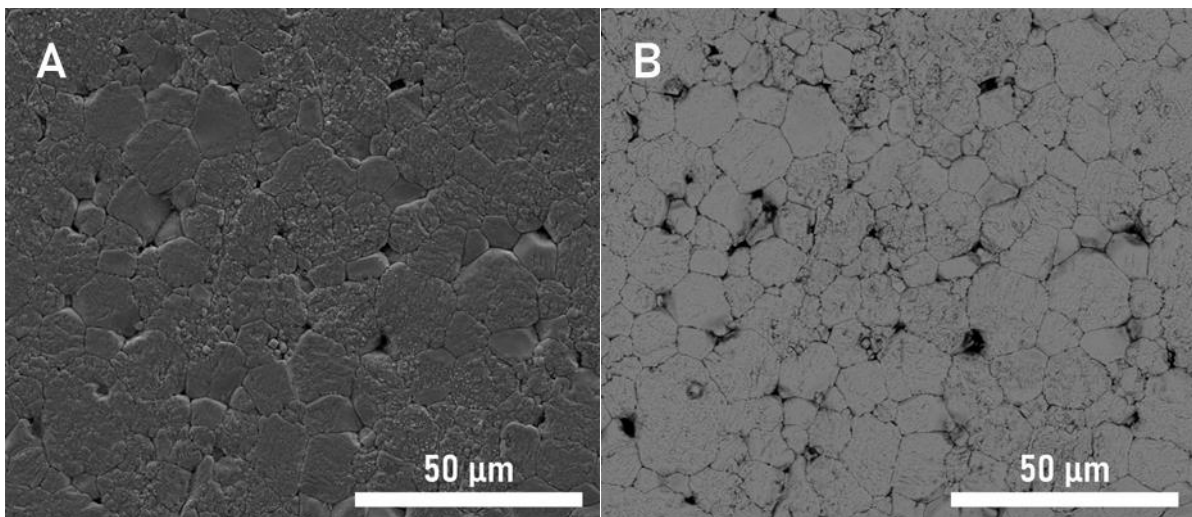


Figure 50 - a) SE image of homogeneous PZT_x-5BT microstructure with grain boundaries revealed; b) BSE image.

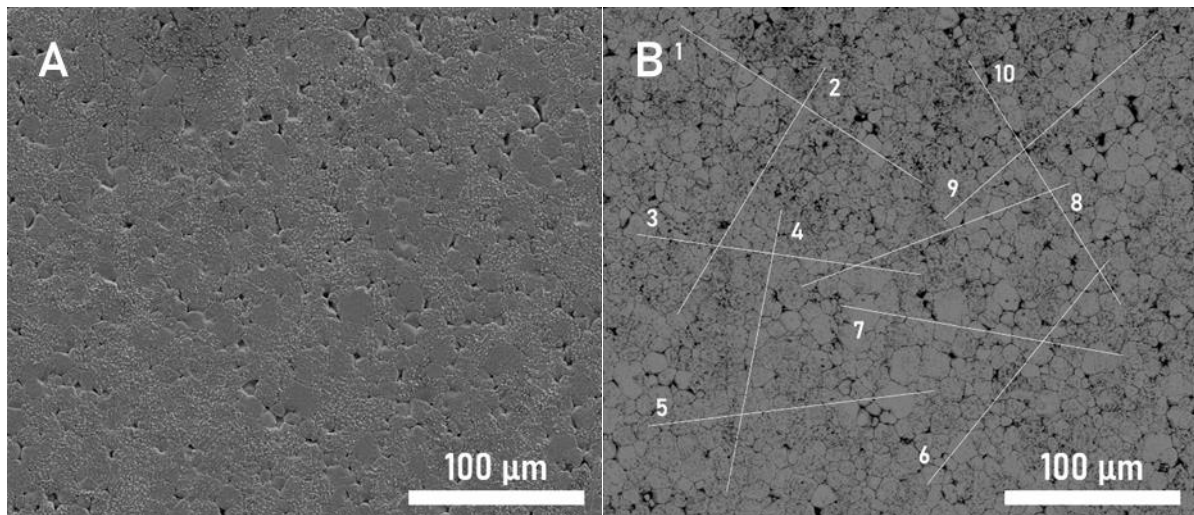


Figure 51 - a) SE image of homogeneous PZTx-5BT microstructure with grain boundaries revealed; b) BSE image with mean liner intercept method annotations for grain size analysis.

The microstructure for the homogeneous ceramic pellets shown in Figure 50-Figure 51 indicates that final stage sintering has occurred at the sintering temperature of 1250 °C after 2 hours, with isolated pores located along grain boundaries and triple points. No continuous pore channels can be observed, characteristic of incomplete densification, with reported density measurements confirming satisfactory pellet densities have been achieved with the employed sintering regime. An average grain size of 14.6 μm was obtained via the mean liner intercept method. BSE images fail to show any secondary phases or chemical inhomogeneity.

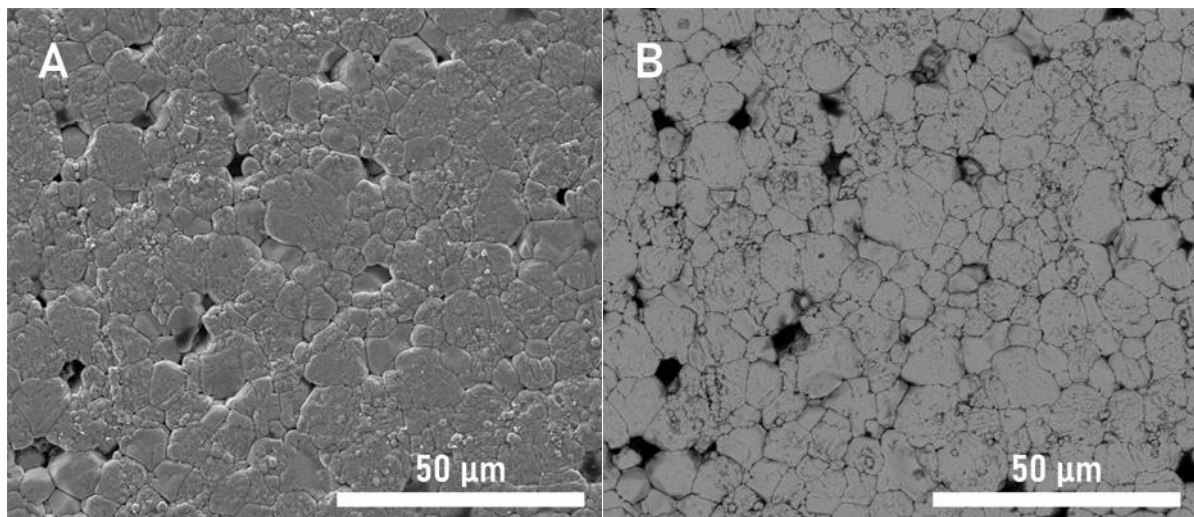


Figure 52 - a) SE image of inhomogeneous PZTx-5BT microstructure with grain boundaries revealed; b) BSE image.

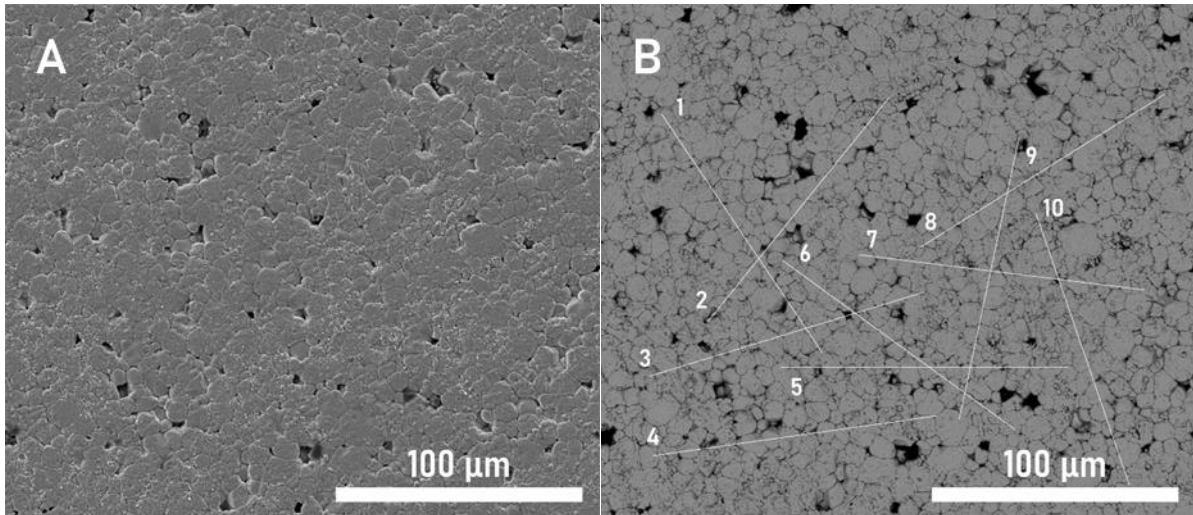


Figure 53 - a) SE image of inhomogeneous PZTx-5BT microstructure with grain boundaries revealed; b) BSE image with mean liner intercept annotations for grain size analysis.

The microstructure for the suspected inhomogeneous ceramics, shown in Figure 52-Figure 53 suggests that final stage sintering has occurred. An average grain size of 9 μm was obtained via the mean liner intercept method. BSE images fail to show significant compositional inhomogeneity. Attempts at EDS analysis to distinguish regions of high Ba concentration were unsuccessful due to the overlapping Ba $L\alpha_1$ (4.466 keV) and Ti $K\alpha_1$ (4.512 keV) spectral lines. Due to the low concentration of added BT with respect to the main precursor PZT, the resolution of the EDS probe may be insufficient in distinguishing the spatial distribution of Ba. Further investigation using a more sensitive instrument, such as an electron probe micro-analyser (EPMA), may provide better data, suitable in determining the levels of Ba inhomogeneity within the bulk.

8.4 Dielectric properties of PZTx-5BT ceramics

Dielectric data for all PZTx-5BT compositions synthesised from small batches were obtained according to the procedure outlined in section 4.4. The T_c of MPB PZT ($\text{PbZr}_{0.52}\text{Ti}_{0.48}\text{O}_3$) can be deduced from the PZT phase diagram (section 2.2, Figure 2) to be $\sim 380^\circ\text{C}$. From the PZT phase diagram, increasing the Zr:Ti ratio is likely to result in a reduction in T_c . Moreover, BT is known to have a much lower $T_c \sim 120^\circ\text{C}$ than PZT and generally, isovalent A-site dopants, e.g. Sr^{2+} , Ba^{2+} are also reported to lower the T_c in the PZT system²²¹. It is therefore expected that the T_c for the PZTx-5BT compositions will be lower than undoped PZT, with a decreasing trend in T_c as the Zr:Ti ratio increases. $\epsilon_{r,RT}$ is reported to increase in compositions near to the MPB for PZT. The change in crystal structure from tetragonal to rhombohedral identified at ~ 56 Zr mol. % in the PZTx-5BT system should be accompanied by an increase in room temperature ϵ_r . ϵ_r as a function of temperature for tetragonal and rhombohedral PZTx-5BT compositions are shown in Figure 54.

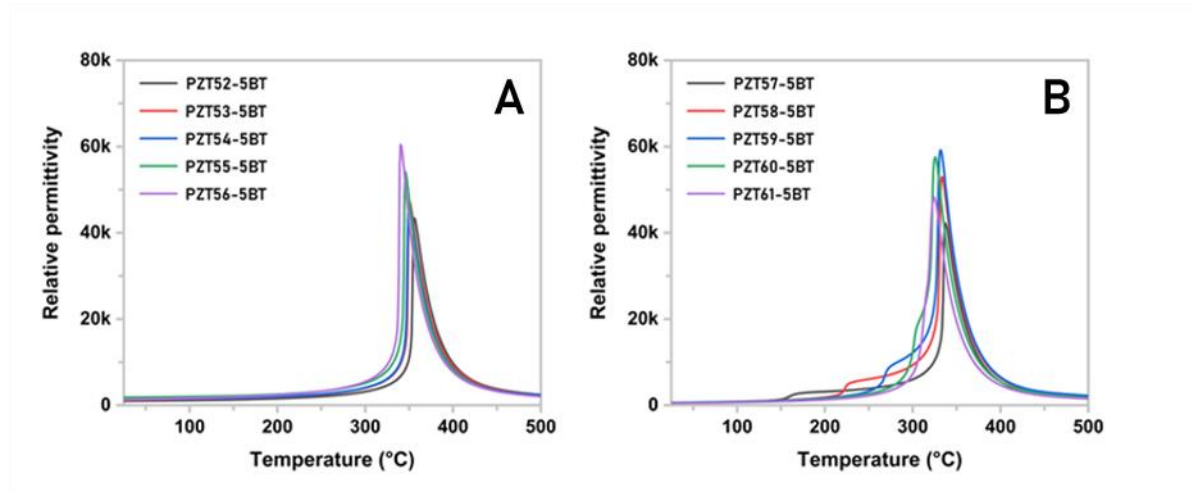


Figure 54 - a) ϵ_r vs. temperature for tetragonal PZT_x-5BT compositions; b) rhombohedral PZT_x-5BT compositions.

All tetragonal samples (Figure 54a) exhibit a sharp singular ϵ_r peak, with the narrow peak width an indication of sample homogeneity. Across the whole studied range, the expected decrease in T_c is apparent with increasing Zr content, by 2-5 °C/mol. % Zr increase (Figure 56b). For the tetragonal PZT_x-5BT compositions, the ϵ_r maxima increases as the final Zr:Ti ratio approaches the MPB, with $\epsilon_r \sim 60,000$ for the PZT56-5BT composition. The $T_c \sim 340$ °C for PZT56-5BT shows a decrease of ~ 40 °C with respect to the MPB of undoped PZT.

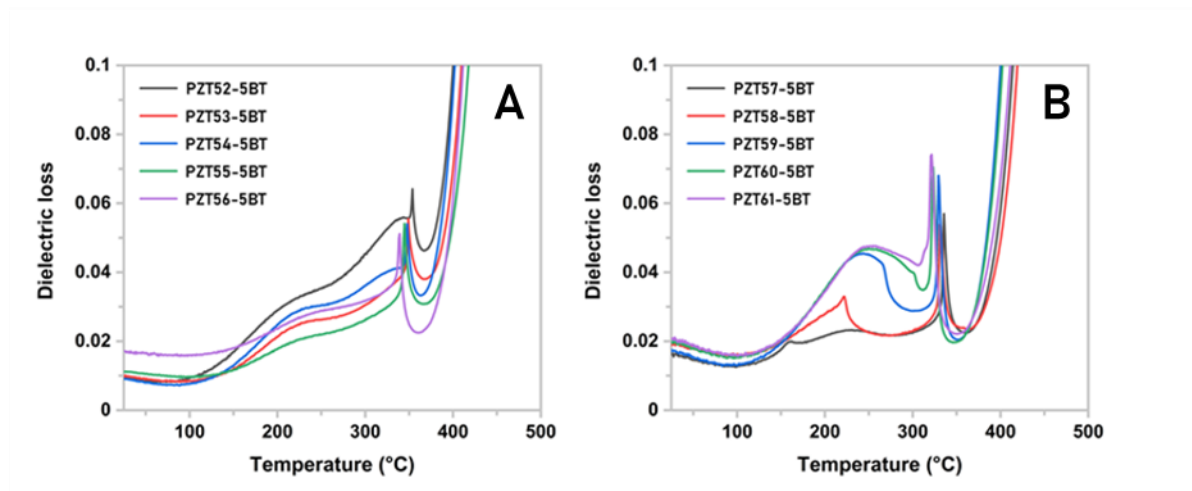


Figure 55 - a) $\tan \delta$ vs. temperature for tetragonal PZT_x-5BT compositions; b) rhombohedral PZT_x-5BT compositions.

As the ambient temperature structure changes from tetragonal to rhombohedral, a secondary dielectric hump is visible in the rhombohedral compositions (Figure 54b), as well as a sharp T_c peak. This secondary hump increases non-linearly in temperature with increasing Zr concentration, starting at ~ 160 °C for PZT57-5BT composition, to ~ 314 °C for PZT61-5BT composition (Figure 56b). The appearance of this low temperature peak is analogous to the low temperature ferroelectric-ferroelectric

phase transition (T_{r-t}) seen in binary and ternary relaxor-PT based perovskite systems, e.g. PMN-PT and PIN-PMN-PT. The non-linear nature of the transition temperature dependence on composition indicates that the MPB in the PZT_x -5BT system is not completely temperature independent, rather the inclusion of BT is causing a slight curvature in the MPB towards the rhombohedral side with respect to temperature, i.e. the appearance of a T_{r-t} , whilst generally depressing the T_c .

The $\tan \delta$ data for tetragonal and rhombohedral compositions are shown in Figure 55. A singular $\tan \delta$ peak is visible for all tetragonal compositions (Figure 55a) at the same temperature as the corresponding ϵ_r maximum. $\tan \delta_{RT}$ for tetragonal compositions between $x = 0.52$ - 0.55 are $\sim 1\%$, with the PZT56-5BT composition having a slightly elevated $\tan \delta_{RT}$ of 1.5% . The $\tan \delta_{RT}$ value and reported T_c places the PZT56-5BT composition within the Navy type II classification for piezoelectric materials, similar to commercially available PZT-5A1²²². The rhombohedral compositions (Figure 55b) exhibit secondary peaks increasing in temperature with increasing Zr content. The secondary peaks appear much lower in intensity than the major anomaly related to T_c whilst becoming broader/more diffuse with increasing Zr concentration.

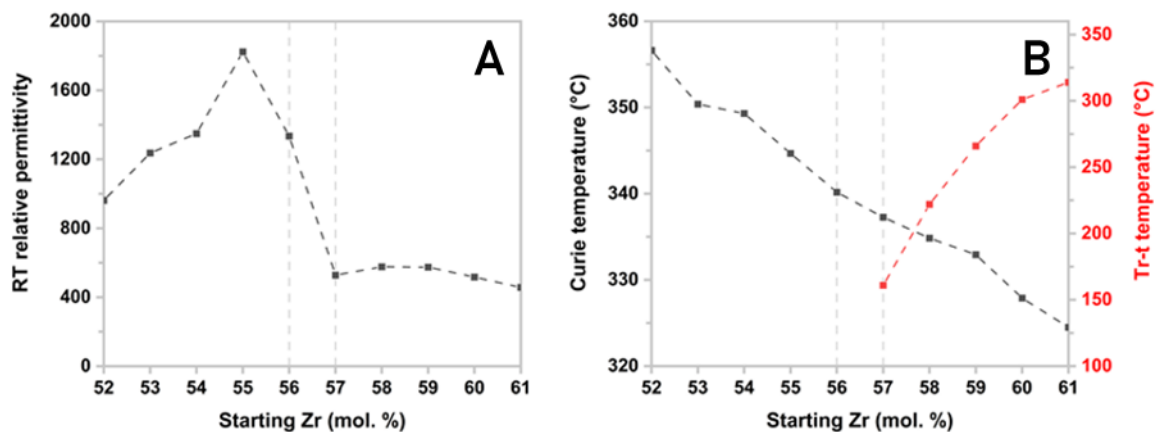


Figure 56 - a) ϵ_{rRT} vs. starting Zr mol. %; b) T_c and T_{r-t} (only seen in rhombohedral compositions) vs. starting Zr mol. %.

ϵ_{rRT} data shows an increase in ϵ_{rRT} with increasing Zr concentration in the tetragonal phase, up to a maximum $\epsilon_{rRT} \sim 1820$ for the PZT55-5BT (Figure 56a). The ϵ_{rRT} values on the rhombohedral side are markedly lower, with $\epsilon_{rRT} \sim 500$. Whilst the PZT56-5BT composition has a lower $\epsilon_{rRT} \sim 1330$, the composition lies on the downward slope of the ϵ_{rRT} maximum, thereby suggesting the exact MPB lies between starting 55-56 Zr mol. %.

The addition of 5 vol. % BT has generally improved dielectric properties whilst only slightly decreasing T_c by $\sim 40^\circ\text{C}$. $\tan \delta_{RT}$ of 1.5% is comparable with commercially available ‘soft’ PZT. These factors suggest that the prospect of successful texturisation of PZT_x -5BT is possible, provided the piezoelectric properties of PZT_x -5BT follow the expected trends for MPB compositions.

8.4.1 Dielectric properties of inhomogeneous PZTx-5BT ceramics

The relative permittivities for all PZTx-5BT compositions with apparent compositional inhomogeneity, as identified from the X-ray diffraction patterns in section 8.2.1, are shown in Figure 57.

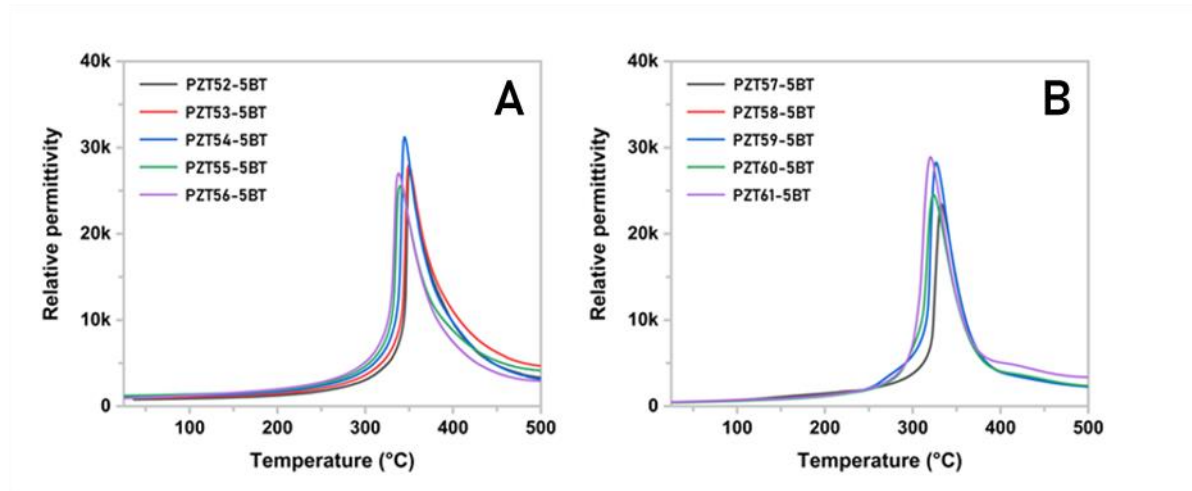


Figure 57 - a) ϵ_r vs. temperature for tetragonal PZTx-5BT compositions; b) rhombohedral PZTx-5BT compositions.

The tetragonal compositions (Figure 57a) show a more diffuse ϵ_r maximum in comparison with the homogeneous samples, with maximum ϵ_r values substantially lower, $\epsilon_r \sim 30,000$ for PZT54-5BT. Both factors are consistent with compositional variation throughout the bulk. The rhombohedral compositions (Figure 57b) exhibit broad T_c peaks, with the low temperature anomalies seen in the homogeneous samples suppressed. A similar trend in reduction of T_c with increasing Zr concentration is apparent in all compositions.

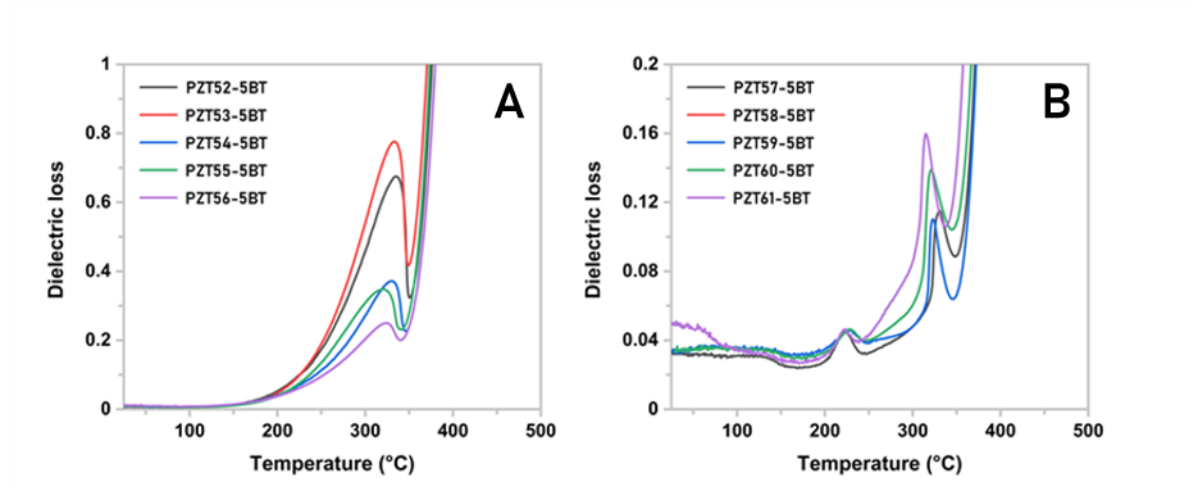


Figure 58 - a) $\tan \delta$ vs. temperature for tetragonal PZTx-5BT compositions; b) rhombohedral PZTx-5BT compositions.

$\tan \delta$ vs. temperature plots for tetragonal and rhombohedral compositions are shown in Figure 58. A single diffuse $\tan \delta$ peak is visible for all tetragonal compositions (Figure 58a). Rhombohedral compositions exhibit two distinct $\tan \delta$ peaks (Figure 58b), although the apparent low temperature peak is independent of Zr content unlike in the homogeneous rhombohedral samples. All rhombohedral compositions show a secondary $\tan \delta$ peak at ~ 220 °C. This suggests that the composition of the local phase related to the secondary $\tan \delta$ peak is constant, irrespective of the starting composition of the PZT powder. It can therefore be inferred that the secondary phase across all inhomogeneous samples originates from the clustering of Ba.

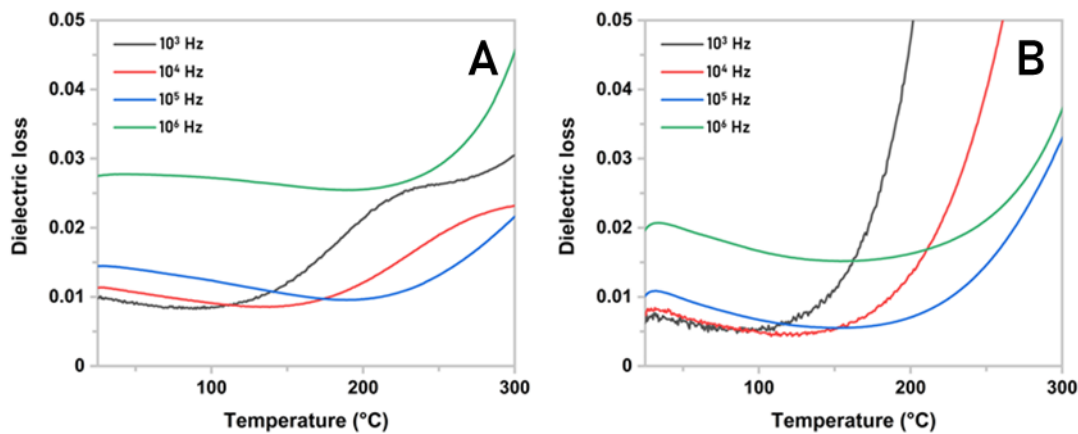


Figure 59 - a) $\tan \delta$ vs. temperature varying frequency plots for homogeneous PZT54-5BT; b) for inhomogeneous PZT54-5BT.

Comparison between the frequency dependence of $\tan \delta$ vs. temperature data for both homogeneous (Figure 59a) and inhomogeneous (Figure 59b) tetragonal PZT54-5BT samples indicates a differing frequency dependence of $\tan \delta$ between specimens. The homogeneous sample shows an increase in $\tan \delta_{RT}$, which can be explained by facilitated domain wall mobility due to isovalent doping of Pb^{2+} with Ba^{2+} , resulting in increased losses associated with such enhanced mobility. This suggests that Ba^{2+} substitution of Pb^{2+} throughout the matrix imparts some ‘soft’ piezoelectric character, supported by large improvements in d_{33} compared with inhomogeneous samples (section 8.5, Table 7). It may also be the case that suppression of V_{O} formation in homogeneous PZT x -5BT ceramics, negates the appearance of any ‘hard’ character, visible in samples with compositional variation²²⁰. Below T_c there exists a weak frequency dependence of $\tan \delta$ in the homogeneous samples, along with near temperature independent behaviour up to 300 °C explained by a broad distribution of Debye type dielectric relaxation times associated with collective easy movement of domain walls²²³. On the other hand the inhomogeneous sample shows a strong frequency dependence of $\tan \delta$, exhibiting large conductivity losses at temperatures > 100 °C, characteristic of acceptor-doped compositions. Narrowing of the distribution of relaxation times responsible for domain wall losses at ambient temperatures, results in a

lower $\tan \delta_{RT}$ value for the inhomogeneous sample. The apparent ‘hard’ character exhibited in inhomogeneous samples suggests that PbO loss has occurred from the specimen, with the resulting V_{O} known to stabilise domain structures, reducing ambient temperature losses associated with domain wall motion^{67,68}. The variation in phase homogenisation with respect to BT incorporation, highlighted from the X-ray diffraction data, can be seen to have a dramatic effect on whether ‘soft’ or ‘hard’ piezoelectric character is attained. This adds greater emphasis on ensure that sufficient interdiffusion between A-site cations occurs during calcination/sintering for ceramic processing, and during liquid phase sintering when attempting TGG of PZT using BT templates, to obtain high d_{33} textured multilayer ceramics.

In the case of rhombohedral PZT_x-5BT compositions, sufficient interdiffusion between A-site cations ($\text{Ba}^{2+}/\text{Pb}^{2+}$) from starting BT and PZT precursors along with concurrent interdiffusion of the B-site cations ($\text{Ti}^{4+}/\text{Zr}^{4+}$), is expected to result in a single phase rhombohedral perovskite structure at room temperature after sintering (section 8.2, Figure 45). In samples where this is not the case, i.e. inhomogeneous samples, due to a variety of processing factors, there will be regions of both high and low concentrations of Ba. The local regions with high Ba concentrations can be assumed to have a tetragonal perovskite structure, due to the tetragonality of starting BT phase ($c/a = 1.01$)³². Conversely the regions with low Ba concentrations will have a structure more closely dependant on the initial PZT matrix Zr:Ti ratio, which in this case would be rhombohedral. There would coexist both Ba-rich tetragonal PZT and Ba-deficient rhombohedral PZT phases at ambient temperatures (section 8.2.1, Figure 48). As the temperature approaches the apparent T_{r-t} in homogeneous samples, the sample will transition from rhombohedral to tetragonal, as Ba^{2+} ions cause structural instabilities throughout the lattice. This would result in a secondary low temperature ϵ_r peak visible in the ϵ_r vs. temperature plot (section 8.4, Figure 54). The two-phase samples would not show such a peak, as Ba is concentrated in the Ba-rich tetragonal phase stable down to ambient temperature. Any secondary ϵ_r peak present, relating to structural changes of the secondary phase, would not change in temperature with respect to increasing Zr concentration due to the lack of significant interdiffusion, i.e. secondary phase composition remains constant across all two-phase samples irrespective of the starting PZT Zr:Ti ratio.

Processing factors should be taken into consideration when analysing the results of these specimens. Poor particle size control after milling may result in large BT clusters which remain stable during calcination, as only limited diffusion occurs at such temperatures. Large BT clusters would require longer sintering times to allow for adequate interdiffusion to occur. Excess PbO, acting as a transient liquid phase, would enhance mass transport by nature of increased diffusion through liquid phases, consequently promoting interdiffusion in the initial stages of sintering. Once the excess PbO has been expelled, the diffusion rate of Ba^{2+} would substantially decrease, limited to only the number of A-site vacancies present throughout the bulk, i.e. transition to solid-state diffusion. It is important to reaffirm that the primary motive for the inclusion of BT is not to increase piezoelectric properties by nature of doping, rather to provide a suitable substrate to promote epitaxial texture. This means that epitaxy of

textured matrix grains must occur before the dissolution and diffusion of Ba^{2+} into the matrix. Therefore, they may exist a slight trade-off between obtaining complete textured grain epitaxy and overall compositional homogeneity.

8.5 Quasi-static d_{33} measurements of $\text{PZT}_x\text{-5BT}$ ceramics

Quasi-static d_{33} coefficients were obtained for all $\text{PZT}_x\text{-5BT}$ compositions according to the procedure outlined in section 4.5. Measured d_{33} coefficients for both single-phase and $\text{PZT}_x\text{-5BT}$ specimens with compositional variation are shown in Figure 60. Undoped PZT is reported to have a narrow band of increased piezoelectric activity near the MPB⁸⁰. As the starting Zr concentration increases from 52 to 56 mol. % in the $\text{PZT}_x\text{-5BT}$ system, there is a steady increase to a maximum $d_{33} = 453$ pC/N for the $\text{PZT}_{56}\text{-5BT}$ composition (Figure 60a). There is a significant drop in d_{33} coefficient for rhombohedral compositions moving away from the MPB. The same trend in d_{33} can be seen for the inhomogeneous samples, with a maximum $d_{33} = 254$ pC/N (Figure 60b) for the $\text{PZT}_{56}\text{-5BT}$ composition. All observed values are roughly half those seen in the homogeneous data set. The maximum $d_{33} = 453$ pC/N for the homogeneous $\text{PZT}_{56}\text{-5BT}$ composition is significantly greater than reported d_{33} values for undoped PZT ($d_{33} \sim 230$ pC/N) and, comparable with commercial ‘soft’ PZT compositions²²².

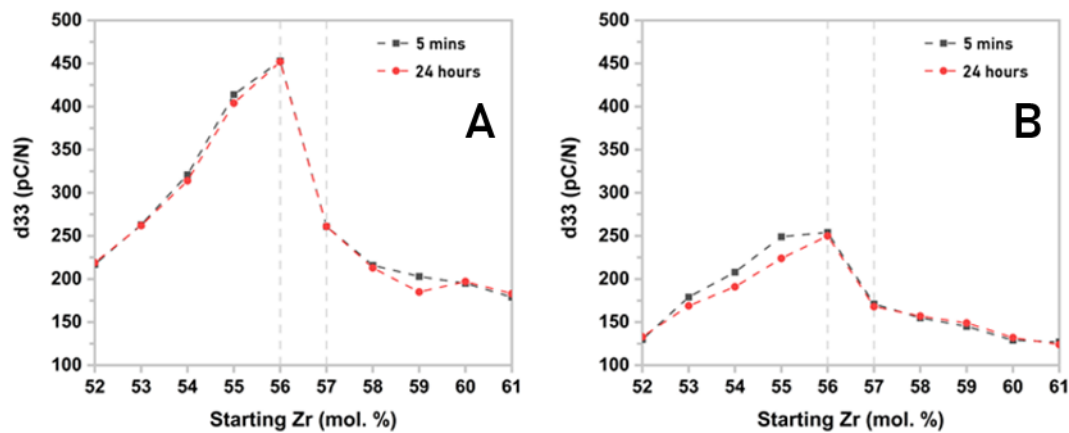


Figure 60 - a) d_{33} vs. starting Zr mol. % concentration for homogeneous $\text{PZT}_x\text{-5BT}$ samples; b) inhomogeneous $\text{PZT}_x\text{-5BT}$ samples.

The samples with phase coexistence are reported previously in section 8.4.1 to result from incomplete interdiffusion between A-site cations during synthesis, giving rise to a tetragonal Ba-rich PZT phase and a tetragonal/rhombohedral Ba-deficient PZT phase, depending on the starting PZT matrix Zr:Ti ratio. The lack of sufficient Ba^{2+} incorporation, suggests that no ‘soft’ character is achieved from the isovalent substitution of Pb^{2+} , rather the formation of $V_{\text{O}}^{\bullet\bullet}$ resulting from PbO loss during sintering, imparts a ‘hardening’ effect reducing any extrinsic d_{33} contributions. The lower polarisability of BT compared to that of PZT indicates that any intrinsic contributions of a secondary Ba-rich PZT phase,

with a composition most likely away from the MPB, on the d_{33} would be lower than conventional undoped PZT, and likely be detrimental to overall materials piezoelectric properties. The converse can be said for the single-phase homogeneous samples. Satisfactory distribution Ba^{2+} throughout the sample ensures that isovalent substitution of Ba^{2+} for Pb^{2+} dominates, resulting in a modest decrease in T_c and an increase in d_{33} by lowering the energy requirements for domain switching, i.e. ‘softening’ effect. The greater compositional homogeneity results in a larger volume fraction of the sample having a composition near the MPB and therefore more piezoelectrically active. To further replicate the d_{33} coefficients obtained and elucidate whether the degree of PbO loss during sintering plays an important part in ensuring satisfactory interdiffusion between Ba^{2+}/Pb^{2+} , a comparison between the addition of 2 wt. % PbO, which is often reported in literature to compensate for PbO loss during sintering, and stoichiometric PZT56-5BT was conducted^{42,43}.

Table 7 - Comparison between d_{33} values for PZT56-5BT samples with varying starting excess PbO.

composition	excess PbO	d_{33} (pC/N)
PZT56-5BT	2 wt. %	266
PZT56-5BT	stoichiometric	438

The d_{33} coefficient for the 2 wt. % PbO sample is markedly lower than that for the starting stoichiometric sample. This result may give reasoning to the hypothesis that slightly Pb-deficient samples, due to PbO loss during synthesis, may result in more homogeneous distributions of Ba^{2+} throughout the matrix and consequently better piezoelectric properties. Due to the differences in ionic sizes of the 12 coordinated A-site cations ($Ba^{2+} \sim 1.61 \text{ \AA}$, $Pb^{2+} \sim 1.49 \text{ \AA}$) and 6-coordinated B-site cations ($Ti^{4+} \sim 0.75 \text{ \AA}$, $Zr^{4+} \sim 0.86 \text{ \AA}$), it is expected that interdiffusion through the bulk can only occur through A-site lattice vacancies. The diffusion of Ba^{2+} into the PZT matrix will therefore be controlled by V_{Pb}'' concentration. As excess PbO acts to compensate for PbO loss, reducing the concentration of V_{Pb}'' and V_O'' , the rate of Ba^{2+} diffusion can be expected to reduce. If starting BT clusters are sufficiently large, the addition of excess PbO may limit complete compositional homogeneity.

Taking a $d_{33} \sim 450 \text{ pC/N}$ as a starting value for the PZT56-5BT composition prior to texturisation, shows huge potential to obtain d_{33} coefficients to compete with other low T_c , relaxor-PT based piezoelectric materials. d_{33} coefficients of textured materials have been reported to increase by a factor of 2²³. Such an enhancement, maintaining high $T_c \sim 340 \text{ }^\circ\text{C}$, would result in combined material properties surpassing current commercially available PZT variants.

8.6 Polarisation/strain hysteresis measurements

P-E and S-E hysteresis loops for the optimum PZTx-5BT composition and PZT-5A1 ceramics were obtained according to the procedure in section 4.5.1. The polarisation and strain as a function of applied electric fields for both PZT56-5BT and PZT-5A1 samples are shown in Figure 61.

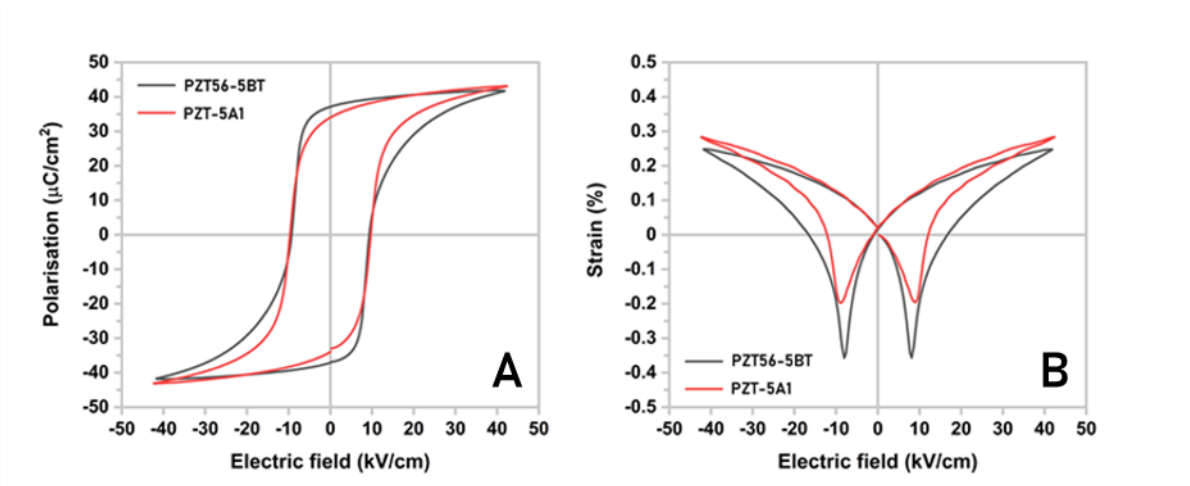


Figure 61 - a) P-E plots for PZT56-5BT and PZT-5A1 ceramics; b) S-E plots.

Both PZT56-5BT and PZT-5A1 exhibit classic squared ferroelectric loops (Figure 61a) and ‘butterfly’ strain loops (Figure 61b). The obtained P_s , P_r , E_c , and S_{max} are summarised in Table 8.

Table 8 - d_{33} , P_s , P_r , E_c , S_{max} , $\tan \delta_{RT}$ values for ceramic PZT56-5BT and PZT-5A1 samples.

composition	d_{33} (pC/N)	P_s ($\mu\text{C}/\text{cm}^2$)	P_r ($\mu\text{C}/\text{cm}^2$)	E_c (kV/cm)	S_{max} (%)	$\tan \delta_{RT}$ (%)
PZT56-5BT	453	41.8	37.1	9.3	0.248	1.5
PZT-5A1	410*	43.1	34.1	9.7	0.284	2*

* reported in technical specifications ref. ²²²

The material coefficients obtained with the addition of 5 vol. % BT show a strong similarity with the ‘soft’ PZT-5A1. Such similar P-E/S-E hysteresis loops between the synthesised PZT56-5BT composition and PZT-5A1, suggests that PZT56-5BT is the optimum final composition for future texturing via TGG, provided the detrimental effects of compositional variation as identified in certain ceramic specimens are avoided.

8.7 PZTx-5BT ceramics results summary

PZT with a starting Zr:Ti ratio of 56:44 has been identified as the optimum matrix composition for future TGG utilising 5 vol. % BT templates, the inclusion of which gives a final bulk composition of $\text{Pb}_{0.947}\text{Ba}_{0.053}\text{Zr}_{0.531}\text{Ti}_{0.469}\text{O}_3$ (PZT56-5BT). The MPB for the PZTx-5BT system lies near starting 56 Zr

mol. %, with PZT56-5BT exhibiting a tetragonal perovskite structure with slight phase coexistence. Plots of ϵ_r vs temperature report a $T_c \sim 340$ °C, approximately ~ 40 °C lower than that of undoped MPB PZT, along with a $\tan \delta_{RT}$ of 1.5 %. Rhombohedral compositions, with > 57 Zr mol. %, exhibit low temperature ϵ_r peaks that rise in temperature with increasing Zr concentration, analogous to the T_{r-t} seen in relaxor-PT based systems. This trend is not seen in specimens with apparent compositional variation. PZT56-5BT shows a maximum quasi-static d_{33} coefficient ~ 450 pC/N, comparable with commercial ‘soft’ PZT variants. $E_c \sim 9.3$ kV/cm and $S_{max} \sim 0.25$ %, values place the optimised PZT56-5BT composition in the Navy Type II (PZT-5) class of piezoelectric material ²²⁴. This ‘soft’ character, reflected in the frequency dielectric loss data for homogenous samples and comparable d_{33} coefficient to PZT-5A1, is believed to originate from the stabilising effect of Ba^{2+} on suppressing oxygen vacancies formation during synthesis ^{220,225}. This compensating effect negates the appearance of ‘hard’ character seen in inhomogeneous samples from poor Ba^{2+} incorporation and subsequent PbO loss, resulting in increased $V_O^{\bullet\bullet}$ concentrations.

Problems originating from unsatisfactory powder processing pre-sintering, resulted in samples with coexisting tetragonal and rhombohedral phases in nominally rhombohedral compositions extending away from the MPB. These samples exhibited a distinct broadening of ϵ_r peaks and a secondary $\tan \delta$ peak ~ 220 °C across all rhombohedral compositions. Compositional inhomogeneity regarding the distribution of BT clusters during synthesis and subsequent lack of interdiffusion between Ba^{2+}/Pb^{2+} cations can explain these findings. ‘Hard’ character originating from uncontrolled $V_O^{\bullet\bullet}$ formation due to PbO loss from the matrix PZT phase, resulted in lowered $\tan \delta_{RT}$ values, lower ϵ_{RT} values, and lower d_{33} coefficients. The secondary Ba-rich phase is noted to most likely have a composition far from the MPB and therefore be detrimental to the overall piezoelectric properties. PbO loss is identified as playing a role in the determining expected piezoelectric properties possibly due to controlling the rate of Ba^{2+} through $V_{Pb}^{\bullet\bullet}$.

Overall, a substantial enhancement of piezoelectric properties has been obtained with the inclusion of 5 vol. % BT and optimisation of the starting PZT composition. Texturisation of this composition via TGG may see an even greater enhancement to piezoelectric properties by exploiting the intrinsic properties in the [00 \bar{l}] direction to compete with other binary/ternary relaxor-PT based piezoelectric materials.

9. Conclusions

The aim of this project was to improve the piezoelectric properties of PZT multilayers by utilising texture in conjunction with compositional modification. The synthesis of suitable perovskite templates, proof of concept in demonstrating [001]-texture formation via TGG in PZT multilayers using suitable templates, and compositional modification, were prior objectives in ultimately achieving significant piezoelectric enhancement in PZT utilising TGG.

The synthesis of anisometric (001) NBT-PT templates via a two-step process consisting of molten flux growth of precursor Aurivillius phase PBT, followed by topochemical conversion was conducted. 1 hour dwell time resulted in the formation of dual phase particles, particles with significant defects, and polycrystalline particles with high mosaicity. Incomplete topochemical conversion had occurred, with particles exhibiting irregular shapes not suitable for TGG. 2 hour dwell time resulted in rectangular, well-faceted single phase particles. Particles had smaller grain sizes ($< 5 \mu\text{m}$) and undergone equiaxed particle growth with reduced aspect ratios. The complex synthesis procedure and difficulty in obtaining satisfactory and reproducible template morphologies, meant commercial platelet BT (Entekno Materials) powder was utilised as an alternative template source.

TGG of [001]-textured PZT multilayers using 5 vol. % (001) BT templates + 5 wt. % PbO was achieved. Rapid heteroepitaxy of textured grains and subsequent coarsening resulted in, $f = 0.91$, after just 6 minutes at $1200 \text{ }^\circ\text{C}$. A maximum, $f = 0.94$, was obtained after sintering for 8 hours. BT templates were not stable within the PZT matrix, with distinct elongated pores seen throughout the fracture surfaces. TGG of [001]-textured PZT-5A1 multilayers using 10 vol. % BT templates was attempted, with a maximum, $f = 0.86$, obtained after sintering for 8 hours. The texture evolution was markedly slower in the commercial PZT-5A1 multilayers. No [001]-texture was seen in samples without excess PbO or samples with micron-sized matrix powder. Matrix particle size, volume liquid phase addition, and template concentration are adjudged to be critical parameters in enabling texture formation via TGG.

A starting Zr:Ti ratio of 56:44 was identified as the optimum matrix composition for TGG utilising 5 vol. % (001) BT templates and deemed from a range of experimental techniques to lie close to the MPB. The effect of BT on ceramic dielectric properties, showed a decrease in $T_c \sim 40 \text{ }^\circ\text{C}$ compared to undoped PZT ($\sim 380 \text{ }^\circ\text{C}$), with PZT56-5BT having a $T_c \sim 340 \text{ }^\circ\text{C}$ and $\tan \delta_{RT}$ of 1.5 %. Zr-rich (compared to the modified MPB), rhombohedral compositions exhibited a low temperature ϵ_r peak dependent on increasing Zr concentration, analogous to the T_{r-t} seen in relaxor-PT based systems. The MPB is believed to curve more sharply towards the PZ end member with respect to temperature. PZT56-5BT showed piezoelectric properties comparable to commercial ‘soft’ PZT-5A1, with $d_{33} \sim 450 \text{ pC/N}$, $E_c \sim 9.3 \text{ kV/cm}$, $S_{max} \sim 0.25 \text{ } \%$. The piezoelectric coefficient reduced by almost half when sintering with PbO excess ($d_{33} = 266 \text{ pC/N}$) and in samples what apparent compositional variation. Coexistence

extending well beyond the MPB in rhombohedral compositions is explained by the lack of Ba^{2+} homogenisation throughout the matrix. PbO loss is identified as aiding in Ba^{2+} diffusion by increasing the concentration of V_{pb}'' throughout the bulk, thereby creating facile diffusion pathways through the cuboctahedral cage of the perovskite structure.

Overall, the proof of concept in synthesising [001]-textured PZT multilayers via TGG has been achieved. Whilst the piezoelectric properties in these textured samples were not optimised, compositional modification of the starting matrix PZT matrix revealed promising piezoelectric properties for near MPB composition, similar to commercial PZT-5A1. The future texturisation of this optimised composition, combining both [001]-texture formation and compositional modification, is expected to result in a significant enhancement in piezoelectric coefficient, satisfying the final aim of this project.

10. Future work

In this work the synthesis of high aspect ratio platelet shaped NBT-PT powder was complex. A trade-off between obtaining small well-faceted single crystal particles with reduced aspect ratio at longer dwell times, and large irregular polycrystalline particles at shorter dwell times, meant alternative materials were explored. Optimising topochemical dwell times during the fabrication process warrants further investigation in achieving more suitable particle morphologies. The incorporation of Zr within starting Aurivillius phase compounds may potentially allow for perovskite template compositions more closely matching the PZT matrix.

The use of BT as a perovskite template material has been successful in texturing PZT multilayers, although it is clear that BT does not remain stable within the PZT matrix during sintering. The temperature at which BT dissolves in PZT should be explored by analysing the fracture surface microstructure at different sintering temperatures. This will enable the formulation of a pre-densification step below the discovered BT dissolution temperature, whereby significant textured grain heteroepitaxy can occur without template dissolution and grain coarsening. EPMA/EDS may be used to detect compositional changes between the template-matrix interface and show the extent of Ba homogenisation within textured samples, complemented by high resolution transmission electron microscopy (TEM) studies to explore local atomic structures.

Dilatometry measurements of textured PZT_x-5BT multilayers with varying PbO additions should be conducted to identify the rate controlling mechanism during initial liquid phase sintering. Whilst a reduction in matrix grain size into the nanometre scale is a critical pre-requisite for successful TGG of PZT, the exact quantity of required liquid phase for texture formation and high final densities is not known. Tailoring the quantity, and even the composition of the liquid phase, may be necessary to ensure sufficient early stage textured grain heteroepitaxy and satisfactory final textured multilayer densities.

Complete texture characterisation using X-ray rocking curves will give more a quantitative and comprehensive insight into textured volume fraction and textured grain alignment of synthesised [001]-textured PZT multilayers. The March-Dollase equation using X-ray rocking curve data can give an orientation distribution function (ODF), with two relevant parameters: f , volume fraction of textured material and, r , degree of orientation of textured material¹⁹¹. r values are known to be sensitive to template alignment during tapecasting, and may initiate investigations into tapecasting parameters, e.g. casting speed, casting height, slurry solids loading²²⁶.

Rayleigh analysis of ceramic PZT_x-5BT samples is needed to separate intrinsic/extrinsic piezoelectric contributions and determine what effect Ba has on irreversible domain wall motion. The effect of Ba on depressing T_c and increasing the intrinsic dominated Berlincourt d_{33} measurements reported in this work, highlights its role in controlling piezoelectric properties. The effect Ba has on domain wall

structure and mobility has been suggested, but not confirmed in this work ⁶⁹. Both contributions are required to provide a reference for future analysis, and to predict the enhanced intrinsic contribution from [001]-textured PZTx-5BT multilayers. Further to this, resonance/antiresonance measurements are required to obtain k_p and Q_m factors in categorising the optimised final PZTx-5BT bulk composition.

Final TGG of [001]-textured PZT56-5BT multilayers should be attempted to obtain samples with optimised final compositions. Full piezoelectric characterisation is required to demonstrate the combined effect of texture and compositional modification on piezoelectric enhancement.

11. References

1. Shirane, G. & Takeda, A. Phase transitions in solid solutions of PbZrO_3 and PbTiO_3 (I) Small concentrations of PbTiO_3 . *J. Phys. Soc. Japan* **7**, 5–11 (1952).
2. Shirane, G., Suzuki, K. & Takeda, A. Phase transitions in solid solutions of PbZrO_3 and PbTiO_3 (II) X-ray study. *J. Phys. Soc. Japan* **7**, 12–18 (1952).
3. Shirane, G. & Suzuki, K. Crystal structure of $\text{Pb}(\text{Zr},\text{Ti})\text{O}_3$. *J. Phys. Soc. Japan* **7**, 333 (1952).
4. Kuwata, J., Uchino, K. & Nomura, S. Phase transitions in the $\text{Pb}(\text{Zn}_{1/3}\text{Nb}_{2/3})\text{O}_3$ - PbTiO_3 system. *Ferroelectrics* **37**, 579–582 (1981).
5. Kuwata, J., Uchino, K. & Nomura, S. Dielectric and piezoelectric properties of $0.91\text{Pb}(\text{Zn}_{1/3}\text{Nb}_{2/3})\text{O}_3$ - 0.09PbTiO_3 single crystals. *Jpn. J. Appl. Phys.* **21**, 1298–1302 (1982).
6. Shrout, T. R., Chang, Z., Kim, N. & Markgraf, S. Dielectric behavior of single crystals near the $(1-x)\text{Pb}(\text{Mg}_{1/3}\text{Nb}_{2/3})\text{O}_3$ - $(x)\text{PbTiO}_3$ morphotropic phase boundary. *Ferroelectr. Lett. Sect.* **12**, 63–69 (1990).
7. Zhang, S. & Li, F. High performance ferroelectric relaxor- PbTiO_3 single crystals: Status and perspective. *J. Appl. Phys.* **111**, 031301 (2012).
8. Zhang, S., Li, F., Luo, J., Sahul, R. & Shrout, T. R. Relaxor- PbTiO_3 single crystals for various applications. *IEEE Trans. Ultrason. Ferroelectr. Freq. Control* **60**, 1572–1580 (2013).
9. Yasuda, N. *et al.* Crystal growth and electrical properties of lead indium niobate-lead titanate binary single crystal. *J. Cryst. Growth* **229**, 299–304 (2001).
10. Hosono, Y., Yamashita, Y., Sakamoto, H. & Ichinose, N. Large piezoelectric constant of high-Curie-temperature $\text{Pb}(\text{In}_{1/2}\text{Nb}_{1/2})\text{O}_3$ - $\text{Pb}(\text{Mg}_{1/3}\text{Nb}_{2/3})\text{O}_3$ - PbTiO_3 ternary single crystal near morphotropic phase boundary. *Jpn. J. Appl. Phys.* **41**, L1240–L1242 (2002).
11. Hosono, Y., Yamashita, Y., Sakamoto, H. & Ichinose, N. Growth of single crystals of high-Curie-temperature $\text{Pb}(\text{In}_{1/2}\text{Nb}_{1/2})\text{O}_3$ - $\text{Pb}(\text{Mg}_{1/3}\text{Nb}_{2/3})\text{O}_3$ - PbTiO_3 ternary systems near morphotropic phase boundary. *Jpn. J. Appl. Phys.* **42**, 5681–5686 (2003).
12. Zhang, S., Lee, S.-M., Kim, D.-H., Lee, H.-Y. & Shrout, T. R. Temperature dependence of the dielectric, piezoelectric, and elastic constants for $\text{Pb}(\text{Mg}_{1/3}\text{Nb}_{2/3})\text{O}_3$ - PbZrO_3 - PbTiO_3 piezocrystals. *J. Appl. Phys.* **102**, 114103 (2007).
13. Zhang, S., Lee, S.-M., Kim, D.-H., Lee, H.-Y. & Shrout, T. R. Electromechanical properties of PMN-PZT piezoelectric single crystals near morphotropic phase boundary compositions. *J. Am.*

- Ceram. Soc.* **90**, 3859–3862 (2007).
14. Zhang, S., Lebrun, L., Randall, C. A. & Shrout, T. R. Growth and electrical properties of (Mn,F) co-doped $0.92\text{Pb}(\text{Zn}_{1/3}\text{Nb}_{2/3})\text{O}_3\text{-}0.08\text{PbTiO}_3$ single crystal. *J. Cryst. Growth* **267**, 204–212 (2004).
 15. Zhang, S., Lee, S.-M., Kim, D.-H., Lee, H.-Y. & Shrout, T. R. Characterization of Mn-modified $\text{Pb}(\text{Mg}_{1/3}\text{Nb}_{2/3})\text{O}_3\text{-PbZrO}_3\text{-PbTiO}_3$ single crystals for high power broad bandwidth transducers. *Appl. Phys. Lett.* **93**, 122908 (2008).
 16. Sherlock, N. P. *et al.* Large signal electromechanical properties of low loss $(1-x)\text{Pb}(\text{Mg}_{1/3}\text{Nb}_{2/3})\text{O}_3\text{-}x\text{PbTiO}_3$ single crystals. *J. Appl. Phys.* **107**, 074108 (2010).
 17. Messing, G. L. *et al.* Texture-engineered ceramics - Property enhancements through crystallographic tailoring. *J. Mater. Res.* **32**, 1–23 (2017).
 18. Han, P., Tian, J. & Yan, W. Bridgman growth and properties of PMN-PT based single crystals. in *Handbook of advanced dielectric, piezoelectric and ferroelectric materials* (ed. Ye, Z.-G.) 3–37 (Woodhead Publishing, 2008).
 19. Lim, L.-C. Flux growth and characterization of PZN-PT and PMN-PT single crystals. in *Handbook of advanced dielectric, piezoelectric and ferroelectric materials* (ed. Ye, Z.-G.) 38–72 (Woodhead Publishing, 2008).
 20. Hackenberger, W. S. *et al.* Recent developments and applications of piezoelectric crystals. in *Handbook of advanced dielectric, piezoelectric and ferroelectric materials* (ed. Ye, Z.-G.) 73–100 (Woodhead Publishing, 2008).
 21. Fushimi, S. & Ikeda, T. Phase equilibrium in the system $\text{PbO-TiO}_2\text{-ZrO}_2$. *J. Am. Ceram. Soc.* **50**, 129–132 (1967).
 22. Luo, J. & Zhang, S. Advances in the growth and characterization of relaxor-PT-based ferroelectric single crystals. *Crystals* **4**, 306–330 (2014).
 23. Messing, G. L. *et al.* Templated grain growth of textured piezoelectric ceramics. *Crit. Rev. Solid State Mater. Sci.* **29**, 45–96 (2004).
 24. Goldschmidt, V. M. *Geochemische Verteilungsgesetze der Elemente. Videnskapsselskaps Skrifter. 1. Math.-naturv. Klasse, 1926, no. 8.* (Kristiania, 1926).
 25. Bhalla, A. S., Guo, R. & Roy, R. The perovskite structure - a review of its role in ceramic science and technology. *Mater. Res. Innov.* **4**, 3–26 (2000).
 26. Wenk, H.-R. & Bulakh, A. *Minerals: Their constitution and origin.* (Cambridge University

- Press, 2004).
27. Galasso, F. S. Structure of perovskite-type compounds. in *Structure, properties, and preparation of perovskite-type compounds* (eds. Smoluchowski, R. & Kurti, N.) 3–49 (Pergamon Press, 1969).
 28. Megaw, H. D. *Crystal structures: A working approach*. (Saunders, 1973).
 29. Glazer, A. M. The classification of tilted octahedra in perovskites. *Acta Crystallogr. Sect. B Struct. Crystallogr. Cryst. Chem.* **B28**, 3384–3392 (1972).
 30. Glazer, A. M. Simple ways of determining perovskite structures. *Acta Crystallogr. Sect. A* **A31**, 756–762 (1975).
 31. Sawaguchi, E. Ferroelectricity versus antiferroelectricity in the solid solutions of PbZrO₃ and PbTiO₃. *J. Phys. Soc. Japan* **8**, 615–629 (1953).
 32. Jaffe, B., Cook, W. R. & Jaffe, H. *Piezoelectric ceramics. Piezoelectric ceramics* (Academic Press, 1971).
 33. Matsuo, Y. & Sasaki, H. Formation of lead zirconate-lead titanate solid solutions. *J. Am. Ceram. Soc.* **48**, 289–291 (1965).
 34. Chandratreya, S. S., Fulrath, R. M. & Pask, J. A. Reaction mechanisms in the formation of PZT solid solutions. *J. Am. Ceram. Soc.* **64**, 422–425 (1981).
 35. Sperti, W. M. Thermal analysis of processes which occur during the calcining of adulterated and unadulterated lead zirconate-lead titanate. (Rutgers University, 1969).
 36. Hankey, D. L. & Biggers, J. V. Solid-state reactions in the system PbO-TiO₂-ZrO₂. *Commun. Am. Ceram. Soc.* **64**, C172–C173 (1981).
 37. Hiremath, B. V., Kingon, A. I. & Biggers, J. V. Reaction sequence in the formation of lead zirconate-lead titanate solid solution: Role of raw materials. *J. Am. Ceram. Soc.* **66**, 790–793 (1983).
 38. Moon, R. L. & Fulrath, R. M. Vaporization and surface phases in the lead zirconate-lead titanate system. *J. Am. Ceram. Soc.* **52**, 565–566 (1969).
 39. Holman, R. L. & Fulrath, R. M. Intrinsic nonstoichiometry in the lead zirconate-lead titanate system determined by Knudsen effusion. *J. Appl. Phys.* **44**, 5227–5236 (1973).
 40. Hardtl, K. H. & Rau, H. PbO vapour pressure in the Pb(Ti_{1-x}Zr_x)O₃ system. *Solid State Commun.* **7**, 41–45 (1969).

41. Kingon, A. I. & Clark, J. B. Sintering of PZT ceramics: I, Atmosphere control. *J. Am. Ceram. Soc.* **66**, 253–256 (1983).
42. Kingon, A. I. & Clark, J. B. Sintering of PZT ceramics: II, Effect of PbO content on densification kinetics. *J. Am. Ceram. Soc.* **66**, 256–260 (1983).
43. Kingon, A. I., Terblanché, P. J. & Clark, J. B. The control of composition, microstructure and properties of Pb(Zr,Ti)O₃ ceramics. *Mater. Sci. Eng.* **71**, 391–397 (1985).
44. Kakegawa, K., Matsunaga, O., Kato, T. & Sasaki, Y. Compositional change and compositional fluctuation in Pb(Zr,Ti)O₃ containing excess PbO. *J. Am. Ceram. Soc.* **78**, 1071–1075 (1995).
45. Northrop, D. A. Vaporization of lead zirconate-lead titanate materials. *J. Am. Ceram. Soc.* **50**, 441–445 (1967).
46. Northrop, D. A. Vaporization of lead zirconate-lead titanate materials: II, Hot-pressed compositions at near theoretical density. *J. Am. Ceram. Soc.* **51**, 357–361 (1968).
47. Webster, A. H., Weston, T. B. & Bright, N. F. H. Effect of PbO deficiency on the piezoelectric properties of lead zirconate-titanate ceramics. *J. Am. Ceram. Soc.* **50**, 490–491 (1967).
48. Atkin, R. B. & Fulrath, R. M. Point defects and sintering of lead zirconate-titanate. *J. Am. Ceram. Soc.* **54**, 265–270 (1971).
49. Ikeda, T. Thermodynamic aspects of electromechanical interaction and piezoelectric relations. in *Fundamentals of piezoelectricity* 5–30 (Oxford University Press, 1990).
50. Kholkin, A. L., Pertsev, N. A. & Goltsev, A. V. Piezoelectricity and crystal symmetry. in *Piezoelectric and acoustic materials for transducer applications* (eds. Safari, A. & Akdoğan, E. K.) 17–38 (Springer, 2008).
51. Newnham, R. E. Piezoelectricity. in *Properties of materials: Anisotropy, symmetry, structure* 87–102 (Oxford University Press, 2005).
52. Damjanovic, D. Piezoelectricity. in *Encyclopedia of condensed matter physics* (eds. Bassani, F., Wyder, P. & Liedl, G. L.) 300–309 (Academic Press, 2005).
53. Li, F., Jin, L., Xu, Z. & Zhang, S. Electrostrictive effect in ferroelectrics: An alternative approach to improve piezoelectricity. *Appl. Phys. Rev.* **1**, 011103 (2014).
54. Newnham, R. E. Nonlinear phenomena. in *Properties of materials: Anisotropy, symmetry, structure* 147–161 (Oxford University Press, 2005).
55. Lines, M. E. & Glass, A. M. Basic concepts. in *Principles and applications of ferroelectrics and related materials* 1–19 (Clarendon Press, 1977).

-
56. Lines, M. E. & Glass, A. M. Domains, imperfections, and polarization reversal. in *Principles and applications of ferroelectrics and related materials* 87–126 (Clarendon Press, 1977).
 57. Arlt, G. Twinning in ferroelectric and ferroelastic ceramics: Stress relief. *J. Mater. Sci.* **25**, 2655–2666 (1990).
 58. Damjanovic, D. Ferroelectric , dielectric and piezoelectric properties of ferroelectric thin films and ceramics. *Reports Prog. Phys.* **61**, 1267–1324 (1998).
 59. Shur, V. Y. Fast polarization reversal process: Evolution of ferroelectric domain structure in thin films. in *Ferroelectric thin films: Synthesis and basic properties* (eds. Araujo, C. A., Scott, J. F. & Taylor, G. W.) 153–192 (Gordon & Breach Science Publishers, 1996).
 60. Arlt, G. & Pertsev, N. A. Force constant and effective mass of 90° domain walls in ferroelectric ceramics. *J. Appl. Phys.* **70**, 2283–2289 (1991).
 61. Cross, L. E. Ferroelectric ceramics: Tailoring properties for specific applications. in *Ferroelectric ceramics* (eds. Setter, N. & Colla, E. L.) 1–85 (Birkhäuser, 1993).
 62. Zhang, Q. M., Pan, W. Y., Jang, S.-J. & Cross, L. E. Domain wall excitations and their contributions to the weak-signal response of doped lead zirconate titanate ceramics. *J. Appl. Phys.* **64**, 6445–6451 (1988).
 63. Zhang, Q. M., Wang, H., Kim, N. & Cross, L. E. Direct evaluation of domain-wall and intrinsic contributions to the dielectric and piezoelectric response and their temperature dependence on lead zirconate-titanate ceramics. *J. Appl. Phys.* **75**, 454–459 (1994).
 64. Takahashi, S. Effects of impurity doping in lead zirconate-titanate ceramics. *Ferroelectrics* **41**, 143–156 (1982).
 65. Carl, K. & Hardtl, K. H. Electrical after-effects in Pb(Ti,Zr)O₃ ceramics. *Ferroelectrics* **17**, 473–486 (1977).
 66. Warren, W. L. *et al.* Defect-dipole alignment and tetragonal strain in ferroelectrics. *J. Appl. Phys.* **79**, 9250–9257 (1996).
 67. Lambeck, P. V. & Jonker, G. H. Ferroelectric domain stabilization in BaTiO₃ by bulk ordering of defects. *Ferroelectrics* **22**, 729–731 (1978).
 68. Arlt, G. & Neumann, H. Internal bias in ferroelectric ceramics: Origin and time dependence. *Ferroelectrics* **87**, 109–120 (1988).
 69. Zheng, H., Reaney, I. M., Lee, W. E., Jones, N. & Thomas, H. Effects of octahedral tilting on the piezoelectric properties of strontium/barium/niobium-doped soft lead zirconate titanate

- ceramics. *J. Am. Ceram. Soc.* **85**, 2337–2344 (2002).
70. Devonshire, A. F. XCVI. Theory of barium titanate - Part I. *Philos. Mag. Ser. 7* **40**, 1040–1063 (1949).
71. Devonshire, A. F. CIX. Theory of barium titanate - Part II. *Philos. Mag. Ser. 7* **42**, 1065–1079 (1951).
72. Haun, M. J., Furman, E., Jang, S.-J. & Cross, L. E. Thermodynamic theory of the lead zirconate-titanate solid solution system, part I: Phenomenology. *Ferroelectrics* **99**, 13–25 (1989).
73. Zhuang, Z. Q., Jang, S.-J., Cross, L. E. & Haun, M. J. Composition and temperature dependence of the dielectric, piezoelectric and elastic properties of pure PZT ceramics. *IEEE Trans. Ultrason. Ferroelectr. Freq. Control* **36**, 413–416 (1989).
74. Zhang, X. L., Chen, Z. X., Cross, L. E. & Schulze, W. A. Dielectric and piezoelectric properties of modified lead titanate zirconate ceramics from 4.2 to 300 K. *J. Mater. Sci.* **18**, 968–972 (1983).
75. Rayleigh, L. XXV. Notes on electricity and magnetism.-III. On the behaviour of iron and steel under the operation of feeble magnetic forces. *Philos. Mag. Ser. 5* **23**, 225–245 (1887).
76. Damjanovic, D. & Demartin, M. The Rayleigh law in piezoelectric ceramics. *J. Phys. D. Appl. Phys.* **29**, 2057–2060 (1996).
77. Damjanovic, D. Stress and frequency dependence of the direct piezoelectric effect in ferroelectric ceramics. *J. Appl. Phys.* **82**, 1788–1797 (1997).
78. Reaney, I. M. & Damjanovic, D. Crystal structure and domain-wall contributions to the piezoelectric properties of strontium bismuth titanate ceramics. *J. Appl. Phys.* **80**, 4223–4225 (1996).
79. Damjanovic, D. & Demartin, M. Contribution of the irreversible displacement of domain walls to the piezoelectric effect in barium titanate and lead zirconate titanate ceramics. *J. Phys. Condens. Matter* **9**, 4943–4953 (1997).
80. Mishra, S. K., Pandey, D. & Singh, A. P. Effect of phase coexistence at morphotropic phase boundary on the properties of $\text{Pb}(\text{Zr}_x\text{Ti}_{1-x})\text{O}_3$ ceramics. *Appl. Phys. Lett.* **69**, 1707–1709 (1996).
81. Park, S.-E. & Shrout, T. R. Ultrahigh strain and piezoelectric behavior in relaxor based ferroelectric single crystals. *J. Appl. Phys.* **82**, 1804–1811 (1997).
82. Park, S.-E. & Shrout, T. R. Characteristics of relaxor-based piezoelectric single crystals for

- ultrasonic transducers. *IEEE Trans. Ultrason. Ferroelectr. Freq. Control* **44**, 1140–1147 (1997).
83. Park, S.-E. & Shrout, T. R. Relaxor based ferroelectric single crystals for electro-mechanical actuators. *Mater. Res. Innov.* **1**, 20–25 (1997).
84. Durbin, M. K., Jacobs, E. W., Hicks, J. C. & Park, S.-E. In situ x-ray diffraction study of an electric field induced phase transition in the single crystal relaxor ferroelectric, 92%Pb(Zn_{1/3}Nb_{2/3})O₃-8%PbTiO₃. *Appl. Phys. Lett.* **74**, 2848–2850 (1999).
85. Wada, S., Park, S.-E., Cross, L. E. & Shrout, T. R. Domain configuration and ferroelectric related properties of relaxor based single crystals. *J. Korean Phys. Soc.* **32**, 1290–1293 (1998).
86. Du, X. H., Belegundu, U. & Uchino, K. Crystal orientation dependence of piezoelectric properties in lead zirconate titanate: Theoretical expectation for thin films. *Jpn. J. Appl. Phys.* **36**, 5580–5587 (1997).
87. Du, X. H., Zheng, J., Belegundu, U. & Uchino, K. Crystal orientation dependence of piezoelectric properties of lead zirconate titanate near the morphotropic phase boundary. *Appl. Phys. Lett.* **72**, 2421–2423 (1998).
88. Haun, M. J., Furman, E., Jang, S.-J. & Cross, L. E. Thermodynamic theory of the lead zirconate-titanate solid solution system, part V: Theoretical calculations. *Ferroelectrics* **99**, 63–86 (1989).
89. Fu, H. & Cohen, R. E. Polarization rotation mechanism for ultrahigh electromechanical response in single-crystal piezoelectrics. *Nature* **403**, 281–283 (2000).
90. Fu, H. & Cohen, R. E. Piezoelectric response from rotating polarization. in *Fundamental physics of ferroelectrics 2000: Aspen center for physics winter workshop* (eds. Cohen, R. E. & Mewaldt, R. A.) 143–150 (AIP Conference Proceedings, 2000).
91. Davis, M., Budimir, M., Damjanovic, D. & Setter, N. Rotator and extender ferroelectrics: Importance of the shear coefficient to the piezoelectric properties of domain-engineered crystals and ceramics. *J. Appl. Phys.* **101**, 054112 (2007).
92. Damjanovic, D. Comments on origins of enhanced piezoelectric properties in ferroelectrics. *IEEE Trans. Ultrason. Ferroelectr. Freq. Control* **56**, 1574–1585 (2009).
93. Sundar, V. & Newnham, R. E. Electrostriction and polarization. *Ferroelectrics* **135**, 431–446 (1992).
94. Ishibashi, Y. & Iwata, M. Morphotropic phase boundary in solid solution systems of perovskite-type oxide ferroelectrics. *Jpn. J. Appl. Phys.* **37**, L985–L987 (1998).
95. Ishibashi, Y. & Iwata, M. Phenomenology of magnetostrictive alloys of the rare-earth Fe₂

- compound family. I. Elastic constants. *J. Phys. Soc. Japan* **68**, 1353–1356 (1999).
96. Ishibashi, Y. & Iwata, M. A theory of morphotropic phase boundary in solid-solution systems of perovskite-type oxide ferroelectrics. *Jpn. J. Appl. Phys.* **38**, 800–804 (1999).
97. Ishibashi, Y. & Iwata, M. Theory of morphotropic phase boundary in solid-solution systems of perovskite-type oxide ferroelectrics: Elastic properties. *Jpn. J. Appl. Phys.* **38**, 1454–1458 (1999).
98. Iwata, M. & Ishibashi, Y. Theory of morphotropic phase boundary in solid solution systems of perovskite-type oxide ferroelectrics: p-e hysteresis loop. *Jpn. J. Appl. Phys.* **38**, 5670–5673 (1999).
99. Iwata, M. & Ishibashi, Y. Theory of morphotropic phase boundary in solid solution systems of perovskite-type oxide ferroelectrics: engineered domain configurations. *Jpn. J. Appl. Phys.* **39**, 5156–5163 (2000).
100. Ishibashi, Y. Theory of the morphotropic phase boundary. *Ferroelectrics* **264**, 197–206 (2001).
101. Damjanovic, D., Brem, F. & Setter, N. Crystal orientation dependence of the piezoelectric d₃₃ coefficient in tetragonal BaTiO₃ as a function of temperature. *Appl. Phys. Lett.* **80**, 652–654 (2002).
102. Budimir, M., Damjanovic, D. & Setter, N. Piezoelectric anisotropy-phase transition relations in perovskite single crystals. *J. Appl. Phys.* **94**, 6753–6761 (2003).
103. Damjanovic, D. Contributions to the piezoelectric effect in ferroelectric single crystals and ceramics. *J. Am. Ceram. Soc.* **88**, 2663–2676 (2005).
104. Budimir, M., Damjanovic, D. & Setter, N. Piezoelectric response and free-energy instability in the perovskite crystals BaTiO₃, PbTiO₃, and Pb(Zr,Ti)O₃. *Phys. Rev. B - Condens. Matter Mater. Phys.* **73**, 174106 (2006).
105. Damjanovic, D., Budimir, M., Davis, M. & Setter, N. Piezoelectric anisotropy: Enhanced piezoelectric response along nonpolar directions in perovskite crystals. *J. Mater. Sci.* **41**, 65–76 (2006).
106. Zhang, S. *et al.* Field stability of piezoelectric shear properties in PIN-PMN-PT crystals under large drive field. *IEEE Trans. Ultrason. Ferroelectr. Freq. Control* **58**, 274–280 (2011).
107. Wu, Z. & Cohen, R. E. Pressure-induced anomalous phase transitions and colossal enhancement of piezoelectricity in PbTiO₃. *Phys. Rev. Lett.* **95**, 037601 (2005).
108. Ahart, M. *et al.* Origin of morphotropic phase boundaries in ferroelectrics. *Nature* **451**, 545–548

- (2008).
109. Ganesh, P. & Cohen, R. E. Finite electric-field study of pressure effects on polarization rotation in PbTiO₃. in *Materials Research Society Symposium F – Multiferroic and ferroelectric materials* (eds. Gruverman, A., Fennie, C. J., Kunishima, I., Noheda, B. & Noh, T. W.) 1199-F11-06 (Cambridge University Press, 2010).
 110. Damjanovic, D. A morphotropic phase boundary system based on polarization rotation and polarization extension. *Appl. Phys. Lett.* **97**, 062906 (2010).
 111. Lee, S.-G. *et al.* Growth and electrostrictive properties of Pb(Mg_{1/3}Nb_{2/3})O₃ crystals. *Appl. Phys. Lett.* **74**, 1030–1032 (1999).
 112. Zawilski, K. T. *et al.* Segregation during the vertical Bridgman growth of lead magnesium niobate-lead titanate single crystals. *J. Cryst. Growth* **258**, 353–367 (2003).
 113. Noheda, B. *et al.* A monoclinic ferroelectric phase in the Pb(Zr_{1-x}Ti_x)O₃ solid solution. *Appl. Phys. Lett.* **74**, 2059–2061 (1999).
 114. Noheda, B. Structure and high-piezoelectricity in lead oxide solid solutions. *Curr. Opin. Solid State Mater. Sci.* **6**, 27–34 (2002).
 115. Corker, D. L., Glazer, A. M., Whatmore, R. W., Stallard, A. & Fauth, F. A neutron diffraction investigation into the rhombohedral phases of the perovskite series PbZr_{1-x}Ti_xO₃. *J. Phys. Condens. Matter* **10**, 6251–6269 (1998).
 116. Noheda, B. *et al.* Tetragonal-to-monoclinic phase transition in a ferroelectric perovskite: The structure of PbZr_{0.52}Ti_{0.48}O₃. *Phys. Rev. B - Condens. Matter Mater. Phys.* **61**, 8687–8695 (2000).
 117. Guo, R. *et al.* Origin of the high piezoelectric response in PbZr_{1-x}Ti_xO₃. *Phys. Rev. Lett.* **84**, 5423–5426 (2000).
 118. Hall, D. A., Steuwer, A., Cherdhirunkorn, B., Mori, T. & Withers, P. J. A high energy synchrotron x-ray study of crystallographic texture and lattice strain in soft lead zirconate titanate ceramics. *J. Appl. Phys.* **96**, 4245–4252 (2004).
 119. Bellaïche, L., García, A. & Vanderbilt, D. Finite-temperature properties of Pb(Zr_{1-x}Ti_x)O₃ alloys from first principles. *Phys. Rev. Lett.* **84**, 5427–5430 (2000).
 120. Bellaïche, L., García, A. & Vanderbilt, D. Electric-field induced polarization paths in Pb(Zr_{1-x}Ti_x)O₃ alloys. *Phys. Rev. B - Condens. Matter Mater. Phys.* **64**, 60103 (2001).
 121. Noheda, B. & Cox, D. E. Bridging phases at the morphotropic boundaries of lead oxide solid

- solutions. *Phase Transitions* **79**, 5–20 (2006).
122. Vanderbilt, D. & Cohen, M. H. Monoclinic and triclinic phases in higher-order Devonshire theory. *Phys. Rev. B - Condens. Matter Mater. Phys.* **63**, 094108 (2001).
123. Iwata, M. & Ishibashi, Y. Phenomenological theory of morphotropic phase boundary with monoclinic phase in solid-solution systems of perovskite-type oxide ferroelectrics. *Jpn. J. Appl. Phys.* **44**, 3095–3098 (2005).
124. Cox, D. E. *et al.* Universal phase diagram for high-piezoelectric perovskite systems. *Appl. Phys. Lett.* **79**, 400–402 (2001).
125. Ye, Z.-G., Noheda, B., Dong, M., Cox, D. E. & Shirane, G. Monoclinic phase in the relaxor-based piezoelectric/ferroelectric $\text{Pb}(\text{Mg}_{1/3}\text{Nb}_{2/3})\text{O}_3\text{-PbTiO}_3$ system. *Phys. Rev. B - Condens. Matter Mater. Phys.* **64**, 184114 (2001).
126. Bai, F. *et al.* X-ray and neutron diffraction investigations of the structural phase transformation sequence under electric field in $0.7\text{Pb}(\text{Mg}_{1/3}\text{Nb}_{2/3})\text{-}0.3\text{PbTiO}_3$ crystal. *J. Appl. Phys.* **96**, 1620–1627 (2004).
127. Noheda, B. *et al.* Electric-field-induced phase transitions in rhombohedral $\text{Pb}(\text{Zn}_{1/3}\text{Nb}_{2/3})_{1-x}\text{TixO}_3$. *Phys. Rev. B - Condens. Matter Mater. Phys.* **65**, 2241011 (2002).
128. Noheda, B. *et al.* Polarization rotation via a monoclinic phase in the piezoelectric $92\%\text{PbZn}_{1/3}\text{Nb}_{2/3}\text{O}_3\text{-}8\%\text{PbTiO}_3$. *Phys. Rev. Lett.* **86**, 3891–3894 (2001).
129. Davis, M., Damjanovic, D. & Setter, N. Electric-field-induced orthorhombic to rhombohedral phase transition in $[111]_c$ -oriented $0.92\text{Pb}(\text{Zn}_{1/3}\text{Nb}_{2/3})\text{O}_3\text{-}0.08\text{PbTiO}_3$. *J. Appl. Phys.* **97**, 064101 (2005).
130. Davis, M., Damjanovic, D. & Setter, N. Electric-field-, temperature-, and stress-induced phase transitions in relaxor ferroelectric single crystals. *Phys. Rev. B - Condens. Matter Mater. Phys.* **73**, 014115 (2006).
131. Choi, S. W., Shrout, T. R., Jang, S.-J. & Bhalla, A. S. Dielectric and pyroelectric properties in the $\text{Pb}(\text{Mg}_{1/3}\text{Nb}_{2/3})\text{O}_3\text{-PbTiO}_3$ system. *Ferroelectrics* **100**, 29–38 (1989).
132. Kisi, E. H., Piltz, R. O., Forrester, J. S. & Howard, C. J. The giant piezoelectric effect: Electric field induced monoclinic phase or piezoelectric distortion of the rhombohedral parent? *J. Phys. Condens. Matter* **15**, 3631–3640 (2003).
133. Glazer, A. M., Thomas, P. A., Baba-Kishi, K. Z., Pang, G. K. H. & Tai, C. W. Influence of short-range and long-range order on the evolution of the morphotropic phase boundary in $\text{Pb}(\text{Zr}_{1-x}\text{Tix})\text{O}_3$. *Phys. Rev. B - Condens. Matter Mater. Phys.* **70**, 184123 (2004).

-
134. Zhang, N. *et al.* The missing boundary in the phase diagram of $\text{PbZr}_{1-x}\text{Ti}_x\text{O}_3$. *Nat. Commun.* **5**, 1–9 (2014).
135. Viehland, D. Symmetry-adaptive ferroelectric mesostates in oriented $\text{Pb}(\text{BI}_{1/3}\text{BII}_{2/3})\text{O}_3$ - PbTiO_3 crystals. *J. Appl. Phys.* **88**, 4794–4806 (2000).
136. Jin, Y. M., Wang, Y. U., Khachatryan, A. G., Li, J. F. & Viehland, D. Adaptive ferroelectric states in systems with low domain wall energy: Tetragonal microdomains. *J. Appl. Phys.* **94**, 3629–3640 (2003).
137. Wada, S. *et al.* Enhanced piezoelectric property of barium titanate single crystals with engineered domain configurations. *Jpn. J. Appl. Phys.* **38**, 5505–5511 (1999).
138. Wada, S., Kakemoto, H. & Tsurumi, T. Enhanced piezoelectric properties of piezoelectric single crystals by domain engineering. *Mater. Trans.* **45**, 178–187 (2004).
139. Jin, Y. M., Wang, Y. U., Khachatryan, A. G., Li, J. F. & Viehland, D. Conformal miniaturization of domains with low domain-wall energy: Monoclinic ferroelectric states near the morphotropic phase boundaries. *Phys. Rev. Lett.* **91**, 197601 (2003).
140. Wang, Y. U. Diffraction theory of nanotwin superlattices with low symmetry phase. *Phys. Rev. B - Condens. Matter Mater. Phys.* **74**, 104109 (2006).
141. Wang, Y. U. Diffraction theory of nanotwin superlattices with low symmetry phase: Application to rhombohedral nanotwins and monoclinic M_a and M_b phases. *Phys. Rev. B - Condens. Matter Mater. Phys.* **76**, 024108 (2007).
142. Yin, J. & Cao, W. Observation and analysis of domain configurations in domain engineered PZN-PT single crystals. *Ferroelectrics* **251**, 93–100 (2001).
143. Ishibashi, Y. & Salje, E. Theoretical consideration on the 90° domain walls in tetragonal ferroelectrics. *Ferroelectrics* **303**, 9–13 (2004).
144. Erhart, J. & Cao, W. Effective material properties in twinned ferroelectric crystals. *J. Appl. Phys.* **86**, 1073–1081 (1999).
145. Erhart, J. & Cao, W. Effective symmetry and physical properties of twinned perovskite ferroelectric single crystals. *J. Mater. Res.* **16**, 570–577 (2001).
146. Yin, J. & Cao, W. Effective macroscopic symmetries and materials properties of multidomain $0.955\text{Pb}(\text{Zn}_{1/3}\text{Nb}_{2/3})\text{O}_3$ - 0.045PbTiO_3 single crystals. *J. Appl. Phys.* **92**, 444–448 (2002).
147. Han, J. & Cao, W. Interweaving domain configurations in $[001]$ -poled rhombohedral phase $0.68\text{Pb}(\text{Mg}_{1/3}\text{Nb}_{2/3})\text{O}_3$ - 0.32PbTiO_3 single crystals. *Appl. Phys. Lett.* **83**, 2040–2042 (2003).

148. Woodward, D. I., Knudsen, J. & Reaney, I. M. Review of crystal and domain structures in the $\text{PbZr}_x\text{Ti}_{1-x}\text{O}_3$ solid solution. *Phys. Rev. B - Condens. Matter Mater. Phys.* **72**, 104110 (2005).
149. Reaney, I. M. Octahedral tilting, domain structure and piezoelectricity in perovskites and related ceramics. *J. Electroceramics* **19**, 1–8 (2007).
150. Cordero, F. Elastic properties and enhanced piezoelectric response at morphotropic phase boundaries. *Materials (Basel)*. **8**, 8195–8245 (2015).
151. Sato, Y., Hirayama, T. & Ikuhara, Y. Monoclinic nanodomains in morphotropic phase boundary $\text{Pb}(\text{Mg}_{1/3}\text{Nb}_{2/3})\text{O}_3$ - PbTiO_3 . *Appl. Phys. Lett.* **104**, (2014).
152. Suvaci, E., Oh, K. S. & Messing, G. L. Kinetics of template growth in alumina during the process of templated grain growth (TGG). *Acta Mater.* **49**, 2075–2081 (2001).
153. Suvaci, E. & Messing, G. L. Critical factors in the templated grain growth of textured reaction-bonded alumina. *J. Am. Ceram. Soc.* **83**, 2041–2048 (2000).
154. Seabaugh, M. M., Messing, G. L. & Vaudin, M. D. Texture development and microstructure evolution in liquid-phase-sintered α -alumina ceramics prepared by templated grain growth. *J. Am. Ceram. Soc.* **83**, 3109–3116 (2000).
155. Rahaman, M. N. Liquid-phase sintering. in *Ceramic processing and sintering* 620–687 (CRC Press, 2003).
156. Moriana, A. D. & Zhang, S. Lead-free textured piezoceramics using tape casting: A review. *J. Mater.* **4**, 277–303 (2018).
157. Sabolsky, E. M., Trolier-McKinstry, S. & Messing, G. L. Dielectric and piezoelectric properties of $\langle 001 \rangle$ fiber-textured $0.675\text{Pb}(\text{Mg}_{1/3}\text{Nb}_{2/3})\text{O}_3$ - 0.32PbTiO_3 ceramics. *J. Appl. Phys.* **93**, 4072–4080 (2003).
158. Kwon, S., Sabolsky, E. M., Messing, G. L. & Trolier-McKinstry, S. High strain, $\langle 001 \rangle$ textured $0.675\text{Pb}(\text{Mg}_{1/3}\text{Nb}_{2/3})\text{O}_3$ - 0.325PbTiO_3 ceramics: Templated grain growth and piezoelectric properties. *J. Am. Ceram. Soc.* **88**, 312–317 (2005).
159. Richter, T., Denneler, S., Schuh, C., Suvaci, E. & Moos, R. Textured PMN-PT and PMN-PZT. *J. Am. Ceram. Soc.* **91**, 929–933 (2008).
160. Poterala, S. F., Trolier-Mckinstry, S., Meyer, R. J. & Messing, G. L. Processing, texture quality, and piezoelectric properties of $\langle 001 \rangle$ textured $(1-x)\text{Pb}(\text{Mg}_{1/3}\text{Nb}_{2/3})\text{TiO}_3$ - $x\text{PbTiO}_3$ ceramics. *J. Appl. Phys.* **110**, 014105 (2011).
161. Yan, Y., Wang, Y. U. & Priya, S. Electromechanical behavior of $[001]$ -textured

- Pb(Mg_{1/3}Nb_{2/3})O₃-PbTiO₃ ceramics. *Appl. Phys. Lett.* **100**, 192905 (2012).
162. Yan, Y. *et al.* Giant energy density in [001]-textured Pb(Mg_{1/3}Nb_{2/3})O₃-PbZrO₃-PbTiO₃ piezoelectric ceramics. *Appl. Phys. Lett.* **102**, 042903 (2013).
163. Yan, Y., Cho, K.-H. & Priya, S. Piezoelectric properties and temperature stability of Mn-doped Pb(Mg_{1/3}Nb_{2/3})-PbZrO₃-PbTiO₃ textured ceramics. *Appl. Phys. Lett.* **100**, 132908 (2012).
164. Chang, Y. *et al.* Enhanced electromechanical properties and phase transition temperatures in [001] textured Pb(In_{1/2}Nb_{1/2})O₃-Pb(Mg_{1/3}Nb_{2/3})O₃-PbTiO₃ ternary ceramics. *Appl. Phys. Lett.* **107**, 082902 (2015).
165. Wei, D. D., Yuan, Q. B., Zhang, G. Q. & Wang, H. Templated grain growth and piezoelectric properties of <001>-textured PIN-PMN-PT ceramics. *J. Mater. Res.* **30**, 2144–2150 (2015).
166. Watson, B. H., Brova, M. J., Fanton, M. A., Meyer, R. J. & Messing, G. L. Textured Mn-doped PIN-PMN-PT ceramics: Harnessing intrinsic piezoelectricity for high-power transducer applications. *J. Eur. Ceram. Soc.* **41**, 1270–1279 (2021).
167. Duran, C., Dursun, S. & Akça, E. High strain, <001>-textured Pb(Mg_{1/3}Nb_{2/3})O₃-Pb(Yb_{1/2}Nb_{1/2})O₃-PbTiO₃ piezoelectric ceramics. *Scr. Mater.* **113**, 14–17 (2016).
168. Brova, M. J. *et al.* Templated grain growth of high coercive field CuO-doped textured PYN-PMN-PT ceramics. *J. Am. Ceram. Soc.* **103**, 6149–6156 (2020).
169. Seabaugh, M. M., Kerscht, I. H. & Messing, G. L. Texture development by templated grain growth in liquid-phase-sintered α -alumina. *J. Am. Ceram. Soc.* **80**, 1181–1188 (1997).
170. Arendt, R. H., Rosolowski, J. H. & Szymaszek, J. W. Lead zirconate titanate ceramics from molten salt solvent synthesized powders. *Mater. Res. Bull.* **147**, 703–709 (1979).
171. Arendt, R. H. & Pasco, W. D. The molten salt synthesis of large crystal-sized SrTiO₃. *J. Electrochem. Soc.* **134**, 733–736 (1987).
172. Bishop, A. C. *An outline of crystal morphology*. (Hutchinson Scientific and Technical, 1967).
173. Ma, S., Fuh, J. Y. H., Zhang, Y. F. & Lu, L. Synthesis of anisotropic lead titanate powders for templated grain growth of textured piezoelectric ceramics. *Surf. Rev. Lett.* **17**, 159–164 (2010).
174. Ito, Y., Jadidian, B., Allahverdi, M. & Safari, A. Particle-shape control of molten salt synthesized lead titanate. in *IEEE International Symposium on Applications of Ferroelectrics* vol. 1 389–392 (IEEE, 2000).
175. Moon, J., Carasso, M. L., Krarup, H. G., Kerchner, J. A. & Adair, J. H. Particle-shape control and formation mechanisms of hydrothermally derived lead titanate. *J. Mater. Res.* **14**, 866–875

- (1999).
176. Takeuchi, T., Tani, T. & Satoh, T. Microcomposite particles Sr₃Ti₂O₇-SrTiO₃ with an epitaxial core-shell structure. *Solid State Ionics* **108**, 67–71 (1998).
177. Takeuchi, T. & Tani, T. Synthesis of Bi₄Ti₃O₁₂-PbTiO₃ micro-composite particles. *J. Ceram. Soc. Japan* **106**, 947–950 (1998).
178. Watari, K., Brahmaroutu, B., Messing, G. L., Trolrier-McKinstry, S. & Cheng, S.-C. Epitaxial growth of anisotropically shaped, single-crystal particles of cubic SrTiO₃. *J. Mater. Res.* **15**, 846–849 (2000).
179. Saito, Y. *et al.* Lead-free piezoceramics. *Nature* **432**, 84–87 (2004).
180. Saito, Y. & Takao, H. Synthesis of platelike {100} SrTiO₃ particles by topochemical microcrystal conversion and fabrication of grain-oriented ceramics. *Jpn. J. Appl. Phys.* **45**, 7377–7381 (2006).
181. Yan, Y., Liu, D., Zhao, W., Zhou, H. & Fang, H. Topochemical synthesis of a high-aspect-ratio platelet NaNbO₃ template. *J. Am. Ceram. Soc.* **90**, 2399–2403 (2007).
182. Liu, D., Yan, Y. & Zhou, H. Synthesis of micron-scale platelet BaTiO₃. *J. Am. Ceram. Soc.* **90**, 1323–1326 (2007).
183. Sato, T., Yoshida, Y. & Kimura, T. Preparation of <110>-textured BaTiO₃ ceramics by the reactive-templated grain growth method using needlelike TiO₂ particles. *J. Am. Ceram. Soc.* **90**, 3005–3008 (2007).
184. Sato, T. & Kimura, T. Preparation of <111>-textured BaTiO₃ ceramics by templated grain growth method using novel template particles. *Ceram. Int.* **34**, 757–760 (2008).
185. Poterala, S. F., Chang, Y., Clark, T., Meyer, R. J. & Messing, G. L. Mechanistic interpretation of the Aurivillius to perovskite topochemical microcrystal conversion process. *Chem. Mater.* **22**, 2061–2068 (2010).
186. Poterala, S. F., Meyer, R. J. & Messing, G. L. Synthesis of high aspect ratio PbBi₄Ti₄O₁₅ and topochemical conversion to PbTiO₃-based microplatelets. *J. Am. Ceram. Soc.* **94**, 2323–2329 (2011).
187. Pérez, J. A. *et al.* Growth of lead zirconate titanate single crystals by the high temperature solution method. *Mater. Sci. Forum* **514–516**, 184–187 (2006).
188. Muramatsu, H. & Kimura, T. Preparation of bulk Pb(Zr,Ti)O₃ with crystallographic texture by templated grain growth method. *J. Electroceramics* **13**, 531–535 (2004).

-
189. Miwa, Y. *et al.* Processing and enhanced piezoelectric properties of highly oriented compositionally modified Pb(Zr,Ti)O₃ ceramics fabricated by magnetic alignment. *Appl. Phys. Express* **8**, 041501 (2015).
190. Lotgering, F. K. Topotactical reactions with ferrimagnetic oxides having hexagonal crystal structures-I. *J. Inorg. Nucl. Chem.* **9**, 113–123 (1959).
191. Seabaugh, M. M., Vaudin, M. D., Cline, J. P. & Messing, G. L. Comparison of texture analysis techniques for highly oriented α -Al₂O₃. *J. Am. Ceram. Soc.* **83**, 2049–2054 (2000).
192. Boultif, A. & Louër, D. Powder pattern indexing with the dichotomy method. *J. Appl. Crystallogr.* **37**, 724–731 (2004).
193. ASTM-E112. *Standard test methods for determining average grain size.* (2013).
194. Tellier, J., Boullay, P. & Mercurio, D. Crystal structure of the Aurivillius phases in the system Bi₄Ti₃O₁₂-PbTiO₃. *Zeitschrift fur Krist.* **222**, 234–243 (2007).
195. Smazhevskaya, E. G. *et al.* The systems PbTiO₃-(K_{0.5}Bi_{0.5})TiO₃ and PbTiO₃-(Na_{0.5}Bi_{0.5})TiO₃. *Inorg. Mater.* **2**, 1597 (1966).
196. Foo, C. *Private Communication.* (2015).
197. Joseph, J., Vimala, T. M., Sivasubramanian, V. & Murthy, V. R. K. Structural investigations on Pb(Zr_xTi_{1-x})O₃ solid solutions using the X-ray Rietveld method. *J. Mater. Sci.* **35**, 1571–1575 (2000).
198. Chang, Y. *et al.* Formation mechanism of highly [001]_c textured Pb(In_{1/2}Nb_{1/2})O₃-Pb(Mg_{1/3}Nb_{2/3})O₃-PbTiO₃ relaxor ferroelectric ceramics with giant piezoelectricity. *J. Eur. Ceram. Soc.* **36**, 1973–1981 (2016).
199. Smith, C. S. Grains, phases, and interfaces: An interpretation of microstructure. *Metall. Mater. Trans. A Phys. Metall. Mater. Sci.* **41A**, 1063–1100 (1948).
200. Rahaman, M. N. Grain growth and microstructure control. in *Ceramic processing and sintering* 540–619 (CRC Press, 2003).
201. Kimura, T. Application of texture engineering to piezoelectric ceramics. *J. Ceram. Soc. Japan* **114**, 15–25 (2006).
202. Kang, S.-J. Basis of liquid phase sintering. in *Sintering - densification, grain growth, and microstructure* 199–203 (Butterworth-Heinemann, 2005).
203. Hennings, D. F. K., Janssen, R. & Reynen, P. J. L. Control of liquid-phase-enhanced discontinuous grain growth in barium titanate. *J. Am. Ceram. Soc.* **70**, 23–27 (1987).

-
204. Sabolsky, E. M., Messing, G. L. & Trolier-McKinstry, S. Kinetics of templated grain growth of $0.65(\text{Mg}_{1/3}\text{Nb}_{2/3})\text{O}_3\text{-}0.35\text{PbTiO}_3$. *J. Am. Ceram. Soc.* **84**, 2507–2513 (2001).
205. Kwon, O. H. & Messing, G. L. A theoretical analysis of solution-precipitation controlled densification during liquid phase sintering. *Acta Metall. Mater.* **39**, 2059–2068 (1991).
206. Kingery, W. D. Densification during sintering in the presence of a liquid phase. I. Theory. *J. Appl. Phys.* **30**, 301–306 (1959).
207. Kingery, W. D. & Narasimhan, M. D. Densification during sintering in the presence of a liquid phase. II. Experimental. *J. Appl. Phys.* **30**, 307–310 (1959).
208. Muramatsu, H. & Kimura, T. Effect of $\text{Pb}(\text{Zr}_x\text{Ti}_{1-x})\text{O}_3$ composition on crystallographic texture in PZT composites. *J. Eur. Ceram. Soc.* **25**, 2231–2234 (2005).
209. Ozer, I. O. *et al.* Anisotropic sintering shrinkage in alumina ceramics containing oriented platelets. *J. Am. Ceram. Soc.* **89**, 1972–1976 (2006).
210. Lange, F. F. & Metcalf, M. Processing-related fracture origins: II, Agglomerate motion and cracklike internal surfaces caused by differential sintering. *J. Am. Ceram. Soc.* **66**, 398–406 (1983).
211. Sudre, O., Bao, G., Fan, B., Lange, F. F. & Evans, A. G. Effect of inclusions on densification: II, Numerical model. *J. Am. Ceram. Soc.* **75**, 525–531 (1992).
212. Sudre, O. & Lange, F. F. The effect of inclusions on densification; III, The desintering phenomenon. *J. Am. Ceram. Soc.* **75**, 3241–3251 (1992).
213. Keskinbora, K., Suzuki, T. S., Ozer, I. O., Sakka, Y. & Suvaci, E. Hybrid processing and anisotropic sintering shrinkage in textured ZnO ceramics. *Sci. Technol. Adv. Mater.* **11**, 065006 (2010).
214. Chaisan, W., Yimnirun, R., Ananta, S. & Cann, D. P. Dielectric properties of solid solutions in the lead zirconate titanate-barium titanate system prepared by a modified mixed-oxide method. *Mater. Lett.* **59**, 3732–3737 (2005).
215. Li, G. & Haertling, G. Dielectric, ferroelectric and electric field-induced strain properties of $(\text{Pb}_{1-x}\text{Ba}_x)(\text{Zr}_{1-y}\text{Ti}_y)\text{O}_3$ ceramics. *Ferroelectrics* **166**, 31–45 (1995).
216. Ikeda, T. Studies on $(\text{Ba-Pb})(\text{Ti-Zr})\text{O}_3$ System. *J. Phys. Soc. Japan* **14**, 168–174 (1959).
217. Frantti, J. *et al.* Neutron diffraction studies of $\text{Pb}(\text{Zr}_x\text{Ti}_{1-x})\text{O}_3$ ceramics. *Jpn. J. Appl. Phys.* **39**, 5697–5703 (2000).
218. Amin, A., Newnham, R. E., Cross, L. E. & Cox, D. E. Phenomenological and structural study

- of a low-temperature phase transition in the PbZrO₃-PbTiO₃ system. *J. Solid State Chem.* **37**, 248–255 (1981).
219. Fernandes, J. C., Hall, D. A., Cockburn, M. R. & Greaves, G. N. Phase coexistence in PZT ceramic powders. *Nucl. Inst. Methods Phys. Res. B* **97**, 137–141 (1995).
220. Zhang, M. F., Wang, Y., Wang, K. F., Zhu, J. S. & Liu, J. M. Characterization of oxygen vacancies and their migration in Ba-doped Pb(Zr_{0.52}Ti_{0.48})O₃ ferroelectrics. *J. Appl. Phys.* **105**, 061639 (2009).
221. Zheng, H. Structure-property relations in Sr, Nb, Ba doped lead zirconate titanate. (University of Sheffield, 2001).
222. CeramTec UK Ltd. *Piezoceramic soft materials - Material data.* (2020).
223. Härdtl, K. H. Electrical and mechanical losses in ferroelectric ceramics. *Ceram. Int.* **8**, 121–127 (1982).
224. Navy SH. MIL-STD-1376B. *Piezoelectirc ceramic material and measurements guidelines for sonar transducers.* (1999).
225. Wang, Y., Shao, Q. Y. & Liu, J. M. Enhanced fatigue-endurance of ferroelectric Pb_{1-x}Sr_x(Zr_{0.52}Ti_{0.48})O₃ thin films prepared by sol-gel method. *Appl. Phys. Lett.* **88**, 122902 (2006).
226. Walton, R. L. *et al.* Tailoring particle alignment and grain orientation during tape casting and templated grain growth. *J. Am. Ceram. Soc.* **102**, 2405–2414 (2019).

A. Appendix

Example of a batch calculation for a singular starting reagent, M_mO_2 , to give weight, w , in grams of product $A_xM_yO_3$.

$$w_{(M_mO_2)} = \frac{w}{RMM_{(A_xM_yO_3)}} \times RMM_{(M_mO_2)} \times \frac{y}{m} \quad (29)$$

where RMM is the relative molecular mass, m and y are the specific elemental subscripts in the empirical formulas of the reagent and product, respectively.

Table 9 - 5 g batch calculation for molten salt synthesis of Aurivillius phase PBT precursor.

composition	PbO (g)	Bi ₂ O ₃ (g)	TiO ₂ (g)	KCl (g)
PBT	0.7568	3.1599	1.0832	-
molten flux	-	-	-	5.0000

Table 10 - 5 g batch calculation for topochemical conversion of PBT into NBT-PT

composition	PBT (g)	PbO (g)	NaCl (g)
NBT-PT	1.9893	1.3550	-
molten flux	-	-	1.6557

B. Appendix

Table 11 - 50g batch calculation for tapecasting PZT.

composition	PbO (g)	ZrO ₂ (g)	TiO ₂ (g)
PZT52	34.2740	9.8393	5.8867

Table 12 - 30 g matrix batch tapecast slurry formulation based on fixed dried tape volume.

component	solids (%)	density (g/cm ³)	slurry mass (g)	slurry volume (%)	dried tape mass (g)	dried tape volume (%)
matrix	100	8	30.0000	18.19	30.0000	54
WB4101	35	1.03	6.7441	31.76	2.3604	33
PL005	100	1	0.5556	2.69	0.5556	8
DS001	40	1	0.6944	3.37	0.2778	4
DF002	100	1	0.0694	0.34	0.0694	1
D.I. water	0	1	9.0000	43.65	-	0
Total	-	-	47.0635	100	33.2632	100

C. Appendix

Table 13 - 10 g batch calculations for PZTx-5BT compositions using starting PbO.

composition	PbO (g)	ZrO ₂ (g)	TiO ₂ (g)	BaTiO ₃ (g)
PZT52-5BT	6.8548	1.9679	1.1773	0.3961
PZT53-5BT	6.8457	2.0030	1.1513	0.3961
PZT54-5BT	6.8366	2.0381	1.1253	0.3961
PZT55-5BT	6.8275	2.0731	1.0994	0.3961
PZT56-5BT	6.8185	2.1080	1.0735	0.3961
PZT57-5BT	6.8095	2.1428	1.0477	0.3961
PZT58-5BT	6.8005	2.1775	1.0220	0.3961
PZT59-5BT	6.7915	2.2121	0.9964	0.3961
PZT60-5BT	6.7826	2.2467	0.9708	0.3961
PZT61-5BT	6.7736	2.2811	0.9453	0.3961

Table 14 - Calculated lattice parameters for PZTx-5BT compositions.

composition	final Zr/Ti ratio	structure	a (Å)	c (Å)	c/a ratio	cell volume (Å ³)
PZT52-5BT	0.972	tetragonal	4.0349	4.1429	1.0268	67.449
PZT53-5BT	1.008	tetragonal	4.0371	4.1417	1.0259	67.504
PZT54-5BT	1.049	tetragonal	4.0407	4.1414	1.0249	67.617
PZT55-5BT	1.088	tetragonal	4.0441	4.1391	1.0235	67.694
PZT56-5BT	1.132	tetragonal*	4.0472	4.1358	1.0219	67.744
PZT57-5BT	1.174	rhombohedral*	4.0773	=	1	67.783
PZT58-5BT	1.217	rhombohedral	4.0778	=	1	67.806
PZT59-5BT	1.268	rhombohedral	4.0804	=	1	67.937
PZT60-5BT	1.315	rhombohedral	4.0827	=	1	68.050
PZT61-5BT	1.370	rhombohedral	4.0844	=	1	68.136

*predominant phase within identified phase coexistence

